DOE/ER-0046/14

Nuc. Mat Inventory, JCS 12-8

Damage Analysis and Fundamental Studies

Quarterly Progress Report
April-June 1983

August 1983

U.S. Department of Energy
Office of Energy Research
Office of Fusion Energy
Washington, DC 20545

NOTICE

Printed in the United States of America
Available from
National Technical Information Service
U.S. Department of Commerce
5285 Port Royal Road
Springfield, VA 22161

NTIS price codes
Printed copy: A08
Microfiche copy: A01

DOE/ER-0046/14
UC-20,20c

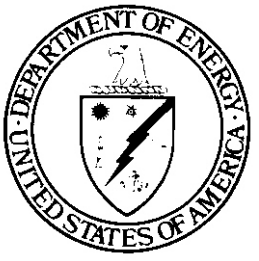

Damage Analysis and Fundamental Studies

Quarterly Progress Report
April-June 1983

August 1983

U.S. Department of Energy
Office of Energy Research
Office of Fusion Energy
Washington, DC 20545

FOREWORD

This report is the twenty-second in a series of Quarterly Technical Progress Reports on *Damage Analysis and Fundamental* ***Studies*** (DAFS), which is one element of the Fusion Reactor Materials Program, conducted in support of the Magnetic Fusion Energy Program of the U.S. Department of Energy (DOE). The first eight reports in this series were numbered DOE/ET-0065/1 through 8. Other elements of the Fusion Materials Program are:

- Alloy Development for Irradiation Performance (ADIP)
- Plasma-Materials Interaction (PMI)
- Special Purpose Materials (SPM).

The DAFS program element is a national effort composed of contributions from a number of National Laboratories and other government laboratories, universities, and industrial laboratories. It was organized by the Materials and Radiation Effects Branch, DOE/Office of Fusion Energy, and a Task Group on *Damage Analysis and Fundamental Studies,* which operates under the auspices of that branch. The purpose of this series of reports is to provide a working technical record of that effort for the use of the program participants, the fusion energy program in general, and the DOE.

This report is organized along topical lines in parallel to a Program Plan of the same title so that activities and accomplishments may be followed readily, relative to that Program Plan. Thus, the work of a given laboratory may appear throughout the report. Note that a new chapter has been added on Reduced Activation Materials to accommodate work on a topic not included in the early program plan. The Contents is annotated for the convenience of the reader.

This report has been compiled and edited under the guidance of the Chairman of the Task Group on *Damage Analysis and Fundamental Studies,* D. G. Doran, Hanford Engineering Development Laboratory (HEDL). His efforts, those of the supporting staff of HEOL, and the many persons who made technical contributions are gratefully acknowledged. T. C. Reuther, Materials and Radiation Effects Branch, is the DOE counterpart to the Task Group Chairman and has responsibility for the DAFS program within DOE.

G. M. Haas, Chief
Reactor Technologies Branch
Office of Fusion Energy

C H A P T E R 1

IRRADIATION TEST FACILITIES

CONTENTS

RTNS-II IRRADIATIONS AND OPERATIONS

C.M. Logan and **D. W.** Heikkinen
Lawrence Livermore National Laboratory

1.0 Objective

The objectives of this work are operation of **RTNS-II** (a 14-MeV neutron source facility), machine development, **and** support of the experimental program that utilizes this facility. Experimenter services include dosimetry, handling, scheduling, coordination, and reporting. RTNS-II is dedicated to materials research for the fusion power program. **Its** primary use is to aid in the development of models of high-energy neutron effects. Such models are needed in interpreting and projecting to the fusion environment, engineering data obtained in other spectra.

2.0 Summary

Irradiations were performed **for** 16 different experimenters during this quarter. Due to a malfunction in the target ***scan*** system, the HEDL furnace experiment was damaged after only 40 minutes of running and will be rescheduled later. **On** June 15, **1983** the right machine produced neutrons for the first time.

3.0 Program

Title: RTNS-II Operations (WZJ-16)
Principal Investigator: **C.** M. Logan
Affiliation: Lawrence Livermore National Laboratory

4.0 Relevant DAFs Program Plan Task/Subtask

TASK II.A.2,3,4.
TASK II.B.3,4
TASK II.C.1,2,6,11,18.

5.0 Irradiation - M. Logan, D. W. Heikkinen and M. W. Guinan

During this quarter, irradiations (both dedicated and add-on) were done for the following people.

Experimenter	P or A*	Sample Irradiated
J. Fowler (LANL)	P	MACOR - changes in electrical and mechanical properties.
N. Yoshida (Kyushu)	A	Pure metals and alloys - sub-cascade structure TEM, positron annihilation and tensile test.
C. Ichihara (Kyoto)	A	MgO - light absorption for dosimetry
Y. Ogawa (Nagoya)	A	Al alloys - activation analysis
R. Hopper (LLNL)	A	^{235}U and optical materials - etched fission fragment tracks in optical materials for surface treatment.
P. Hahn (Vienna)	A	Nb-Ti - measure fluxoid pinning strength of superconductors.
R. Hartmann (Northrop)	A	Integrated circuits - performance
C. Logan (LLNL)	A	1. Cu alloys - activation analysis 2. Cu-Al - Al assay 3. Loctite - strength
K. Okamura (Tohoku)	A	SiC - strength
C. Violet (LLNL)	A	1. W - Mossbauer effect 2. CuNi - magnetic, Mossbauer effect TEM and x-ray diffraction.
R. Borg (LLNL)	A	1. NiRh -magnetic properties 2. Geological samples - inert gas diffusion.
P. Cannon (HEDL)	P	FMIT instrumentation
D. Heikkinen (LLNL)	A	Nb - dosimetry calibration
T. Vercelli (LLNL)	A	Carbon fiber/epoxy - tensile strength

5.0 (Continued)

Experimenter	P or A*	Sample Irradiated
Y. Tabata (Tokyo)	A	Polymer materials - tensile strength
C. Snead (BNL)	A	Superconductors - critical field and current, transition temperature.

*P = Primary, A = Add-on

5.1 RTNS- tatus - C. M. Logan and D. W. Heikkinen

A mechanical failure in the sensing system used to measure target scan position caused the target controller to drive the target past the normal limit on the "up" direction. The spinning target hit the HEDL furnace. The furnace is being reconstructed. An overtravel switch has been installed on the target.

Operation of the right machine has begun. Neutrons were produced for the first time on June 15, 1983.

6.0 Future Work

Irradiations will be continued for P. Cannon (HEDL), R. Borg (LLNL), C. logan (LLNL), T. Vercelli (LLNL) and Y. Tabata (Tokyo). Also during this period, irradiations for M. Guinan (LLNL), T. Okada and C. Ichihara (Kyoto) will be made.

C H A P T E R 2

DOSIMETRY AND DAMAGE PARAMETERS

MEASUREMENT OF SPALLATION CROSS SECTIONS AT IPNS

L. R. Greenwood and R. K. Smither (Argonne National Laboratory)

1.0 Objective

To develop new cross sections and techniques for dosimetry and damage analysis at accelerator-based neutron sources.

2.0 Summary

Spallation cross sections for Al and Cu have been measured at the IPNS at Argonne National Laboratory. Results are reported for the Al reactions to ^{7}Be, ^{22}Na, and ^{24}Na at proton energies between 80-450 MeV. These reactions will be used to extend our dosimetry technique to higher energies and will improve damage and transmutation rates for accelerator-based neutron sources such as IPNS and FMIT.

3.0 Program

Title: Dosimetry and Damage Analysis

Principal Investigator: L. R. Greenwood

Affiliation: Argonne National Laboratory

4.0 Relevant DAFS Program Plan Task/Subtasks

Task ZI.A.2 High-Energy Neutron Dosimetry

5.0 Accomplishments and Status

At present, dosimetry cross sections are not well known above 14 MeV and only a few reactions have been measured up to 28 MeV. Accelerator-based neutron sources extend to much higher neutron energies. For example, FMIT will produce neutrons up to 55 MeV and spallation sources up to 500-800 MeV. Even though these sources do not have a large fraction of their neutrons above 30 MeV, it is necessary that some data be developed to monitor these high-energy and very damaging events. Spallation cross sections appear to have the greatest potential for dosimetry above about 40 MeV since one target material will produce virtually all lower-z activation products, each product having a different production threshold and energy dependence. Routti and Sandberg[1] have shown that copper spallation products can be used to unfold neutron spectra at CERN. Unfortuantely, the required spallation cross sections are not very well known for this purpose. Consequently, we have initiated spallation measurements at the Intense Pulsed Neutron Source (IPNS) at Argonne National Laboratory.

The IPNS consists of a 50 MeV proton linac which feeds a synchroton capable of accelerating protons up to 500 MeV. In a somewhat unusual use of this facility, we have placed various materials directly into the proton beam and changed the extraction time to obtain proton energies as low as 80 MeV. In this way we were able to obtain activation measurements at proton energies of 80, 100, 150, 200, 400, and 450 MeV. It should be noted that proton and neutron cross sections are expected to be identical at high particle energies. Al, Cu, V, Nb, and Zr foils measuring 4" x 4" x 5 mils were irradiated in stacks of three foils per material. The center foils were gamma counted while the front and

back foils are used to correct for recoil losses. At present, only the Al results have been completely analyzed and these data are reported here. The other materials produce many more activation products and some foils are still being counted in order to measure the longer-lived activities.

Three activities were measured from the Al foils, namely ^{7}Be, ^{22}Na, and ^{24}Na. Each energy point required an irradiation of about 0.5-1 hour with a proton fluence of about 10^{17}. The proton current was measured using a beam dump designed to operate as a Faraday cup. An extraction toroid was also used to monitor the proton beam, although this toroid was only calibrated at energies above 400 MeV. Following irradiation, the foils were allowed to cool in the beam tunnel for a few hours and then transported to the gamma counting facilities in the Chemical Technology Division at ANL. Prior to counting, each foil was autoradiographed using polaroid film. This served two purposes. First, the autoradiographs confirmed that the proton beam was roughly centered on the foils and had a beam diameter of about 1". Secondly, this allowed us to cut the foils into a hot center portion and a relatively cold outer portion prior to gamma counting. This reduced the size of the foil stack to minimize geometric and absorption corrections.

The measured cross sections are listed in Table 1 and plotted in Figs. 1-3. The values are compared to a semi-empirical model of spallation proposed by Rudstam.[2] It should be noted that the Rudstam cross sections shown on the figures include contributions from other short-lived isotopes in the same A-chain. Hence, ^{22}Na includes ^{22}Mg, ^{24}Na included ^{24}Ne, and ^{7}Be includes ^{7}B (weak). As can be seen, the Rudstam formulas are reasonably close to the

TABLE 1

Al SPALLATION CROSS SECTIONS MEASURED AT IPNS
(Estimated accuracy ±5%)

	Cross Section, mb		
Energy, MeV	7Be	^{22}Na	^{24}Na
80	0.76	20.75	11.42
100	0.89	18.28	10.53
150	1.15	15.75	9.64
200	1.43	15.08	9.50
400	2.85	13.50	--
450	3.05	13.28	9.68

experimental measurements only for ^{22}Na. This is not totally unexpected since ^{24}Na can also be made by the ^{27}Al(n,α) reaction and the theory is known to work poorly for isotopes either too close to the target isotope or too light in mass. The data is also compared to an earlier evaluation3 and it also appears that our 7Be measurements differ considerably. However, previous data appears to have an appreciable scatter, possibly due to poor integration of the proton beam or inadequate recoil corrections.

6.0 References

1. J. T. Routti and J. V. Sandberg, Comp. Phys. Commun. 21, pp. 119-144, 1980.
2. G. Rudstan, Z. Naturforsch. 21a, p. 1027, 1966.
3. J. Tobailem, C. H. Lassus - St. Genies and L. Leveque, CEA Report N1466, 1971.

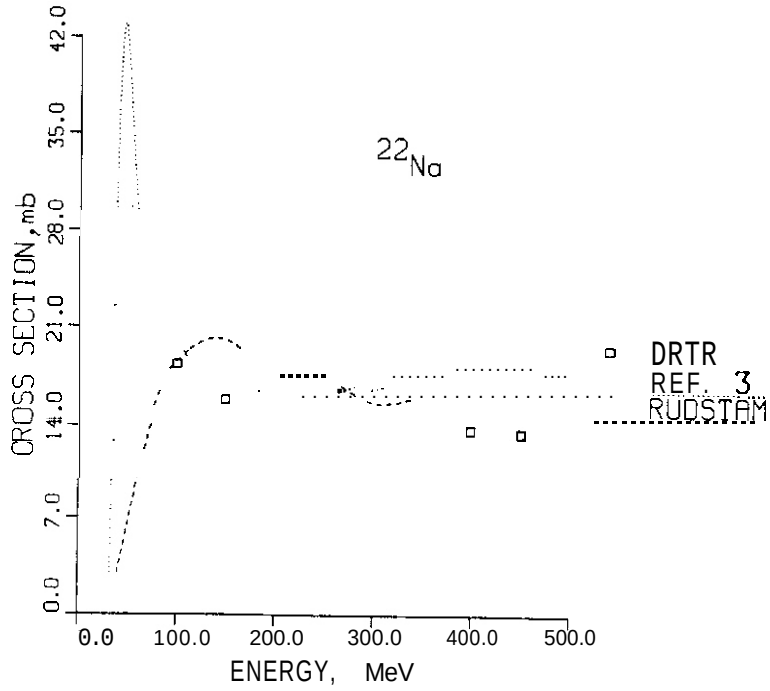

FIGURE 1. **Spallation Cross Sections for the ^{27}Al(n,*)22Na Reaction Compared with Previous Data and Theory.**

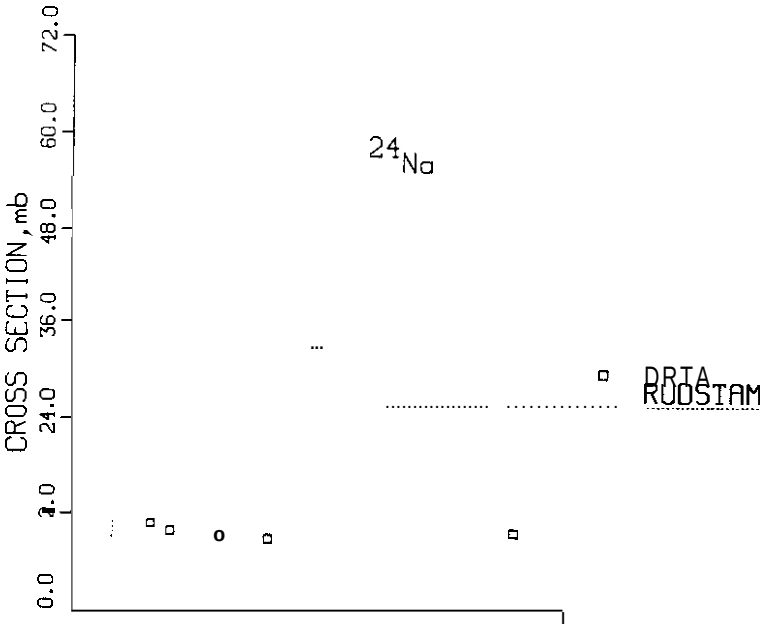

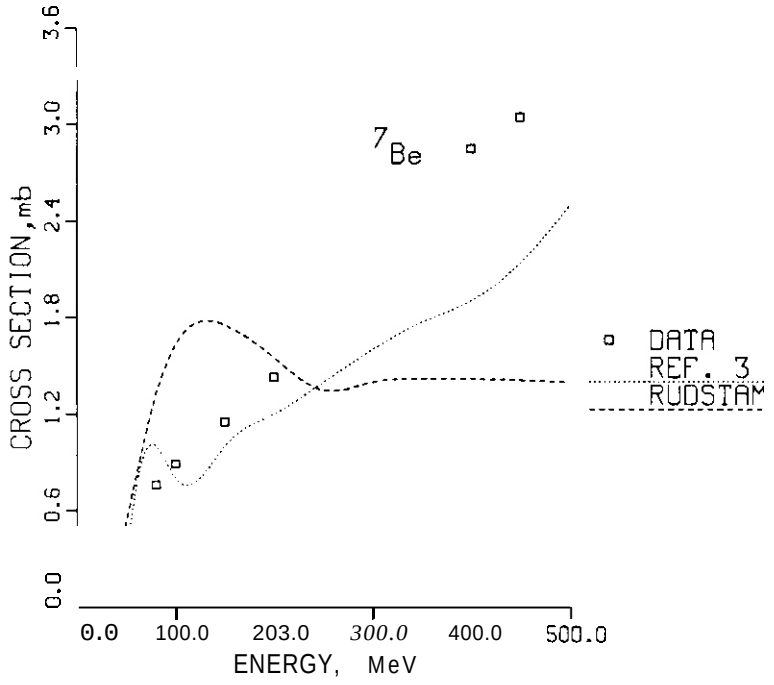

FIGURE **3.** Spallation Cross Sections for the $^{27}Al(n,*)^{7}Be$ Reaction Compared with Previous Data and Theory.

7.0 Future Work

Cross sections will be measured at additional energies to complete the excitation functions. The Cu, Nb, V, and Zr data will be analyzed shortly. Integral neutron data taken at IPNS will then be compared with calculated neutron spectra to assess the technique for high-energy spectral unfolding.

8.0 Publications

None.

MEASUREMENT OF THE HALF-LIFE OF ^{60}Fe USING ACCELERATOR MASS SPECTROMETRY

R. K. Smither, L. R. Greenwood, W. Kutchera, P. J. Billquist, D. Henning, X. A. Ma,* L. F. Mausner,** M. Paul,*** R. Pardo, K. E. Rehm, and J. L. Yntema
(Argonne National Laboratory)

1.0 Objective

To develop new cross sections and techniques for dosimetry and damage calculations.

2.0 Summary

A new technique, AMS[1] (Accelerator Mass Spectrometry), was used to measure the half-life of ^{60}Fe. The AMS technique measured the concentration of ^{60}Fe in a sample produced through spallation in Cu by a 200-MeV proton beam. This concentration measurement was combined with the measurement of the radioactive decay rate of the ^{60}Fe sample measured in a low-level gamma counting facility to determine the half-life of ^{60}Fe. The main objective of the experiment was to develop the combination of the Argonne FN Tandem plus the Argonne Super-Conducting Linac as an accelerator mass spectrometry system capable of measuring isotope ratios of 10^{-8} to 10^{-12} for masses as heavy as 60 atomic mass units. This technique can then be used to measure other long-lived or stable transmutation products for fusion dosimetry and for the assessment of fusion waste products.

* Institute of Atomic Energy, Peking, Peoples Republic of China
** Brookhaven National Laboratory, Long Island, New York.
*** The Hebrew University of Jerusalem, Jerusalem, Israel.

3.0 Program

Title: Dosimetry and Damage Analysis

Principal Investigator: L. R. Greenwood

Affiliation: Argonne National Laboratory

4.0 Relevant DAFS Program Plan Task/Subtask

Task II.A.5 Technique Development for Dosimetry Applications

Task II.B.1.2 Acquisition of Nuclear Data for the Calculation of Defect Production Cross Sections

5.0 Accomplishments and Status

5.1 Introduction

The original accelerator mass spectrometer (AMS) system developed at Argonne[1] used only the FN Tandem and was capable of measuring isotope ratios and concentrations for elements as heavy as aluminum[2] and silicon[3] with ease. As the method was extended to heavier masses (Cl, Ca, and Ti)[1,4] the technique became more difficult and more time consuming and experiments with elements as heavy as Fe were not possible because of the lack of sufficient energy in the accelerated beams. To get around the insufficient energy problem a new AMS systems was developed that combined the Argonne FN Tandem with the Argonne Super-Conducting Linac. The increased accelerating power of this new system makes it possible to perform experiments in the mass-60 range with some potential for

the mass 70 to 80 range. The measurement of the half-life of ^{60}Fe was performed to demonstrate the potential of this new AMS system. The only published value[5] for the half-life of ^{60}Fe gave a value of $T_{1/2} = 3 \times 10^5$ yrs with an uncertainty of a factor of 3. The ^{60}Fe was prepared through the spallation reaction in this previous work and the value used for the concentration of ^{60}Fe in the sample was estimated from spallation cross-section systematics. The uncertainty in this estimate was the main contribution to the large uncertainty in the quoted half-life value. By actually measuring the concentration of ^{60}Fe in the sample with the AMS method this uncertainty is eliminated and a check on the spallation theory can be obtained. This type of check on the spallation theory should lead to further improvements in the theory and better damage calculation where the source of the damage is very energetic neutrons or protons. The AMS technique will be applied to measure the production of long-lived activities in fusion waste products as well as for dosimetry purposes. Stable transmutants can also be measured to test the effects of transmutation on materials properties.

5.2 The Accelerator Mass Spectrometry Measurement of the Half-Life of ^{60}Fe

The sample of ^{60}Fe material was produced by spallation in a Cu target with 200 MeV protons in the Brookhaven Linac Isotope Produces (BLIP). The Fe fraction was chemically extracted in September 1982 after a wait of one year. The sample contained approximate 10^{15} atoms of ^{60}Fe along with mCi quantities of ^{55}Fe ($T_{1/2}$ = 2.7 years) and μCi quantities of ^{59}Fe ($T_{1/2}$ = 45.1 days). After an additional waiting period of 5 months the chemically separated Fe sample was added to a known amount of natural Fe and the AMS method was used to measure

the $^{60}Fe/Fe$ ratio. Several 130 mg pellets were made from this sample for use in an improved inverted sputter source as the source of the particle beams measured in the AMS system. The ^{60}Fe ions were accelerated to 320 MeV in the Tandem-Linac system, analyzed by an Enge split-pole magnetic spectrometer and counted in the multiple chamber position sensitive detector located in the focal plane of the spectrometer. The resulting three dimensional yield plot of counts (vertical) versus total energy (E) versus energy loss in the first section of the detector (ΔE) is shown in Fig. 1. The plot for the active Fe sample is shown in the upper half of the figure exhibits a cleanly separated ^{60}Fe peak while the plot for the Cu blank shown in the lower part of the figure (note the scale change of 100) demonstrates how well the ^{60}Fe peak is separated from the strong background peak of ^{60}Ni. The particle beam passed through an Al foil stack before being magnetically analyzed in the spectrometer. The difference in energy loss due to the different Z's (atomic charge) of ^{60}Fe and ^{60}Ni particles as they passed through this Al foil stack made it possible to separate the ^{60}Fe beam from a strong background beam of stable ^{60}Ni atoms. The different energy loss (ΔE) in the first section of the detector also helps to separate the ^{60}Fe beam from the background in the three dimensional plot in Fig. 1. The single count in the peak labled ^{60}Fe in the lower graph is believed to be cross contamination in the ion source. The results of 18 individual runs were averaged to give a ratio of $^{60}Fe/Fe$ of 1.16×10^{-7} with an uncertainty of 20%. Most of this uncertainty is related to the variation in the operation and thus the efficiency or transmission from run to run of this complex acceleration system.

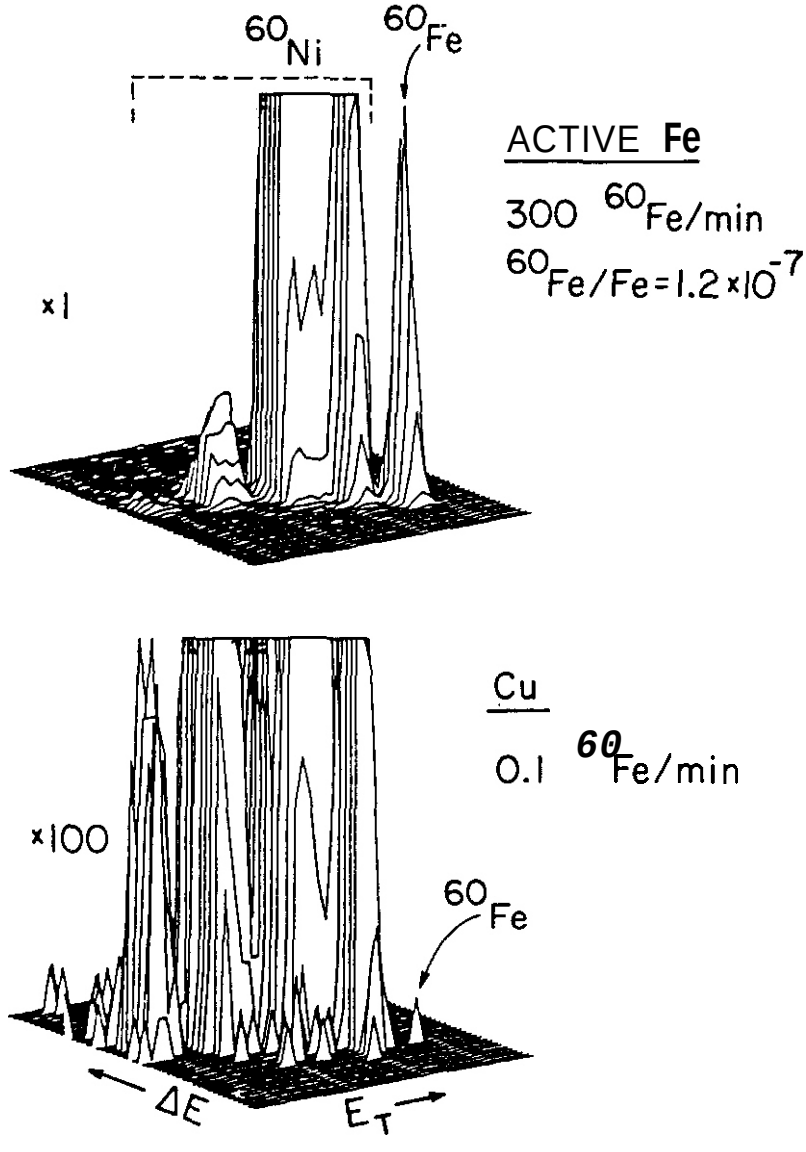

FIGURE 1. Three-Dimensional Plot of Counts (Vertical) Versus Total Energy of the Ion (E_T) and Partial Energy Loss in the First Section of the Focal Plane Detector. The upper plot is for the sample containing ^{60}Fe, and the lower plot is for a Cu blank in the ion source.

With the concentration of ^{60}Fe in the sample known from the AMS experiments one need only to measure the rate of decay of the sample to be able to calculate a half-life. This is difficult to do directly because 100% of the ^{60}Fe atoms decay to the 2+ (56.60 keV) state of ^{60}Co which decays 99.75% of the time to the 5+ groundstate of ^{60}Co through a highly converted low energy transition (56.60 keV) which makes it very difficult to be oberved (see Fig. 2). What can be observed is the subsequent decay of the ^{60}Co to ^{60}Ni. Figure 2 shows this somewhat complicated decay pattern. By monitoring the buildup of ^{60}Co as a function of time by measuring the change in intensity of the *two* ^{60}Co decay gamma rays at 1173.2 keV and 1332.5 keV one can calculate the primary decay rate of the ^{60}Fe sample. This low level counting is now in progress at the low-level gamma counting facility at Argonne-CMT. The original sample was found to have a considerable amount of residual ^{60}Co in it so a second chemical separation was performed in early March of 1983. The buildup of ^{60}Co in this sample has been monitored for three months. This data sets a lower limit on the half-life of ^{60}Fe of 1.3×10^6 yrs. This limit is about four times longer than the previous measurement of 3×10^5 yrs.[5] The upper limit has not been established yet because uncertainties of the data points make them consistent with an infinite half-life. The low level counting experiments are still in progress and will be continued until an upper limit on the half-life is also determined.

Although ^{60}Fe is not produced by fusion neutrons the experiment described above demonstrate the capability of the AMS technique to measure the transmutation rates and/or production rates of long-lived isotopes in the mass-60 region.

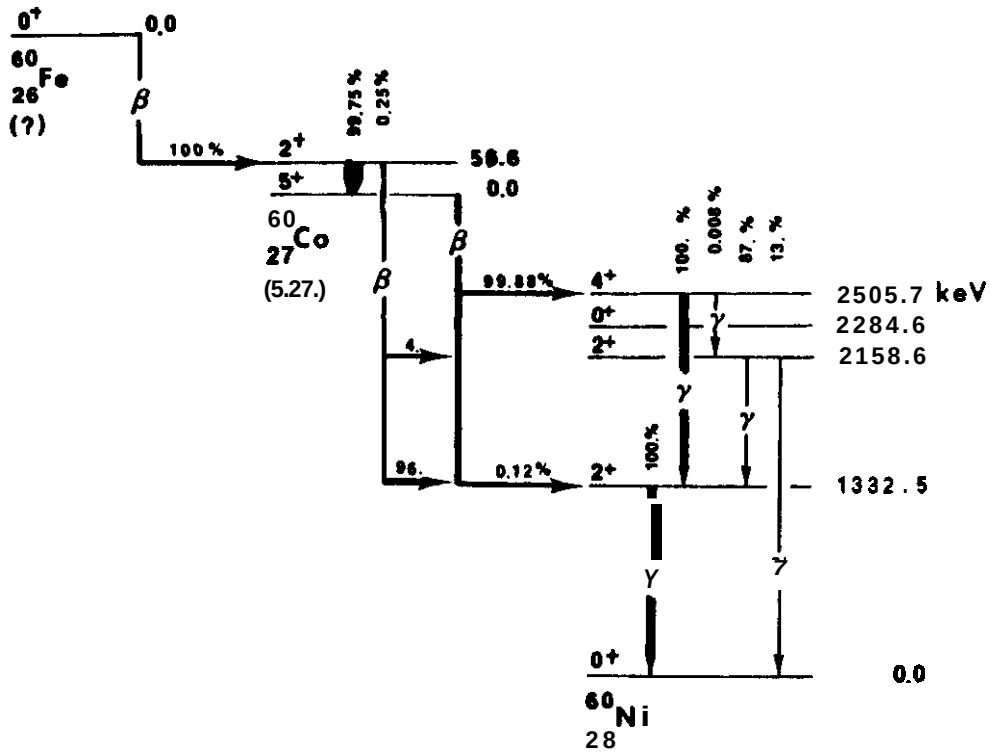

FIGURE 2. Radioactive Decay Scheme of ^{60}Fe and the Subsequent Decay to ^{60}Co to ^{60}Ni. The branching ratios for each mode of decay are given in %. The level energies in each isotope are given to the left. The half-life of the ground state of each isotope is given in parentheses below the level.

6.0 References

1. W. Henning, W. Kutschera, M. Paul, R. K. Smither, E. J. Stephenson and J. L. Yutema, Nucl. Inst. & Meth. 184, p. 247, 1981.

2. R. K Smither and L. R. Greenwood, "Measurement of the $^{27}Al(n, 2n)^{26}Al$ Cross Section," Damage Analysis and Fundamental Studies Quarterly Progress Report, DOE/ER-0046/7, pp. 39-49, November 1981.

3. W. Kutschera, W. Henning, M. Paul, R. K. Smither, E. J. Stephenson, J. L. Yutema, D. E. Alberger, J. Cumming and G. Harbottle, Phys. Rev. Lett. 45, pp. 592-596, August 1980.

4. D. Frekas, W. Henning, W. Kutschera, K. E. Rehm, R. K. Smither, J. L. Yutema and B. Stievano, Bull. Am. Phys. Soc. 27, p. 712, September 1982.

5. J. C. Roy and T. P. Kohman, Can. J. Phys. 35, p. 649, 1957.

7.0 Future Work

The AMS technique has several quite interesting applications to fusion neutron dosimetry. Long-lived activities can be measured for assessment of waste and for dosimetry during long irradiations. We have observed ^{26}Al (730,000 yr) and can detect ^{10}Be, ^{14}C, ^{53}Mn, ^{59}Ni, ^{93}Mo, ^{93}Zr, and ^{94}Nb, all of which are produced in fusion materials. Stable transmutants can also be detected to determine transmutation rates which are of concern since compositional changes eventually change the properties of materials and alloys.

8.0 Publications

"Accelerator Mass Spectrometry of ^{59}Ni and Fe Isotopes at the Argonne Super-Conducting Linac" W. Henning, W. Kutchera, B. Myslek-Laurikainen, R. C. Pardo, R. K. Smither, and J. L. Yntema. Proceedings of the Symposium on Accelerator Mass Spectrometry, Argonne National Laboratory, Argonne, Illinois, 11-13 May 1981. Proceedings of the Symposium organized by W. Henning, W. Kutschera, R. K. Smither, and J. L. Yntema.

Physics Division Report ANL-PHY-81-1 (May 1981)

"Measurement of the Half-Life of ^{60}Fe Using the Argonne FN Tandem-Super-conducting Linac System as an Accelerator Mass Spectrometer. W. Kutschera, P. J. Billquist, D. Frekers, W. Henuing, X. Z. Ma, L. F. Mausner, M. Paul, R. Pardo, K. E. Rehm, R. K. Smither, and J. L. Yntema. Proceedings of the Conference on Nuclear Physics with Heavy Ions (Prospects at Energies below 20 MeV/amn, April 14-16, 1983, State University of New York/Stony Brook, Stony Brook, New York.

COMPUTER SIMULATION OF DISPLACEMENT CASCADES IN COPPER

H. L. Heinisch (Westinghouse Hanford Company)

1.0 Objective

The objective of this work is to develop computer models for the simulation of high-energy cascades which will be used to generate defect production functions for correlation analysis of radiation effects.

2.0 Summary

A compendium of information on computer-simulated displacement cascades in copper is now available, and it is summarized here. The compendium contains graphical depictions of 21 cascades ranging in energy from 1-200 keV, along with quantitative analyses of cascade shapes and sizes and defect densities within cascades. The pictures clearly show that with increasing PKA energy, cascade configurations undergo a transition from production of a single compact damage region to widely spaced multiple damage regions. The number of distinct damage regions ("lobes") per cascade is found to increase uniformly with PKA damage energy beginning at about 30-50 keV. The high-energy cascades, although highly irregular in shape, have been classified into two main categories of shapes: "starbursts" and "chains". The defect density of the cascades decreases with

increasing energy, but the average localized defect density remains constant.

3.0 Program

Title: Irradiation Effects Analysis (AKJ)

Principal investigator: D. G. Doran

Affiliation: Westinghouse Hanford Company

4.0 Relevant DAFS Program Plan Task/Subtask

Subtask II.B.2.3 Cascade Production Methodology

5.0 Accomplishments and Status

A knowledge of the initial damage state produced in metals by the various neutron spectra of fusion materials test facilities is an essential element for the development of correlation models. For example, the study of various "cascade effects," i.e., the effects arising from point defects being created collectively in discrete cascades as opposed to being created homogeneously, is aided considerably by a knowledge of the spatial distributions of defects within cascades. Computer simulations of the production of displacement damage initiated by primary knock-on atoms (PKAs) provide detailed information on an atomic scale not readily attainable by experimental methods.

A compendium of information on computer-simulated displacement cascades in copper is now available as a HEDL report.[1] it

contains computer graphics of 21 representative cascades along with quantitative analysis of cascade shapes and sizes and defect densities. A summary of the information in that report is presented here, including the results of the defect density analyses, which have not been reported elsewhere.

Using the MARLOWE code[2] (version 11), results were obtained for PKAs with energies from i keV to 500 kev. This covers cascade behavior ranging from the production of only a few isolated defect pairs per cascade at low energies to the production of widely separated, but densely populated, multiple damage regions at high energies. The average PKA energy resulting from i4-MeV neutrons in copper is about 170 keV, so the energy range treated here is well into the realm of importance for fusion materials irradiations.

The information in this report deals exclusively with the collisional phase ($\sim 10^{-13}$ sec) of cascades produced individually in an otherwise perfect crystal of a pure material. The information obtained by simulations of the subsequent quenching and short-term annealing phases[3] indicates that the initial structure of the cascade is the dominating factor in its subsequent disposition.

Table 1 contains the values of MARLOWE code parameters employed in this study. These parameter values were determined by

Robinson[4] in a comparison of MARLOWE with results of more rigorous molecular dynamics simulations of lower energy cascades.[5]

TABLE 1

MARLOWE PARAMETER SETTINGS FOR CASCADES GENERATED IN COPPER AT 300K

Interatomic Potential:	Moliere. with screening length of 7.30 pm
Inelastic Losses:	Local (Firsov)
Lattice Parameter:	ALAT = 0.3615 nm
Maximum Impact Parameter:	RB = 0.62 lattice parameters
Debye Temperature:	TDEBYE = 314 K
Energy Criteria for Displaced Atoms:	EDISP = 5.0 eV EQUIT = 4.8 eV EBND = 0.2 eV

Three-dimensional drawings of the vacancy and interstitial configurations of typical cascade structures for 1- to 200-keV cascades in copper were produced using computer graphics. Figures 1-3 show typical 2-, 20- and 200-keV cascades, respectively.

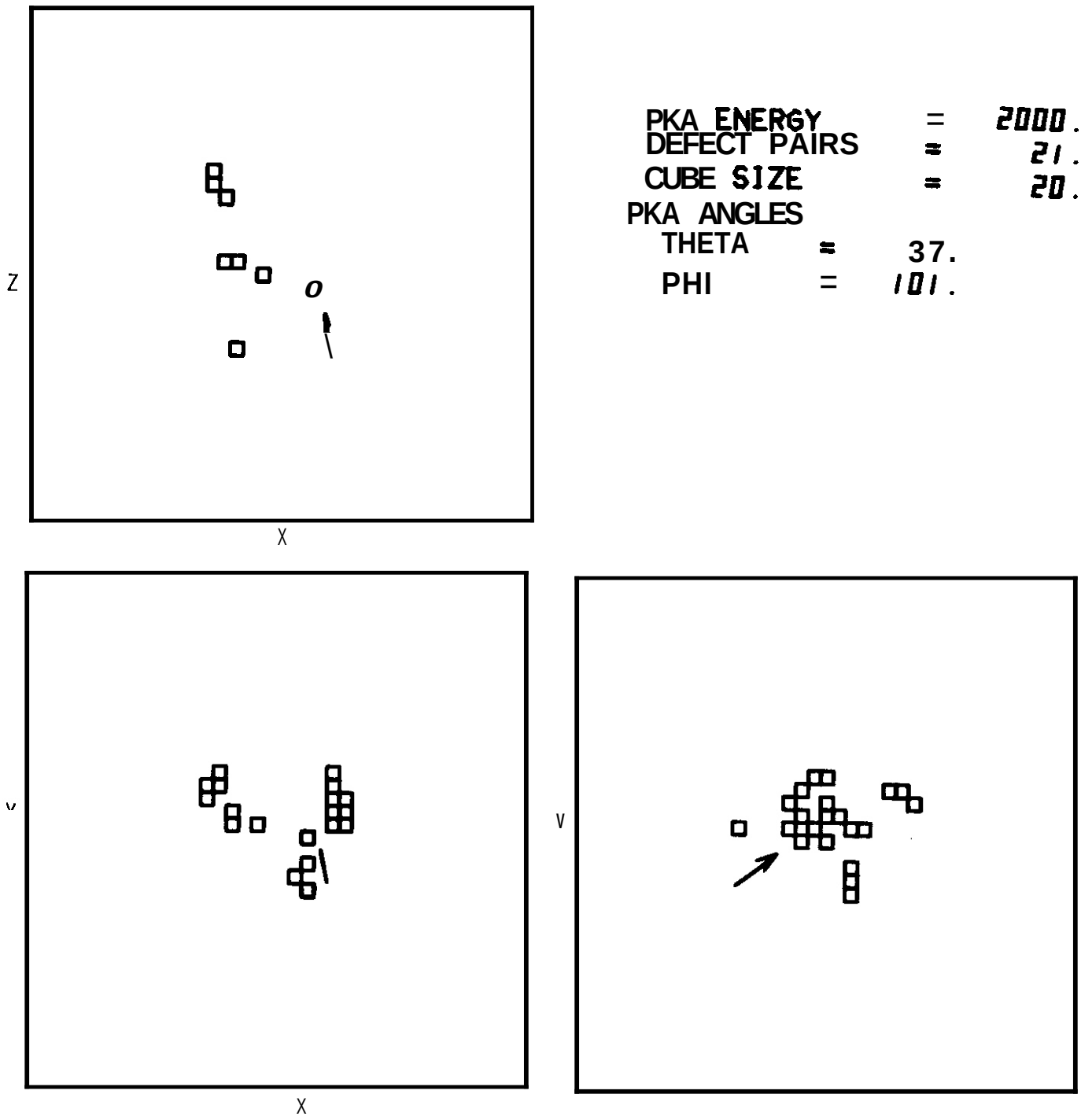

FIGURE 1. (a) Orthographic Projection of the Vacancy Distribution of a Typical 2-keV Cascade. In Figures 1-3 the small arrows show the original position and direction of the PKA.

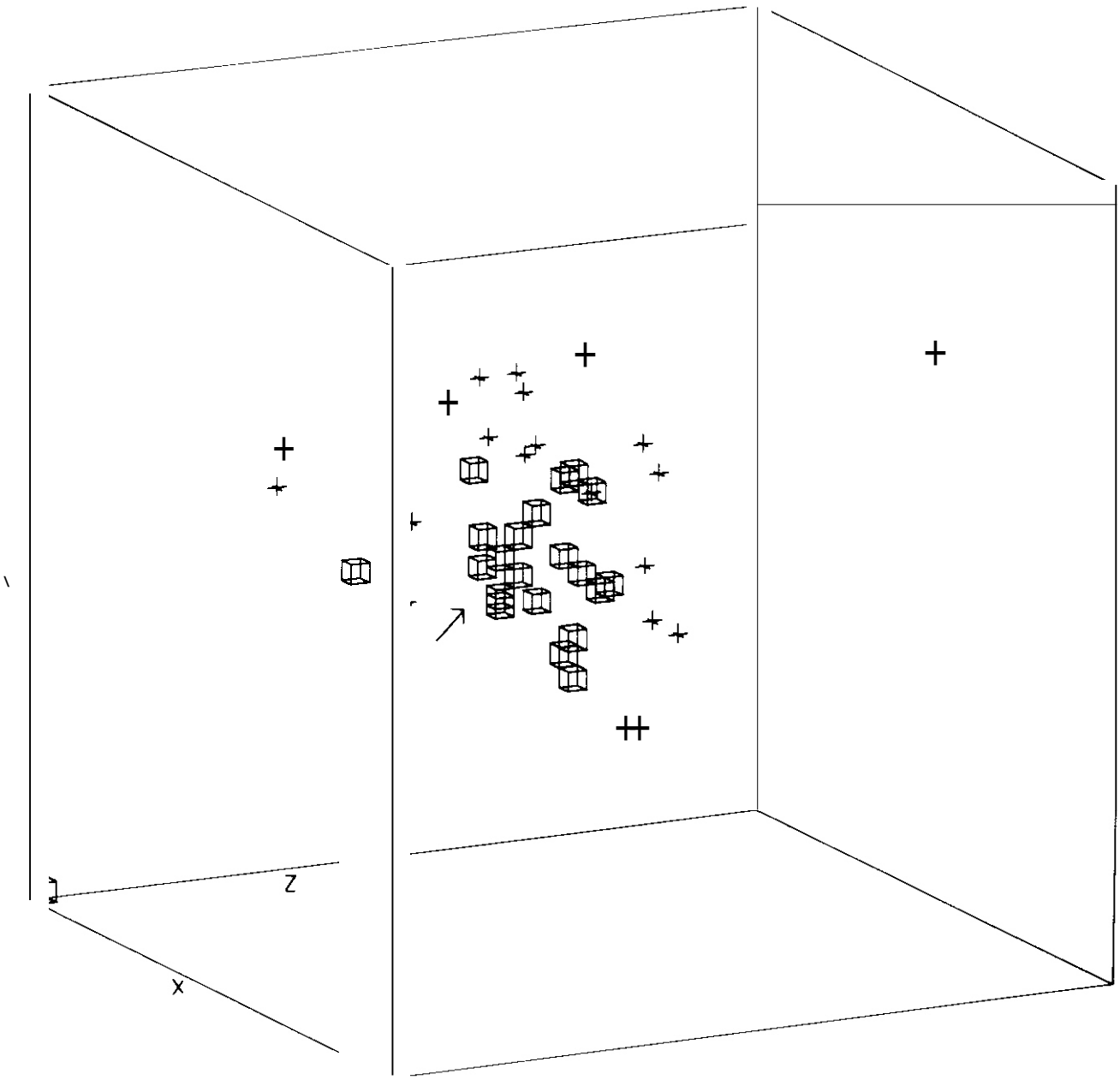

FIGURE 1. (b) 3-D View of a Typical 2-keV Cascade. The vacancies are represented by cubes and the interstitials by "stars". Each three-dimensional symbol is 1/2 lattice parameter on a side.

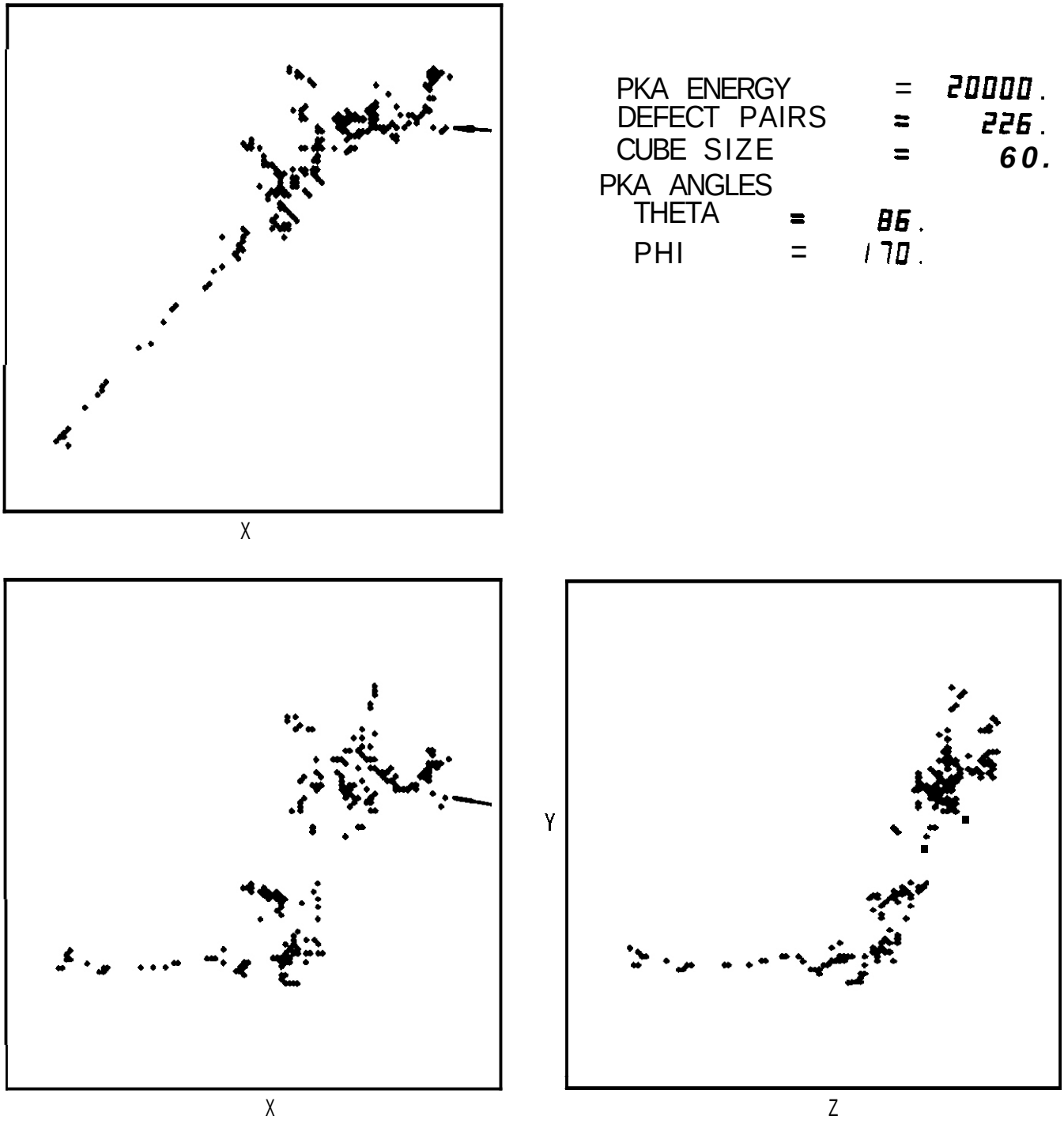

FIGURE 2. (a) Orthographic Projection of the Vacancy Distribution of a Typical 20-keV Cascade.

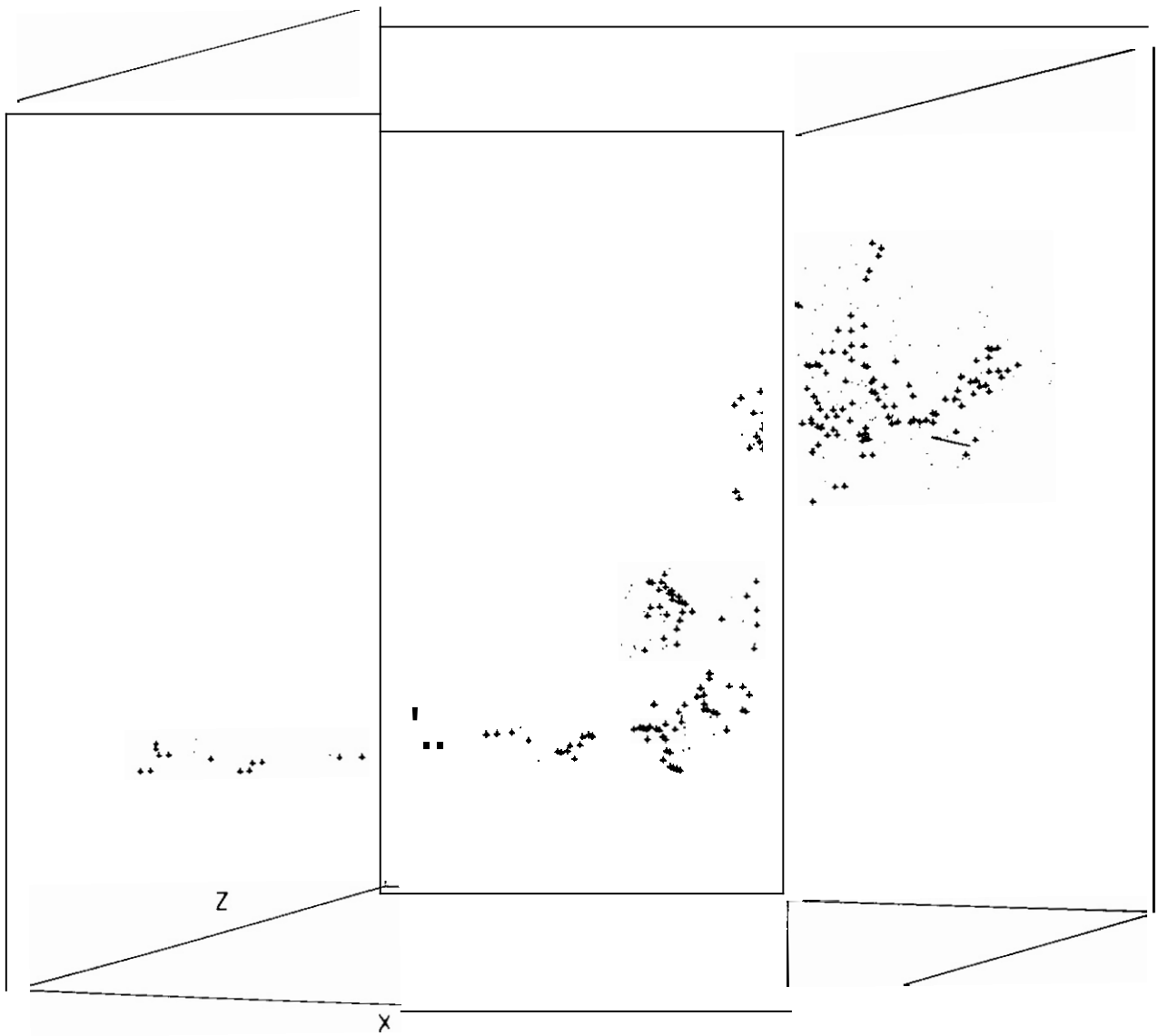

FIGURE 2. (b) 3-D view of a Typical 20-keV Cascade. At 20-keV and above, the vacancies are represented by 1/2 lattice parameter stars, and the interstitials are simply dots. As the actual size of the plotted stars decreases, they tend to appear as diamond shapes, then as large dots.

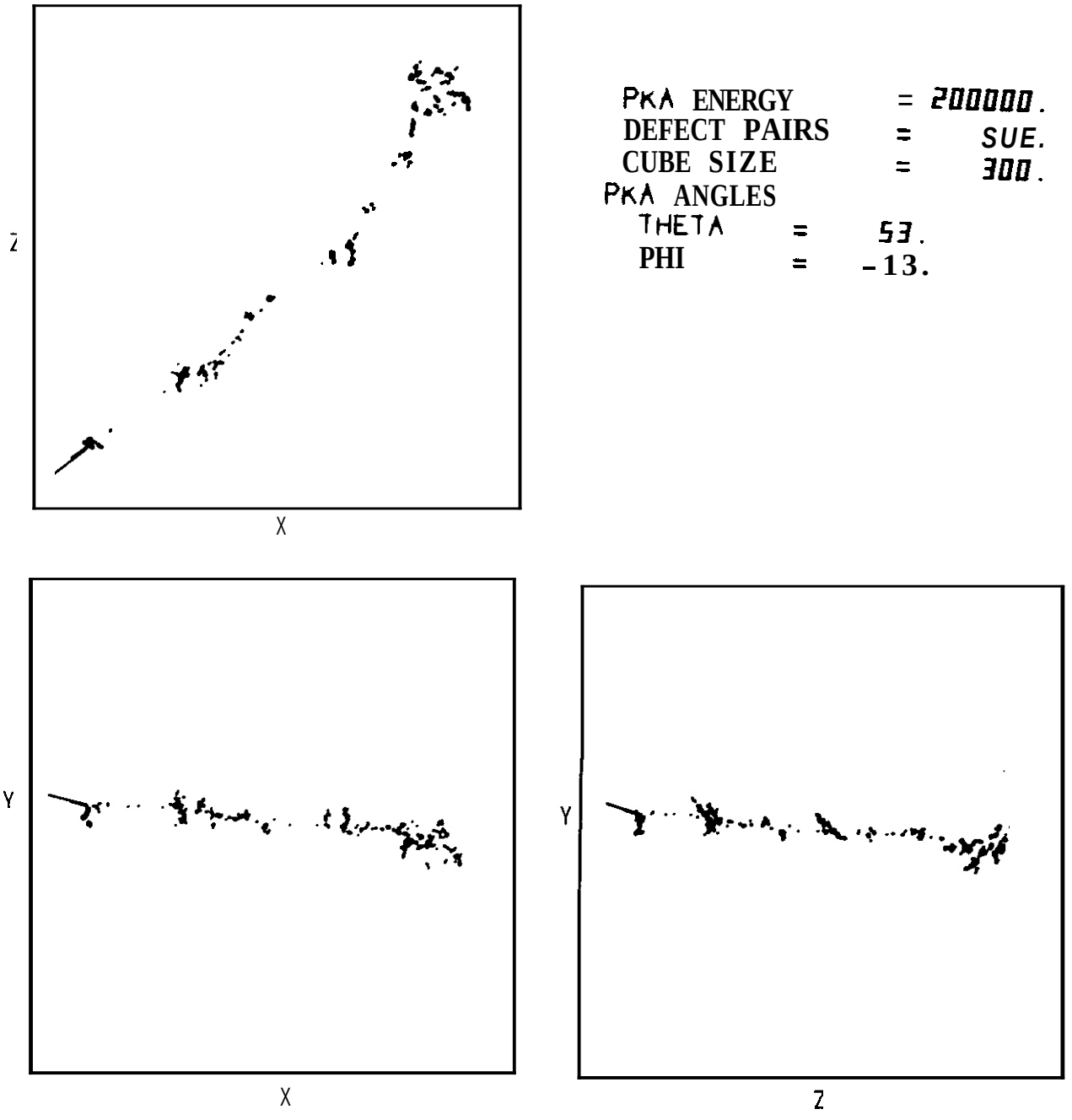

FIGURE 3. (a) Othographic Projection of the Vacancy Distribution of a Typical 200-keV Cascade.

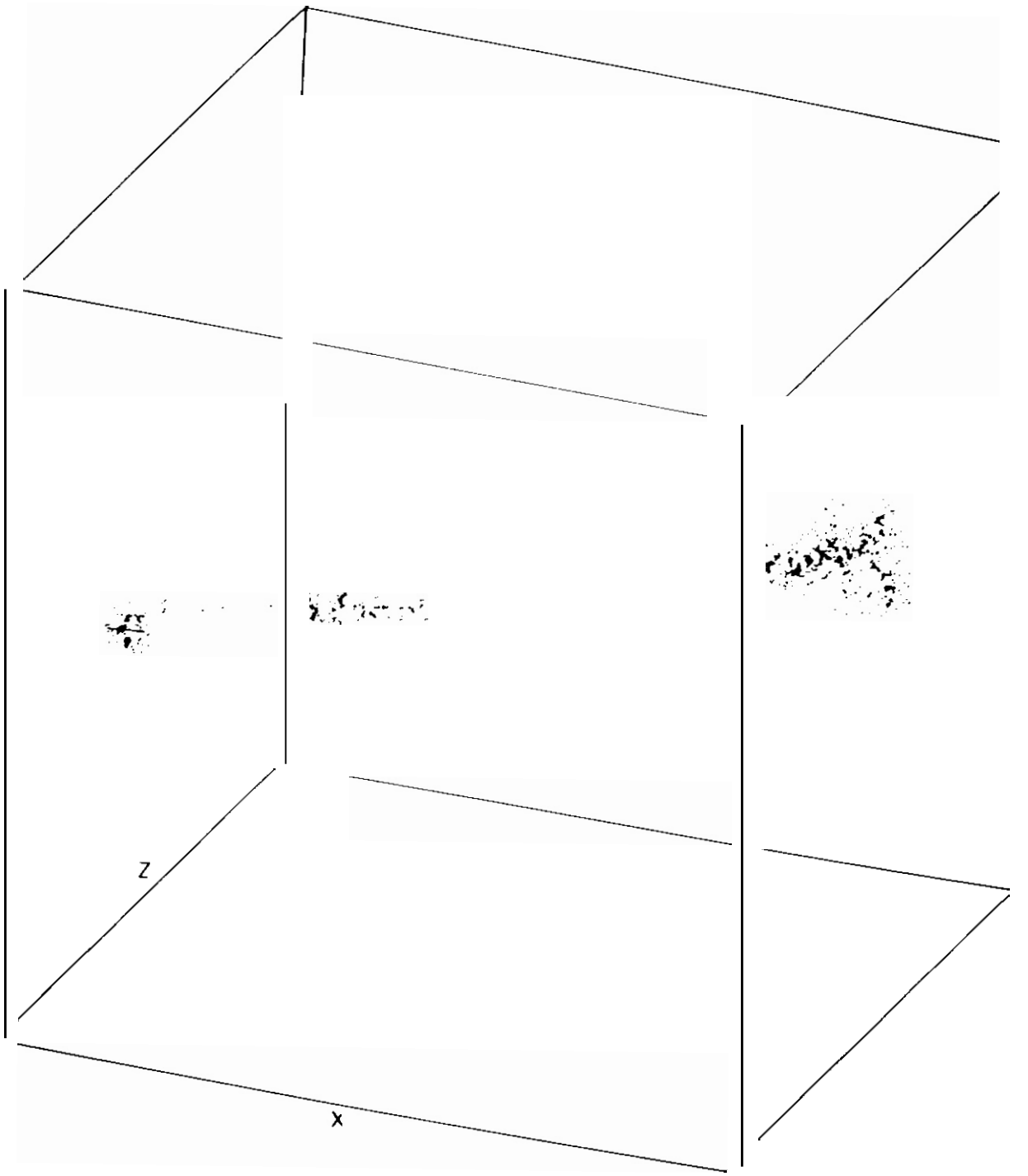

FIGURE 3. (b) 3-D View of a Typical 200-keV Cascade.

Each cascade is depicted in four views: three orthographic projections of the vacancy distribution along the directions of the cubic crystal axes (part a), and one three-dimensional view of both vacancies and interstitials enclosed in a cube aligned with the cubic crystal axes (part b). The legend for each cascade gives the PKA energy in eV, the number of defect pairs in the picture, the size of the cube edge in lattice parameters, and the angle in degrees of the initial momentum vector of the PKA with respect to the crystal axes.

At low energies, the general configuration is a single depleted zone surrounded by a more diffuse cloud of interstitials.

There does not appear to be a sharp threshold at which widely-spaced multiple damage regions are always produced. Cascades from 20-50 keV occur with both widely spaced damage regions and with what appears to be only one major damage region. Perhaps the apparently single-damage regions should be considered as closely-spaced, multiple-damage regions. This viewpoint led to the description of cascades in terms of "lobes" for the purpose of quantitative analysis.

At 100-keV and above, the cascades exhibit two typical configurations, a "starburst" configuration of several damage regions emanating from a central point, and the "chain" configuration of damage regions strung out along a single path

(Figure 3). Most higher energy cascades can be classified as either chains or starbursts, or as some combination of the two forms.

In general, the high energy cascades appear to be made up of collections of lower energy cascades, sometimes contiguous, sometimes wldeiy separated. Because of thelr irregular shapes, it is difficult to describe the true lengths or volumes of the high energy cascades In quantitative terms. However, attempts have been made to obtain quantitative characterization of the cascades, and this information is contained in Ref. 6 and 7.

Another quantity of Interest is the defect denslty of cascades. The difficulty in determining meaningful defect densities lies in defining the volume of the cascade. How the volume, hence the defect density, is defined depends very much on the application of the information. In some cases the cascade volume or size itself may be more pertinent than the defect density, e.g., In studying cascade overlap or the interactions of cascades wlth precipitates. However, other properties may be influenced by the detailed behavior of the individual defects after they are created. The subsequent behavlor of defects is strongly Influenced by their immedlate surroundings. Hence, one must have a clear idea of what the defect density value represents.

Let the volume of the cascade be the volume of the parallelepiped $\Delta x \Delta y \Delta z$, oriented along the crystal axes x, y, z, that just encloses the vacancy distribution of the cascade, and divide that into the number of defects that remain after imposing a recombination radius of 2 lattice parameters. The resulting defect density, plotted as a function of PKA energy (Figure 4), decreases smoothly by more than two orders of magnitude over the energy range from 1-200 keV. The number of defects increases approximately linearly with energy, but the cascade volume increases much more rapidly. In the lower part of the energy range the single vacancy distributions tend to become more open and irregular with increasing energy. At high energies the production of multiple, widely separated damage regions leads to larger, sparsely populated enclosing volumes as the energy increases.

However, some aspects of individual damage regions do not change much with energy. The average defect density in the vicinity of each defect is about the same at each energy, even though the cascades become more irregular in shape. This can be examined quantitatively by determining the average local defect density as a function of cascade energy. The number of other defects in a small volume about each defect is averaged over the cascades. In Figure 5 the average number of neighboring vacancies within the third nearest neighbor distance from each vacancy is plotted as a

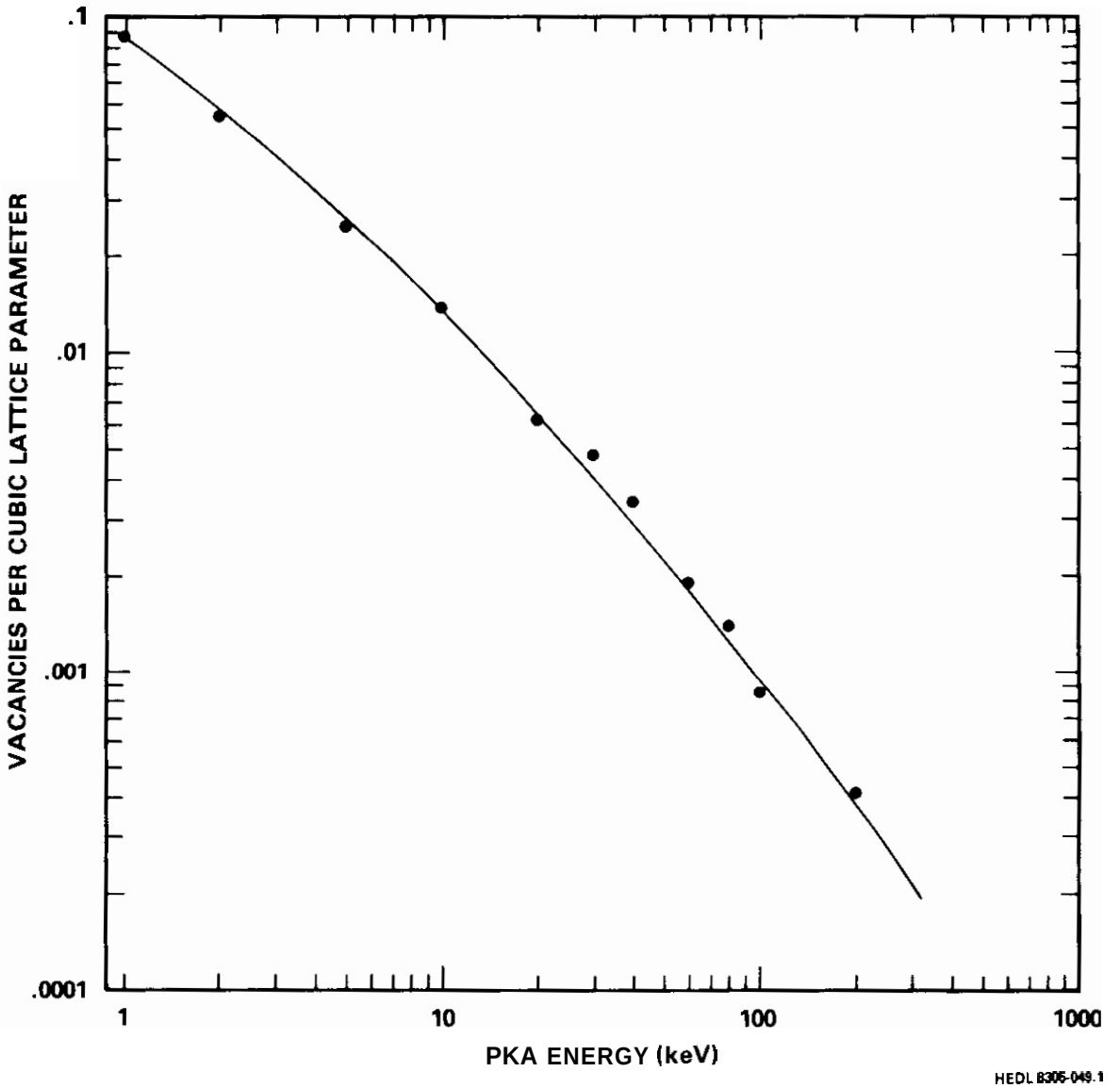

FIGURE 4. The Average Density of Vacancies as a Function of Cascade Energy. The density is the number of vacancies remaining after imposing a recombination radius of 2 lattice parameters divided by the volume of the rectangular parallelepiped oriented along the crystal axes which just encloses the vacancy distribution.

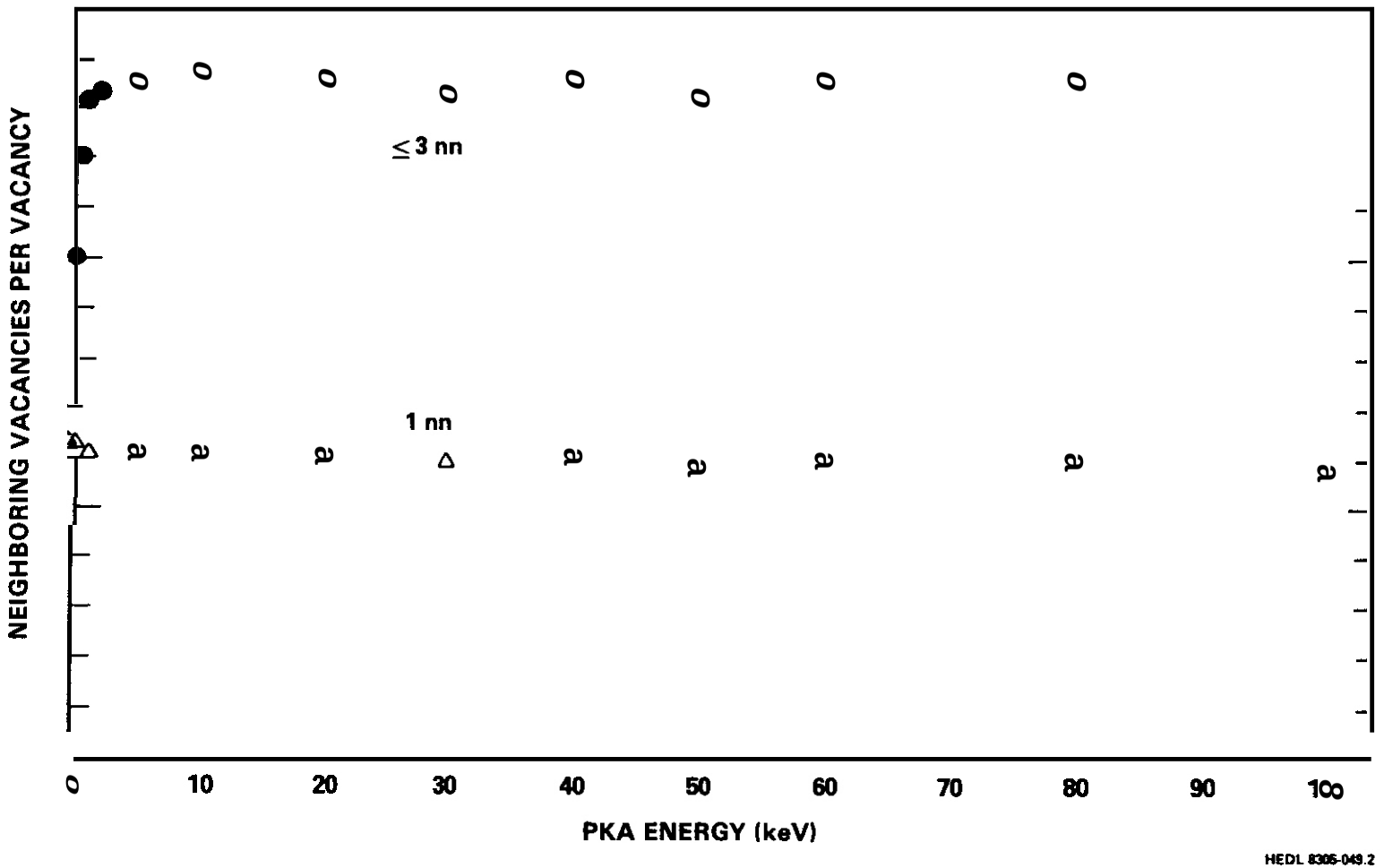

FIGURE 5. The Average Local Density of Vacancies as a Function of Cascade Energy, Defined as the Average Number of Neighboring Vacancies Within the Third Nearest-Neighbor Distance (≤3 nn) of a Vacancy. The average number of nearest-neighboring vacancies (1 nn) is also shown.

function of cascade energy. Above 1-2 keV this value is constant at about 2.7 neighboring vacancies per vacancy. The figure also shows a constant value of 1.2 nearest neighbor vacancies per vacancy.

Figure 6 is a similar plot for interstitials only. Within a spherical volume with a radius of 5 lattice parameters centered on each interstitial, about 1 neighboring interstitial exists, on the average, above 10-20 keV. Only about 5% of Interstitials have neighboring interstitials within one nearest neighbor distance.

The localized defect density analysis indicates quantitatively that the defects see the same average environment, independent of cascade energy, and that the vacancy distribution is more dense than the interstitial distribution.

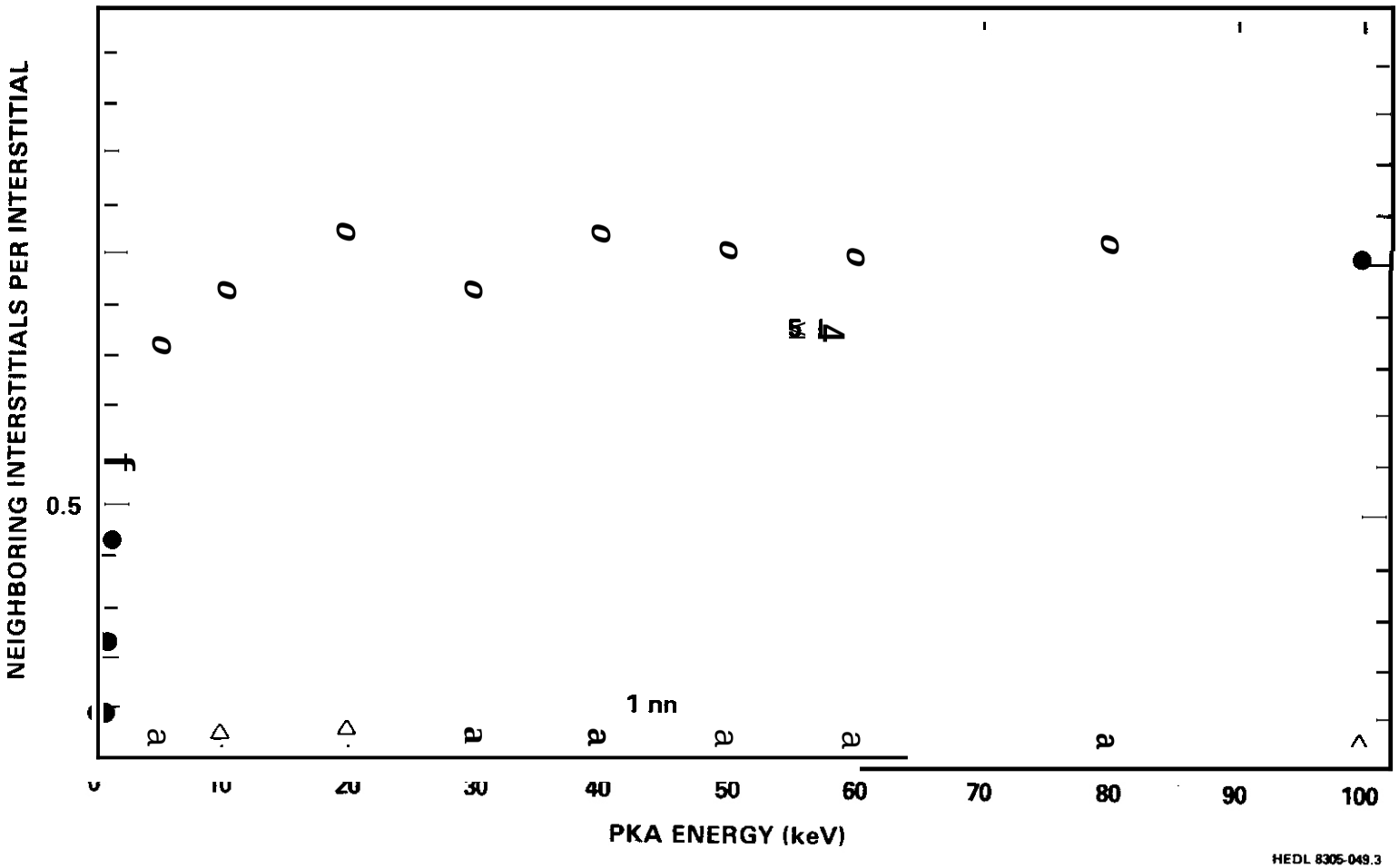

FIGURE 14 The Average Local Density of Interstitials as a Function of Cascade Energy, Defined as the Average Number of Neighboring Interstitials Within 5 Lattice Parameters of an Interstitial (≤ 5 *l.p.*). The average number of nearest-neighboring interstitials (1 nn) is also shown.

6.0 References

1. H.L. Heinisch, HEDL-TME-83-17, Computer Simulation of Displacement Cascades In Copper, 1983.

2. M.T. Robinson and I.M. Torrens, Phys. Rev. B9, p. 5008, 1972.

3. H.L. Heinisch, TMS-AIME Symposium on Radiation Damage Analysis for Fusion Reactors, October 25-28. 1982. St. Louis, MO (also J. Nucl. Mater., in press).

4. M.T. Robinson, DAFS Quarterly Progress Report, Jan-Mar 1980, DOE/ER-0046/1, US Department of Energy p. 55, 1980.

5. J.O. Schiffgens, D.M. Schwartz, R.G. Arlyasu and S.E. Cascadden, Radiat. Eff. 39, p. 221, 1978.

6. H.L. Heinisch, J. Nucl. Mater. 103, p. 1325. 1981.

7. H.L. Heinisch, J. Nucl. Mater. 108, p. 63, 1982.

7.0 Future Work

Future work will investigate quantitative relationships between cascade structures and microstructural features.

8.0 Publications

The full report and "cascade compendium" is available as HEDL-TME-83-17.

14-MEV NEUTRON RADIATION-INDUCED MICROHARDNESS INCREASE IN COPPER ALLOYS

S.J. Zinkle and G.L. Kulcinski (University of Wisconsin - Madison)

1.0 Objectives

The objective of this work is to examine the effect of a high-energy neutron irradiation on damage production in copper alloys. Specific objectives are: 1) to determine the effect of neutron fluence and solute additions on the radiation-induced Vickers microhardness number of copper, 2) to examine the effect of indenter load on the radiation-induced microhardness at low load values, and 3) to correlate microhardness results with resistivity and TEM data.

2.0 Summary

Vickers microhardness measurements have been performed on copper and copper alloy (Cu-5% Al, Cu-5% Mn, Cu-5% Ni) TEM disks which were irradiated at room temperature with 14-MeV neutrons in incremental doses up to a maximum fluence of 2.2 x 10^{21} n/m^2. After an initial incubation period, the radiation-induced hardness was found to be proportional to the square root of neutron fluence for all four metals. This result is in good agreement with previously reported pure copper resistivity data.(1) The incubation period ranged from $\lesssim$ 1 x 10^{20} n/m^2 for the alloys to about 4 x 10^{20} n/m^2 for pure copper. The copper alloys also exhibited a larger radiation-induced hardness increase than the pure copper samples. The Cu-5% Mn samples showed a significantly larger radiation hardening than any of the other samples. Anomalous behavior of the irradiated Cu-5% Mn samples compared to the other alloys was also observed in reported resistivity data.(1)

3.0 Program

Title: Radiation Effects to Reactor Materials

Principal Investigators: G.L. Kulcinski and R.A. Dodd

Affiliation: University of Wisconsin

4.0 Relevant DAFS Program Plan Task/Subtask

Subtask II.B.3.2 Experimental Characterization of Primary Damage State; Studies of Metals

Subtask II.C.6.3 Effects of Damage Rate and Cascade Structure on Microstructure; Low-Energy/High-Energy Neutron Correlations

Subtask II.C.16.1 14-MeV Neutron Damage Correlation

5.0 Accomplishments and Status

5.1 Introduction

Vickers microhardness measurements are a convenient experimental method which can be used to help characterize the extent of radiation damage in crystals. This report describes some of the microhardness results which we have obtained ,as part of a three-pronged approach to analyzing 14-MeV neutron irradiated copper alloys. The first method, resistivity measurements, indicated that the neutron-induced damage was proportional to the square root of neutron fluence for a pure copper sample, while the copper alloys exhibited short-range ordering effects.[1] The results of the third experimental tool, transmission electron microscopy (TEM) observations, will be reported in the next quarterly progress report.

This study is a continuation of research on irradiated copper alloys which was initiated by researchers at HEDL. In their study[2], the authors used microhardness and TEM in an attempt to quantify defect survivability and microstructure. We have included resistivity measurements, the results of which were reported previously[1,3], along with TEM and microhardness measurements at incremental fluences in order to more completely understand the radiation effects shown by the copper/copper alloy samples. Details concerning alloy composition[4], foil preparation[5], and heat treatment and irradiation

procedure[1] have been previously reported.

5.2 Experimental Procedure

Vickers microhardness measurements were performed using a Buehler Micromet® microhardness tester. The standard operating indenter load range of this instrument is from 5g to 500g, with loads down to 1 gram available from the manufacturer. For this investigation, the indenter loading was restricted to be less than or equal to 10 grams in order for the diamond pyramid indentation depth to be less than one-tenth of the nominal TEM foil thickness of 25 nm. At this low indenter load, special care must be taken to ensure that background vibrations do not introduce errors into the measurement. A simple anti-vibration test stand was designed which effectively isolated the microhardness tester from background vibrations down to indenter loads of 1 gram. This test stand assembly is shown in schematic form in Fig. 1. The 1000-kg lead brick base provides the test stand with a large inertia so that all except very low frequency vibrations are damped out. The air pad serves as a dashpot to effectively suppress most of the remaining external vibrations. The remaining cushion materials were chosen on the basis of their different stiffness values. The use of varied materials was found to be effective in eliminating external vibrations. Also, the value of a multiple-interface design, which serves to reflect/dampen vibration waves, was found to be important. The anti-vibration stand was found to be very effective In suppressing background vibrations down to indenter loads of 1 gram as determined by various testing methods (e.g. hardness vs. load curves, reproducibility of hardness results while slamming door, dropping bricks from a designated height, etc.).

A standard sample preparation procedure was developed for all of the TEM disks prior to indentation. Each disk was given a light mechanical polish in a 0.3 μm alumina slurry on a rotating cloth wheel in order to remove the oxide layer and give a relatively smooth surface. The samples were then electropolished in a 33% HNO_3/67% CH_3OH solution cooled to -20°C at an applied potential of

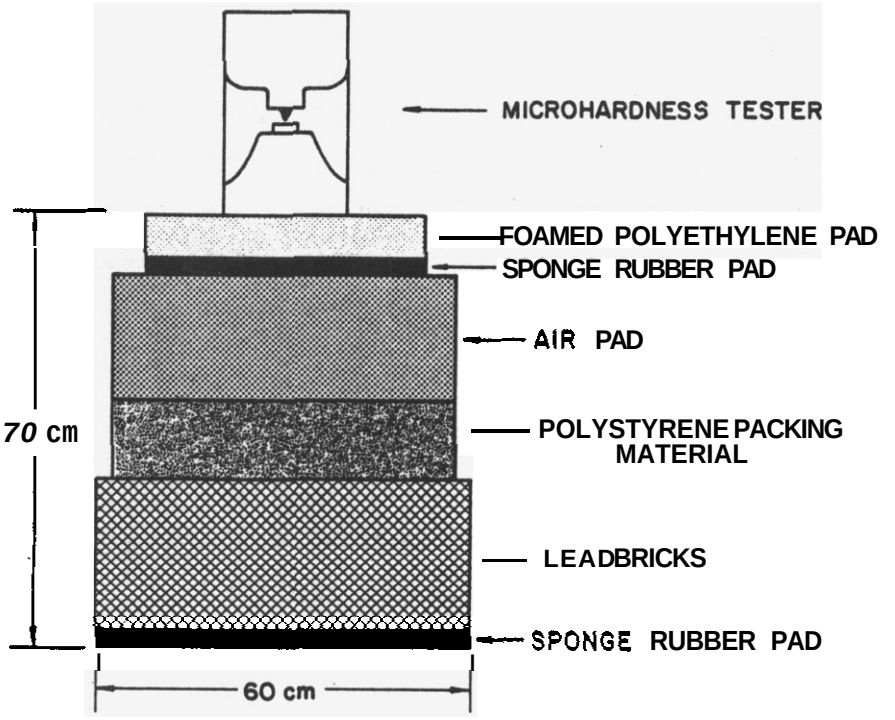

FIGURE 1. Microhardness Anti-Vibration Test Stand.

5V for 5 seconds. The purpose of the electropolish was to remove the work-hardened layer introduced by the mechanical polishing, and also to give an optically smooth surface. The electropolish treatment removed approximately 1-2 μm, which is expected to exceed the work-hardened layer in copper for the type of mechanical polishing which was utilized.[7]

Table 1 shows the grain size of each of the four metals irradiated at RTNS-II as detennined by Heyn's Procedure (line intercept method). A total of 250 to 500 grain boundary intercepts in at least 20 different viewing areas were sampled to deternine the average grain sire for each metal.

A minimum of 60 indentations were made on four different TEM disks for each metal at every fluence level and for the control samples. A 12 second

TABLE 1

RTNS-II SAMPLE GRAIN SIZE

Copper	CU-5% Al	Cu-5% Mn	Cu-5% Ni
13 μm	23 μm	22 μm	12 μm

indentation time was used throughout. All measurements were made by the same operator in order to minimize the effect of different observers' biases. The lengths of the diagonals were measured at a magnification of 600X using a calibrated eyepiece accurate to ± 0.2 μm. Both diagonals of the indentation were measured twice and the results averaged in order to minimize measurement errors. The chisel tip of the Vickers diamond was found to less than 0.2 μm, as checked by SEM methods. Several TEM disks were re-examined at different time periods and on different days of the week in order to check the effectiveness of the anti-vibration test stand and also to determine the reproducibility of the results. Agreement on the Vickers microhardness (H_v) for a single disk was typically found to be within about 1 kg/mm^2. A larger variation was noted between different TEM disks which had been exposed to identical heat treatment and irradiation histories -- typical standard deviations about the mean for a set of 4 disks were 2-3 kg/mm^2.

5.3 Experimental Results

The Vickers microhardness values obtained for the control and irradiated foils at an indenter load of 10 grams are summarized in Table 2. The table also includes the standard deviation for each set of 4 disks which were examined (Each value given in the table is the result of the measurement of at least 60 indentations). The microhardness value for the unirradiated pure copper was 56.7 kg/mm^2, while the copper alloy control samples all measured about 53.5 kg/mm^2 at an indenter load of 10g. It may be noted that the microhardness values for the alloy and pure copper control samples are equivalent within quoted error bars. The value of H_v for pure copper is in good agreement with the unirradiated value measured by other investigators[6] at an indenter

TABLE 2

VICKERS MICROHARDNESS RESULTS (10-GRAM LOAD)

Dose	Sample H_v (kg/mm^2)			
10^{20} n/m^2	Copper	Cu-5% Al	Cu-5% Mn	Cu-5% Ni
control	56.7 ± 4.3	53.8 ± 0.9	53.4 ± 2.5	53.4 ± 2.8
1	56.3 ± 0.8	57.2 ± 0.8	62.6 ± 4.6	57.3 ± 0.7
4	58.6 ± 2.8	62.7 ± 1.2	73.6 ± 2.2	63.8 ± 1.4
10	68.9 ± 1.6	74.1 ± 1.7	85.8 ± 0.4	69.6 ± 1.7
20	78.2 ± 3.6	82.3 ± 1.1	90.2 ± 3.5	78.3 ± 4.2

loading of 50 grams. However, the hardness values for the unirradiated alloys (in particular Cu-5% Al and Cu-5% Mn) are significantly lower than previously reported values. The reason for this discrepancy is uncertain, as the materials were obtained from the same lot and were given identical heat treatments.

As can be seen from Table 2, 14-MeV neutron irradiation to a fluence of 2 x 10^{21} n/m^2 induces significant hardening in copper and copper alloys -- microhardness changes are on the order of 50% of the unirradiated microhardness value. The fluence dependence of the microhardness change is shown in Fig. 2 for an indenter load of 10 grams, along with representative error bars. Results obtained at an indenter loading of 5g (to be reported separately) showed trends similar to the 10g data. Following a short incubation period, the data for all four metals scales linearly with the square root of neutron fluence. The duration of the incubation period is less than 1 x 10^{20} n/m^2 for the copper alloys, while for pure copper it is about 4 x 10^{20} n/m^2. Cu +5% Mn exhibits significantly larger radiation hardening as compared to the other metals at the fluence levels investigated. This alloy may also be starting to approach a saturation hardness value at the highest fluence examined, but without higher fluence data this conclusion is speculative.

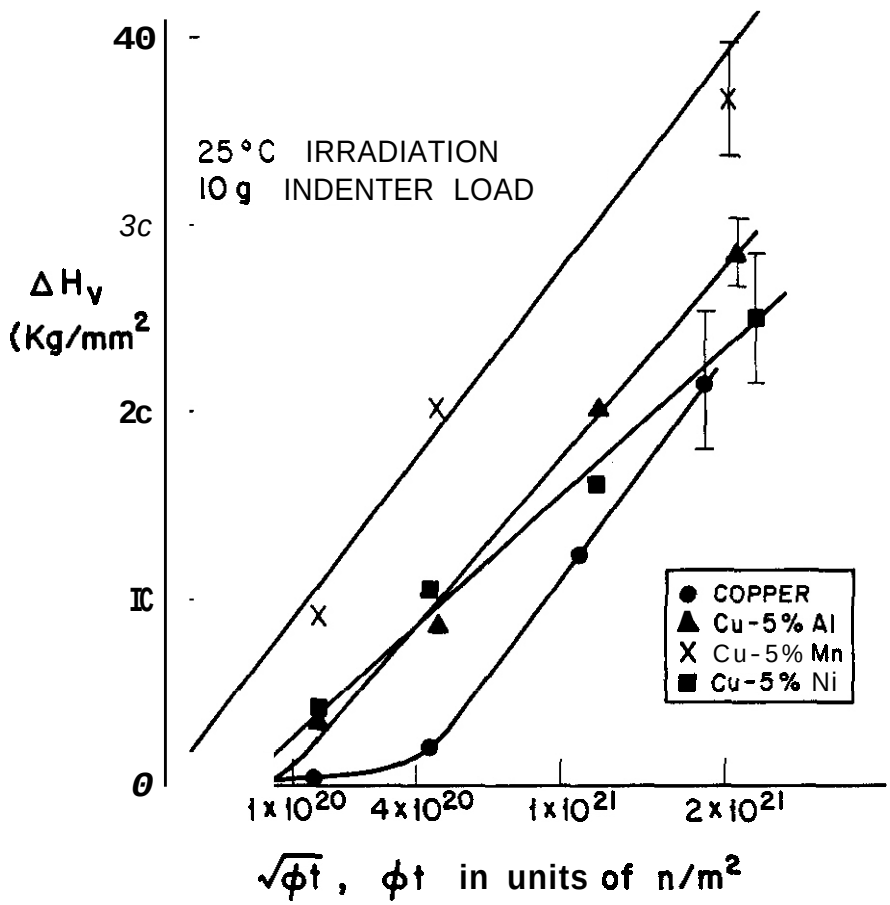

FIGURE 2. Change in Vickers Microhardness vs. Square Root of 14-MeV Neutron Fluence.

5.4 Discussion

The general fluence dependence of the radiation-induced change in Vickers microhardness is in good agreement with a recent theoretical model developed by Ghoniem et al.[8] The model predicts that radiation hardening should scale linearly with the square root of neutron fluence following a short incubation period. The data obtained from resistivity and microhardness measurements as a function of fluence are compared in Fig. 3 with tensile specimen results obtained by Mitchell et al[9] for copper irradiated at room temperature with 14-MeV neutrons. From this figure it can be seen that the resistivity results and tensile data are in good agreement. The microhardness results curve is

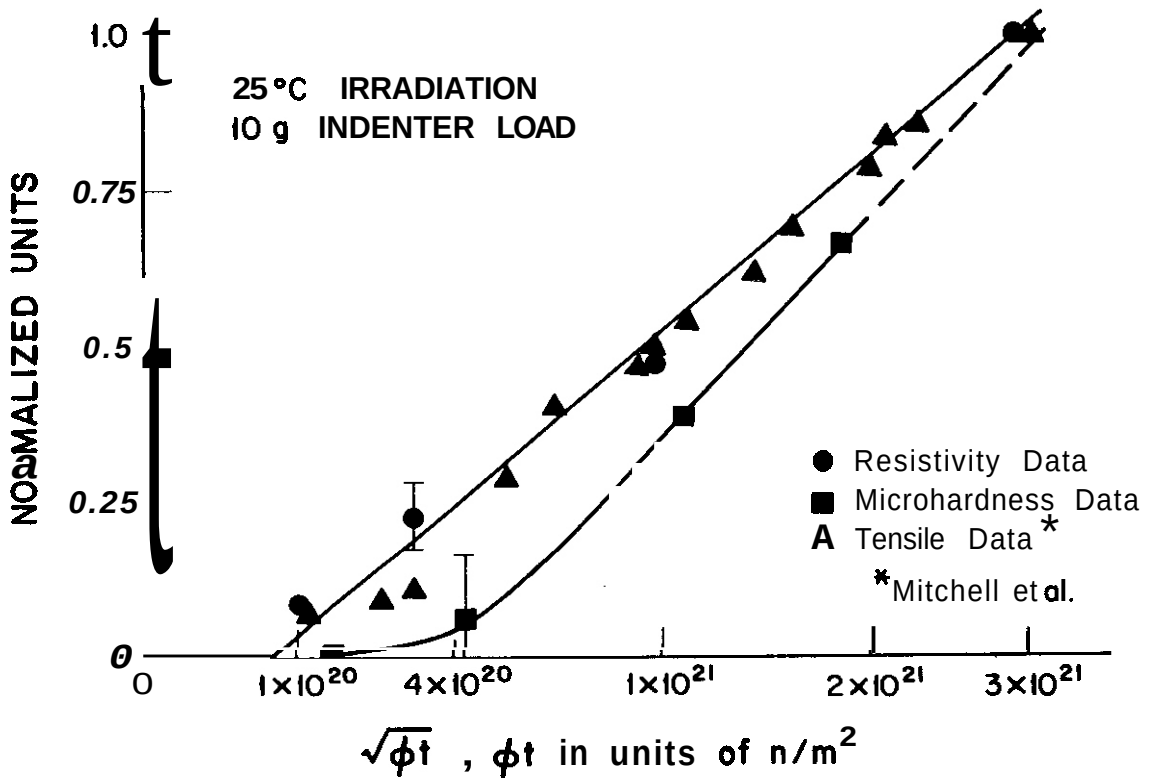

FIGURE 3. Change in Resistance, Microhardness, and Yield Strength vs. Square Root of 14-MeV Neutron Fluence for Copper.

somewhat at odds with the above-mentioned data, although there is agreement within the quoted error bars. It is believed that the slight discrepancy of the microhardness data with regard to the other results is due to the well-known low-load microhardness surface effect (see, e.g., Ref. 10). Evidence indicating that this is the case, along with a discussion of the low-load microhardness phenomena, will be presented in the next quarterly progress report.

The roughly equal slopes for all four metals in the curve of microhardness change vs. square root of neutron fluence (Fig. 2) may be seen as an indication that there is equivalent damage production rates in these materials following the initial transition period. Reasonably good agreement has been

observed with tensile data[9] using the correlation[2] $\Delta\sigma_Y = 3.27\ \Delta H_V$.

5.5 Conclusions

It appears that quite reproducible Vickers microhardness results may be obtained at low indenter loads when adequate precautions are taken to eliminate background vibrations and when a statistically significant number of indentations are sampled. Microhardness measurements are a ueful tool which may be utilized to help characterize irradiation damage in conjunction with other techniques. However, care must be taken when attempting to extrapolate measurements made at low loads to bulk values.

6.0 References

1. S.J. Zinkle and G.L. Kulcinski, "14-MeV Neutron Irradiation of Copper Alloys," DAFS Quarterly Progress Report DOE/ER-0046/8 (February 1982) p. 48.

2. H.R. Brager, F.A. Garner and N.F. Panayotou, J. Nucl. Mater., 103 and 104 (1981), 995.

3. S.J. Zinkle and G.L. Kulcinski, "14-MeV Neutron Irradiation of Copper Alloys," DAFS Quarterly Progress Report DOE/ER-0046/9 (May 1980), p. 93.

4. H.R. Brager et al., "Microstructural Development in Copper Irradiated in RTNS-II," 9th DAFS Quarterly Progress Report DOE/ER-0046/1 (May 1980), 76.

5. N.F. Panayotou et al., "RTNS-II Irradiation Program Status," DAFS Quarterly Progress Report DOE/ET-0065/5 (May 1979), 112.

6. H.R. Brager et al., "Microstructural Development for Copper Alloys Irradiated in RTNS-II," DAFS Quarterly Progress Report DOE/ER-0046/3 (November 1980), p. 81.

7. K.C. Thompson-Russell and J.W. Edington, Practical Electron Microscopy in Materials Science, Monograph 5, Phillips Technical Library, p. 2, 1977.

8. N.M. Ghoniem et al., "Hardening of Irradiated Alloys Due to Simultaneous Formation of Vacancy and Interstitial Loops," Proc. of 11th International Symposium on Effects of Radiation on Materials, STP 782, Scottsdale, AZ, June 27-29, 1982, p. 1054.

9. J.B. Mitchell et al., "DT Fusion Neutron Radiation Strengthening of Copper and Niobium," Radiation Effects and Tritium Technology for Fusion Reactors, J.S. Watson and F.W. Wiffen (Eds), Gatlinburg, TN, (Oct. 1-3, 1975), Vol. II, p. 172.

10. B.W. Mott, Micro-Indentation Hardness Testing, Butterworths Scientific Publications, London, (1956).

7.0 Future Work

Vickers microhardness measurements obtained at an indenter loading of 5g will be compared to the present results in the next quarterly progress report. These findings will be coupled with literature results in an attempt to correlate low indenter load values with data obtained at higher loads. TEM disks at various fluences will be examined in an electron microscope in order to determine visible defect cluster size and density as a function of 14-MeV neutron fluence.

8.0 Publications

The copper/copper alloy resistivity, microhardness and TEM data will be presented at the 3rd Topical Meeting on Fusion Reactor Materials, Albuquerque, NM, September 19-22, 1983. An abstract has been submitted to the Symposium on the Use of Nonstandard Subsized Specimens for Irradiation Testing, Albuquerque, NM, September 23, 1983, which deals with the correlation of low-load microhardness values with bulk values.

9.0 Acknowledgements

The authors would like to thank the Metallurgical and Mineral Engineering Department, University of Wisconsin, for the use of the microhardness tester. This work was performed under appointment to the Magnetic Fusion Energy Technology Fellowship program which is administered for the U.S. Department of Energy by Oak Ridge Associated Universities.

C H A P T E R 3

REDUCED ACTIVATION MATERIALS

ACTIVATION OF COMPONENTS OF A FUSION ALLOY

F. M. Mann (Westinghouse Hanford Company) and W. E. Kennedy, Jr. (Battelle Pacific Northwest Laboratory)

1.0 Objective

The objective of this work is to determine the activation of the constituents of potential fusion alloys so as to guide metallurgists in selecting low activation materials.

2.0 Summary

As the NRC has based its isotopic concentration limits for land disposal of low-level radioactive wastes on present experience, limits for those isotopes not covered by the NRC regulation (10 CFR 61), but which would be produced in a fusion environment, were determined. These limits severely restrict the use of Al as a prime constituent of an alloy and further restrict Mo as a minor constituent.

3.0 Program

Title: Irradiation Effects Analysis (AKJ)
Principal Investigator: D. G. Doran
Affiliation: Westinghouse Hanford Company

4.0 Relevant DAFS Program Plan Task/Subtask

No relevant task.

5.0 Accomplishments and Status

In past quarterly reports, results were presented of calculations of the activation of various elements at the STARFIRE first-wall position.[1,2] In addition, the resulting isotopic concentrations were compared with the NRC

regulation (10 CFR 61) to determine limits on the initial elemental composition of the first wall.

The NRC regulation, however, is based upon present experience, mainly LWRs and medical facilities. Therefore, some radioactive daughters presently considered unimportant under the regulation will almost surely be regulated when fusion devices become more powerful.

A brief investigation of such isotopes was conducted. Since it was not our intent to duplicate the complex exposure scenario analysis used by the NRC, disposal limits for these radionuclides were developed using a ratioing technique based on ^{59}Ni. As a check of the adequacy of this technique, ^{60}Co and ^{63}Ni disposal limits were calculated and found to be in good agreement with the detailed NRC analysis.

Using the calculated activation from References 1 and 2 and these additional limits on burial, new potential limitations on initial compositions of first wall materials can be estimated (see Table 1). Note that the data in this table are for one specific exposure, 10 $MW\text{-}y/m^2$ (the results are generally proportional to the exposure). The differences from the earlier results in Reference 2 are lower limits for Fe, Mo, and Pb, and new limits for B, Al, and S. The limit found for Al would restrict its use as the prime constituent of a first wall exposed to significant fluences if near-surface burial were desired. The limit on Mo, already very low, is reduced by an order of magnitude. The other new limits should not greatly restrict alloy designers.

TABLE 1

ESTIMATED MAXIMUM FRACTIONAL WEIGHT CONCENTRATIONS
PER 10 MW-yr/m^2 (10 CFR 61) (All Tritium Expelled)

Element	Class A Disposal	Class C Disposal
B*	.32[a]	3.18[a]
C	62.	620.
N	.00033(330 ppm)	.0033
O	.31	3.1
Mg	.0096	[b]
Al	.0036[a]	.036[a]
Ti	26.	[b]
S	.4[a]	4.0
V	.37	[b]
Cr	.00064(640 ppm)	[b]
Mn	.0015	[b]
Fe	.4[a]	4.0[a]
co	7.5(-7)[c](.75 ppm)	[b]
Ni	4.(-5)(40 ppm)	.0091
cu	6.(-6)(6 ppm)	.0012
Zr	1.2(-5)(12 ppm)	2.1
Nb	2.9(-7)(.29 ppm)	2.9(-6)[c](2.9 ppm)
Mo	4.9(-6)(.5 ppm)[a]	4.9(-5)(49 ppm)[a]
Ta	.0025	[b]
W	2.3(-5)(23 ppm)	[b]
Pb	.0031[a]	.031[a]

[a] Limit set by BNWL study.

[b] Limited by practical considerations, such as the effects of external radiation and internal heat generation on transport, handling, and disposal.

[c] *X(Y) should be read as X x 10^Y.

Underlined elements may be affected by new regulations. No limits on Li, Be, Si, P, Sn, and Hf.

6.0 References

1. F. M. Mann, "Activation of Components in a Fusion Alloy", Damage Analyses and Fundamental Studies Quarterly Progress Report, October - December 1982, DOE/ER-0046/12 (1983) p. 69

2. F. M. Mann, "Activation of Components in a Fusion Alloy", Damage Analyses and Fundamental Studies Quarterly Progress Report, January - March, 1983, DOE/ER-0046/13 (1983) p. 63

7.0 Future Work

Activation calculations for a TASKA first-wall position will be performed to determine the effect of neutron spectrum on activation. Also, blanket positions in TASKA and STARFIRE will be examined.

C H A P T E R 4

FUNDAMENTAL MECHANICAL BEHAVIOR

EFFECT OF NEUTRON AND HELIUM IRRADIATION ON FRACTURE MODES

T. Hanamura and W. A. Jesser (University of Virginia)

1.0 Objective

The objective of this work is to determine the crack opening modes during in-situ HVEM tensile testing and how it is influenced by test temperature and neutron and helium irradiation.

2.0 Summary

Neutron and helium irradiation were found to hinder Mode II failure and increase Mode I cracking instead. Over the temperature range studied (25-600°C) irradiated specimens showed that Mode II intergranular failure was absent and intergranular failure occurred mostly by a Mode I crack opening. In unirradiated specimens tested under the same tensile conditions as for the irradiated specimens, Mode II crack opening at the grain boundaries was present.

3.0 Program

Title: Simulating the CTR Environment in the HVEM
Principal Investigators: W. A. Jesser and R. A. Johnson
Affiliation: University of Virginia

4.0 Relevant DAFS Program Plan Task/Subtask

Task II.C.13 Effects of Helium and Displacements on Crack Initiation and Propagation

5.0 Accomplishments and Status

5.1 Introduction

In a fusion reactor neutron and helium ions from the plasma that strike a first wall are known to cause a number of serious material problems, one of which is the embrittlement of the material due to a weakening of grain boundaries. The weakening of grain boundaries can cause intergranular fracture by grain boundary sliding through Mode II crack propagation or by other opening modes including a mixed mode. To understand this mechanism, in this investigation crack opening mode is used as a crack propagation parameter'') like other parameters which have been investigated[2-4]. The intent of this paper is to understand the mechanism of crack initiation and propagation in neutron- and helium-irradiated stainless steel, using in-situ HVEM tensile testing of microspecimens under various conditions of irradiation-induced microstructure and temperature, and to determine the effect of irradiation on crack opening mode.

5.2 Experimental Details

In this investigation either type 316 or type 304 stainless steel was investigated. Type 316 stainless steel was helium ion-irradiated for in-situ tensile testing in the HVEM. Type 304 stainless steel was neutron-irradiated and in-situ tensile tested after the irradiation. The type 316 stainless steel specimens were vacuum annealed at 1000°C for one hour at a pressure less than 1×10^{-4} Pa and then punched into microtensile specimens 12.5 mm long, 2.5 mm wide and 40 μm thick. After punching, the specimens were electropolished in a 90% acetic-10% perchloric acid solution at 18°C and at 20 mV in a Tenupol electropolishing apparatus. The helium irradiations were conducted at temperatures estimated from ion beam heating to be less than 300°C[5,6] by bombarding the electropolished specimens with 80 keV helium ions to fluences up to $\simeq 3 \times 10^{18}$ cm^{-2}. In addition, some specimens were given a post-irradiation anneal in vacuum (10^{-4} Pa or better) to coarsen the radiation-induced microstructural features. The neutron-irradiated specimens were from a control rod

thimble from the EBR-II reactor. These specimens were electropolished in the same solution as above but in a Fischione Jet electropolishing apparatus. The specimens investigated here were designated by ORNL as 3T-2b and 3T-5b. The 3T-2b specimen was neutron-irradiated at 428°C to a fluence of 1.0×10^{23} neutrons $(> .1\ MeV)/cm^2$ and the 3T-5b specimen was neutron-irradiated at 371°C to a fluence of 6.5×10^{22} neutrons $(> .1\ MeV)/cm^2$. Tensile testing in the HVEM was carried out in a hydraulically operated load-elongation tensile stage which is capable of heating the specimen to about 600°C.[7] Data were obtained from still micrographs and video tape during the dynamic observation of crack propagation. From these sources the mode of crack opening was determined.

5.3 Experimental Results and Discussion

Crack opening displacement vectors were obtained by analysis of a sequence of pictures during in-situ HVEM tensile testing from video tape and still pictures of electron images on the HVEM screen. The crack opening displacement vector, $\vec{D}$, is defined as the difference vector between two vectors: one obtained from one micrograph by connecting a reference point on one crack flank to a corresponding reference point on the opposite crack flank, and another vector obtained from the same two points on the crack flank but measured from a micrograph later in the sequence. The direction of $\vec{D}$ is where it points to the tip of the vector obtained in the latter micrograph of the pair. The reference points are chosen as any pair of easily distinguishable points located within 10 μm of the tip of each crack.

In order to describe the crack mode, it is convenient to define additional crack characteristics which are shown in Figure 1-A. In this figure, the crack angle is (H) and the crack tip angle is e. The crack propagation direction, $\hat{P}$, is defined as the bisector of the crack flank angle, (H), and points into the material. The crack directional angle α is included between $\hat{P}$ and the tensile axis, and the angle between the tensile axis and $\vec{D}$ is denoted by β. The sum of α and β is denoted as e', i.e., θ' is the angle between $\vec{D}$ and $\hat{P}$.

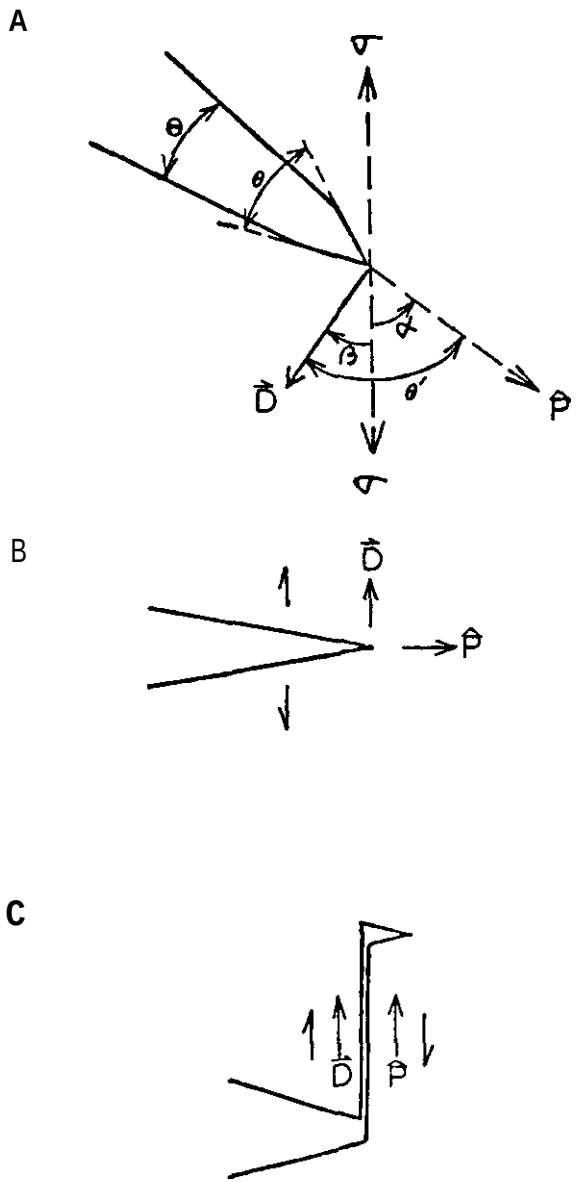

FIGURE 1: (A) Schematic Drawing of a Crack Tip. The crack opening displacement is $\vec{D}$, the crack propagation direction is $\hat{P}$, the angle between the tensile axis and $\hat{P}$ is a, that between the tensile axis and $\vec{D}$ is β, $\alpha + \beta = \theta'$, the crack angle is (H) , and the crack tip angle is e. (B) Schematic Diagram of a Pure Mode I Crack Propagation. The angle between $\vec{D}$ and P is 90°. (C) Schematic Drawing of Pure Mode II Crack Propagation. The angle between $\vec{D}$ and $\hat{P}$ is 0".

Each displacement vector, $\vec{D}$, was separated into a segment, $\bar{D}_{\parallel}$, parallel to the direction of crack propagation, and a perpendicular segment $D_{\perp}$. Using the angle θ', it can be expressed as $D_{\perp} = D \sin \theta'$ which corresponds to Mode I crack opening and similarly $D_{\parallel} = D \cos \theta'$ which corresponds to Mode II crack opening. Since $D_{\perp}^2 + D_{\parallel}^2 = D^2$, the % Mode I character of a crack can be defined as $100 \cdot D_{\perp}^2/D^2$, which is $100 \sin^2 \theta'$, and the % Mode II character as $100 \cdot D_{\parallel}^2/D^2$, which is $100 \cdot \cos^2 \theta'$. Figure 1-B and 1-C show these pure Mode I and Mode II cases respectively. Any Mode III component is parallel to the electron beam and is not revealed by the present technique.

Figure 2 shows the graph of % Mode I versus crack directional angle, a, for the cases of an unirradiated type 316 stainless steel specimen tested at room temperature, a neutron-irradiated type 304 stainless steel specimen (3T-5b 83) tested at 400°C, and another neutron-irradiated specimen (3T-5b #1) tested at room temperature. A transition area from predominantly Mode I crack propagation to Mode II crack propagation was determined to be around $a \simeq 30°$ for the unirradiated specimen tested at room temperature. The neutron-irradiated specimen tested at room temperature showed the transition area at a higher angle of α compared to the case of the unirradiated specimen tested at room temperature. In the case of the neutron-irradiated specimen tested at 400°C, the observed values of a were close to $\alpha = 90°$, and all the cracks showed a character of nearly 100% Mode I. This temperature corresponds to channel fracture in **bulk** specimens which have been neutron-irradiated. In the microtensile specimens, the cracks appear sharp and propagate in straight directions mostly across grains. As a reference curve for comparison with the data points, a smooth curve is superimposed on the plot. This curve shows the idealized case of $\vec{D}$ parallel to the tensile axis for all values of α, i.e., $\beta = 0$ for all α. The displacement vector $\vec{D}$ may be thought of as locating the direction of the local tensile axis so that $\vec{D}$ parallel to the tensile axis (i.e., $\beta = 0$) represents no deviation of the macroscopic tensile axis from the microscopic one. One example of such a situation is a rigid displacement of one crack flank from its opposite, mating crack flank and could be approximated by a completely brittle crack propagation through weak material in which constraints and local

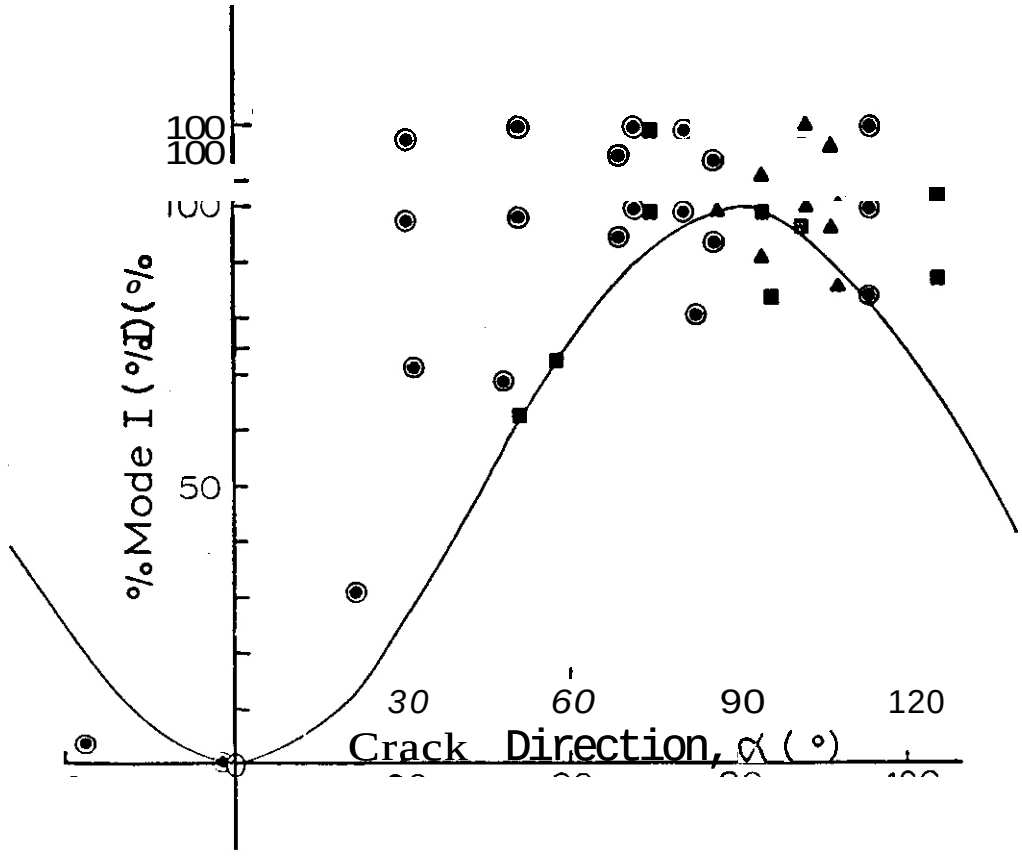

⊙ Unirradiated 316 SS tested at R.T.

▲ Neutron-irradiated 304 SS (3T-5b, #3) tested at 400°C (dose = 6.5 x 10^{22} neutrons • cm^{-2} at 371°C)

■ Neutron-irradiated 304 SS (3T-5b, #1) tested at R.T. (dose = 6.5 x 10^{22} neutrons • cm^{-2} at 371°C)

FIGURE 2: Graph of Observed % Mode I Opening of a Given Crack Plotted as a Function of its Propagation Angle a. Specimens were type 304 stainless steel irradiated with neutrons. The smooth curve represents a rigid displacement of the crack flanks in the direction parallel to the tensile axis, i.e., $\beta = 0$.

plastic deformation which might lead to bending and effective rotations are negligible.

The effect of helium irradiation on crack mode is shown in Figure 3, which is a graph of % Mode I character versus crack directional angle, a, for four type 316 stainless steel specimens: an unirradiated one tested at room temperature,

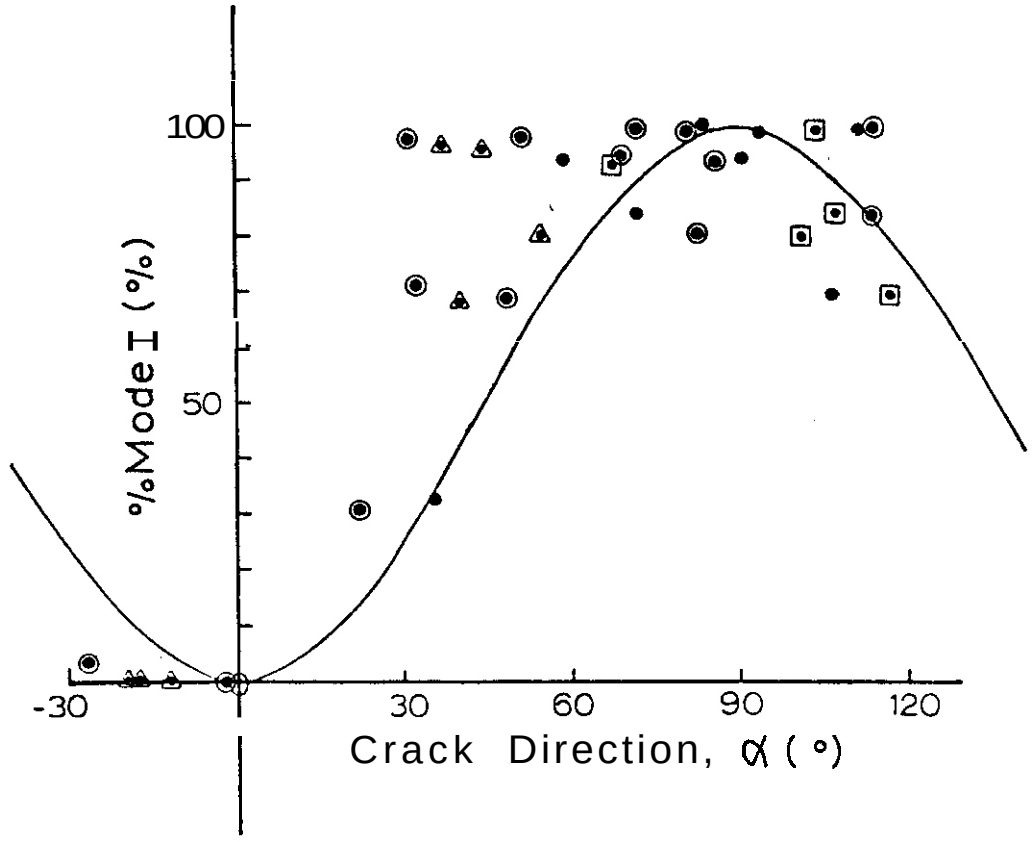

⊙ Unirradiated 316 SS tested at R.T

A Post irradiation annealed 316 SS tested at R.T.
(flux = 1.4 x 10^{15} ions • $cm^{-2}sec^{-1}$; dose = 4.2 x 10^{17} ions • cm^{-2})
(annealed at 900°C for ∿ 10 sec)

• No post irradiation annealing, 316 SS tested at R.T.
(flux = 3.3 x 10^{14} ions • $cm^{-2}sec^{-1}$; dose = 1.0 x 10^{17} ions • cm^{-2})
(no annealing)

⊡ Post-irradiation annealed 316 SS, tested at 250°C
(flux = 3.0 x 10^{14} ions • $cm^{-2}sec^{-1}$; dose = 1.0 x 10^{17} ions • cm^{-2})
(annealed at 300°C)
(mixed fracture mode)

FIGURE 3: Graph of Observed % Mode I Opening of a Given Crack Plotted as a Function of its Propagation Angle *a.* Specimens were type 316 stainless steel irradiated with 80 keV helium ions. The smooth curve represents a rigid displacement of the crack flanks in a direction parallel to the tensile axis, i.e., $\beta = 0$.

an annealed helium-irradiated one tested at room temperature (flux = 1.4 x 10^{15} ions cm^{-2} sec^{-1}, dose = 4.2 x 10^{17} ions cm^{-2}, followed by annealing at 900°C for ∿ 10 sec), a helium-irradiated one tested at room temperature (flux = 3.3 x 10^{14} ions cm^{-2} sec^{-1}, dose = 6.0 x 10^{17} ions cm^{-2}, and no post-irradiation annealing), and a helium-irradiated one tested at 250°C (flux = 3.0 x 10^{14} ions cm^{-2} sec^{-1}, dose = 1.0 x 10^{17} ions cm^{-2}, followed by annealing at 300°C for 30 min). Mode II grain boundary sliding was observed only in the case of the unirradiated specimen tested at room temperature and the annealed helium-irradiated one tested at room temperature. From the six specimens tested in this investigation, it is seen that when α is small, i.e. β is almost parallel to the tensile axis, the crack opening is close to 100% Mode II. In this experiment, all the observed 100% Mode II cracks were along grain boundaries, which means all the 100% Mode II crack propagations correspond to grain boundary sliding. When the observed grain boundary sliding occurred, all cases showed that strong Mode I character cracks preceded the 100% Mode II cracks and initiated the Mode II cracking by intersecting the grain boundaries at an angle near 90° as schematically shown in Figure 1-C.

In the case of the neutron-irradiated specimens (3T-5b #3) tested at 400°C and (3T-5b #1) tested at room temperature, and in the case of the annealed helium-irradiated type 316 stainless steel specimen tested at 250°, the data points were closer to the smooth curve than other cases. This is especially true for the neutron-irradiated one (3T-5b #3) tested at 400°C, which also showed most of the data points lying in a region of α close to 90". Accordingly, all the points for this case correspond to the fracture which is close to 100% Mode I fracture.

A further indication of brittleness is the flow localization at grain boundaries which manifests itself as intergranular failure. In this investigation, two specimens exhibited a significant amount of intergranular failure, the helium-irradiated one tested at 250°C and the neutron-irradiated one (3T-5b #3) tested at 400°C. Both of these specimens failed largely by nearly pure Mode I crack propagation and exhibited a significant amount of intergranular failure.

The range of crack directions for the helium case was wider than that for the neutron case, which showed a narrow range of values of α near 90°.

It is also important to note that a small amount of intergranular failure occurs in the ductile, unirradiated specimen through the mechanism of grain boundary sliding. This Mode II mechanism of intergranular failure is replaced by a Mode 1 mechanism of intergranular failure when the specimen is subjected to irradiation as seen in Figure 2 by comparing the case of the unirradiated specimen tested at room temperature and the case of the neutron-irradiated specimens, especially the one tested at 400°C. It is possible, however, to conduct a post-irradiation anneal of the helium-irradiated specimen and thereby restore the small amount of Mode II intergranular failure found in ductile unirradiated specimens as seen in Figure 3 by comparing the case of the unannealed helium-irradiated one tested at room temperature and the case of the annealed helium-irradiated one tested at room temperature. A further effect of the post-irradiation annealing is to favor ductile crack propagation characteristics which are typified by the crack propagation data for the unirradiated specimen.

Displacement vector changes with distance to the crack tip. The displacement vector was measured as a function of distance to the crack tip and it was found that as the measurement is made closer to the crack tip, the % Mode I character of the crack opening increases gradually as shown in Figure 4. In this figure, the lowest point in a series of points is $\simeq$ 10-15 μm from the crack tip and the highest point in a given series is 1 μm from the tip. This result confirms that the choice of reference points for calculating $\vec{D}$ is not critical.

5.4 Theoretical Development

In this investigation, grain boundary sliding was observed in the case of the unirradiated type 316 stainless steel tested at room temperature and the post helium irradiation annealed type 316 stainless steel tested at room temperature, and only when $|\alpha| < 30°$. To understand the initiation and propagation

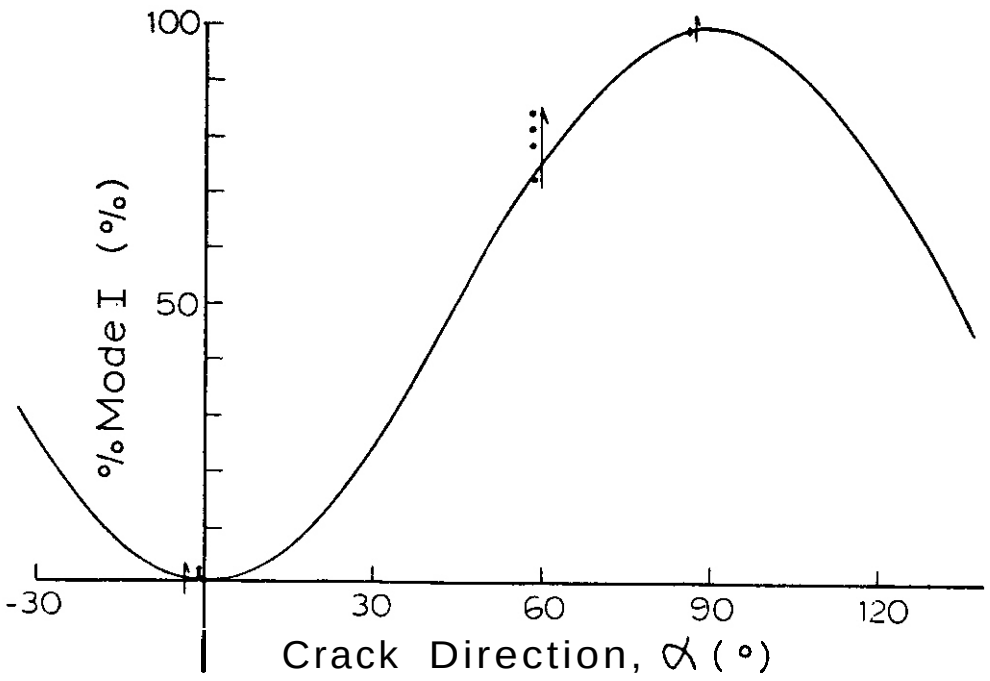

FIGURE 4: Relationship Between % Mode I and Distance to Crack Tip. ←: Direction to the Crack Tip. As the position to measure the displacement vector gets closer to the crack tip, % Mode I is seen to increase. The lowest point in a series is ≃ 10–15 μm from the tip and the highest point is 1 μm from the tip.

mechanisms of grain boundary sliding, it is important to develop a criterion which explains the condition to produce grain boundary sliding, and so, in this paper, a new criterion is developed.

In this theory of a maximum stress criterion, it is assumed that grain boundary sliding occurs when the boundary lies in an orientation near that corresponding to a maximum local shear stress produced by the geometry of a crack in the presence of a load. To obtain the shear stress distribution in front of a crack tip, first consider the local stress in front of the crack tip, which can be expressed in the notation in Figure 5 as[8]

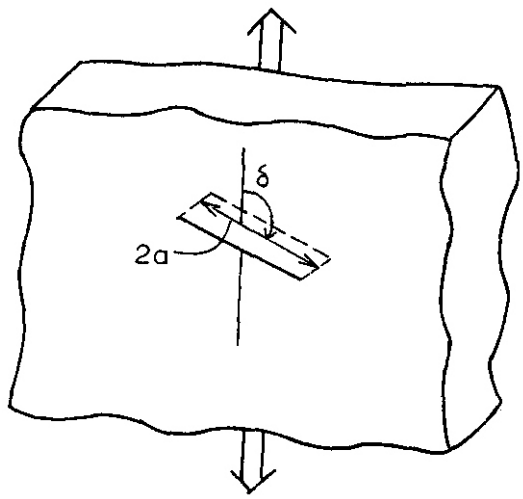

FIGURE 6: Crack Inclined δ Degrees to the Tensile Direction.

$$k_2 = \sigma a^{\frac{1}{2}} \sin \delta \cos \delta \tag{4}$$

where σ = uniaxial tensile stress, δ = inclined angle of the crack against the tensile direction, 2a = length of the crack. So, the total shear stress at a crack tip which is loaded in a mixed Mode I and II case can be expressed in linear elasticity as the sum of ${}_{I}\tau_{r\theta"}$ and ${}_{II}\tau_{r\theta"}$, i.e.,

$$\begin{aligned} \tau_{r\theta"} &= {}_{I}\tau_{r\theta"} + {}_{II}\tau_{r\theta"} \\ &= \sigma\sqrt{\frac{2a}{r}}\,[\sin^2 \delta \sin \theta" \cos(\theta"/2) \\ &\quad + \sin \delta \cos \delta(3 \cos \theta" - 1)\cos(\theta"/2)] \end{aligned} \tag{5}$$

In this analysis, δ is taken to be the angle between the existing crack direction and the tensile direction, and α is taken to be the angle with respect to the tensile axis of the new crack propagation direction, i.e., the next crack segment which is to undergo grain boundary sliding induced by the maximum shear stress at the tip of the existing crack. Further, $\theta"$ is taken to be the angle between the crack propagation direction of the original crack segment as shown in Figure 7. The relationship among these parameters is:

$$\alpha + \theta" = \delta \tag{6}$$

Using equation (5), the variation of $\tau_{r\theta"}$ as a function of $\theta"$ can be calculated

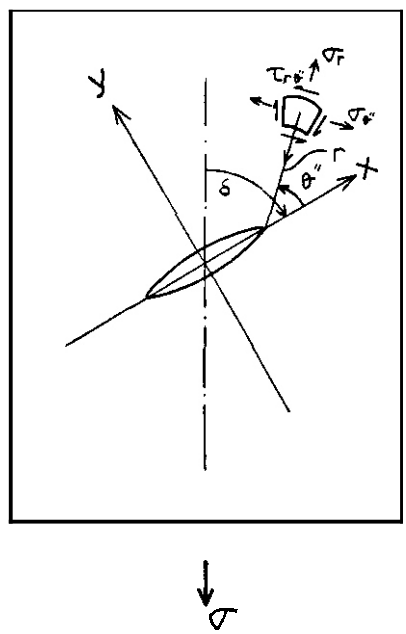

FIGURE 5: Stress Components Near the Crack Tip in Cylindrical Coordinates.

Mode I component:

$$I^{\tau}r\theta'' = \frac{2}{(2r)^{\frac{1}{2}}} k_1 \sin\theta'' \cos(\theta''/2) \qquad (1)$$

Mode II component:

$$II^{\tau}r\theta'' = \frac{2}{(2r)^{\frac{1}{2}}} k_2(3\cos\theta'' - 1)\cos(\theta''/2) \qquad (2)$$

where ${}_{I}\tau_{r\theta''} = {}_{I}\tau_{\theta''r}$ = shear stress in r direction on θ'' plane due to pure Mode I cracking, ${}_{II}\tau_{r\theta''} = {}_{II}\tau_{\theta''r}$ = shear stress in r direction on θ'' plane due to pure Mode II cracking, k_1 = stress intensity factor for Mode I, and k_2 = stress intensity factor for Mode II. The stress intensity factors for a combined Mode I and Mode II character, k_1 and k_2, are expressed as follows in Figure 6[9]:

$$k_1 = \sigma a^{\frac{1}{2}} \sin^2 \delta \qquad (3)$$

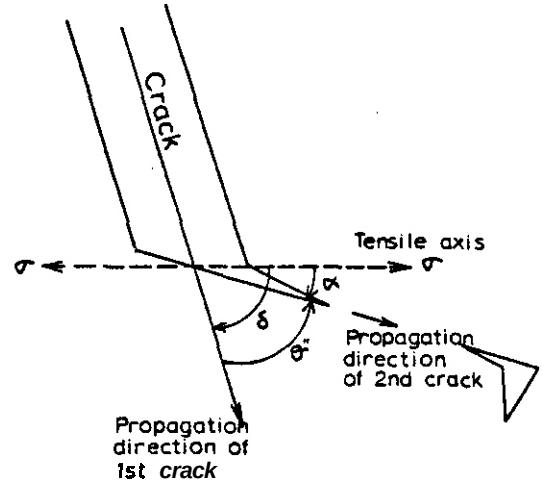

FIGURE 7: Schematic Drawing of Crack Propagation.

for different values of 6. The plotted graph for δ = 10°, 20°, 30°, 40°, and 50° is shown in Figure 8. Each curve is seen to have some relative maxima which shift their positions as 6 changes its value. If the value of e" which corresponds to the maximum point is taken to be $\theta"_{max}$, there is a possibility of the occurrences of shearing across a plane lying in the orientation of $\theta"_{max}$. Hence, to see the relation between the maximum shear stress and the angle of the crack propagation of the second crack against the tensile direction, the maximum value of τ_{max} is plotted against a in Figure 9. One can see that as α changes, the value of $\tau_{r\theta"}$ at the maximum point shifts smoothly. Also, it is seen that when α is close to 13°, 25°, 155°, and 167°, $\tau_{r\theta"}$ at its maximum point has a maximum value. From this result, it is theoretically estimated that when a = 13°, 25°, 155°, and 167°, the probability of the occurrence of grain boundary sliding is highest.

This theoretical result agrees with the experimental data which showed when $|\alpha| < 30"$ grain boundary sliding was observed.

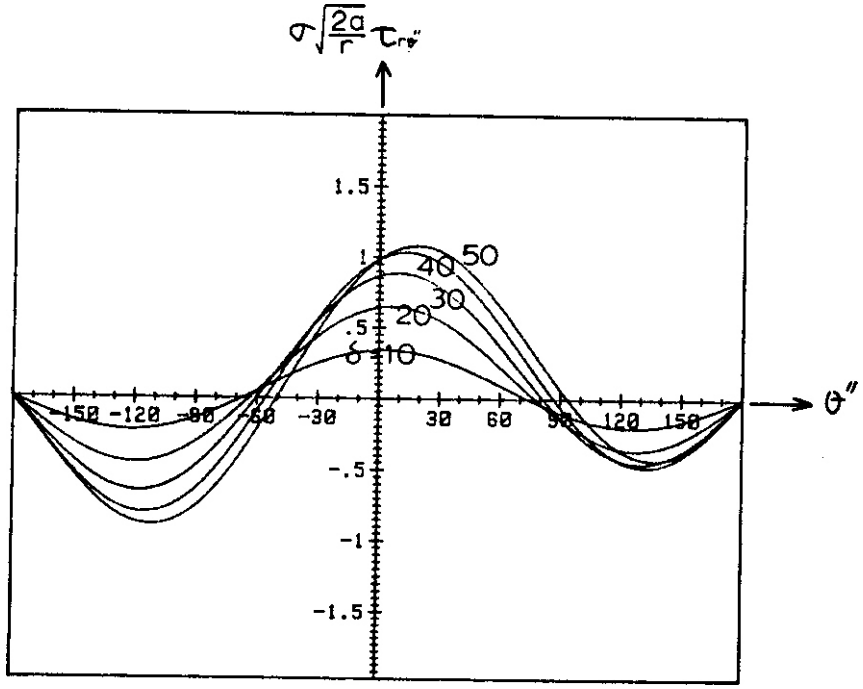

FIGURE 8: Relationship Between $\tau_{r\theta"}$ and e" for δ = 10°, 20°, 30°, 40°, and 50".

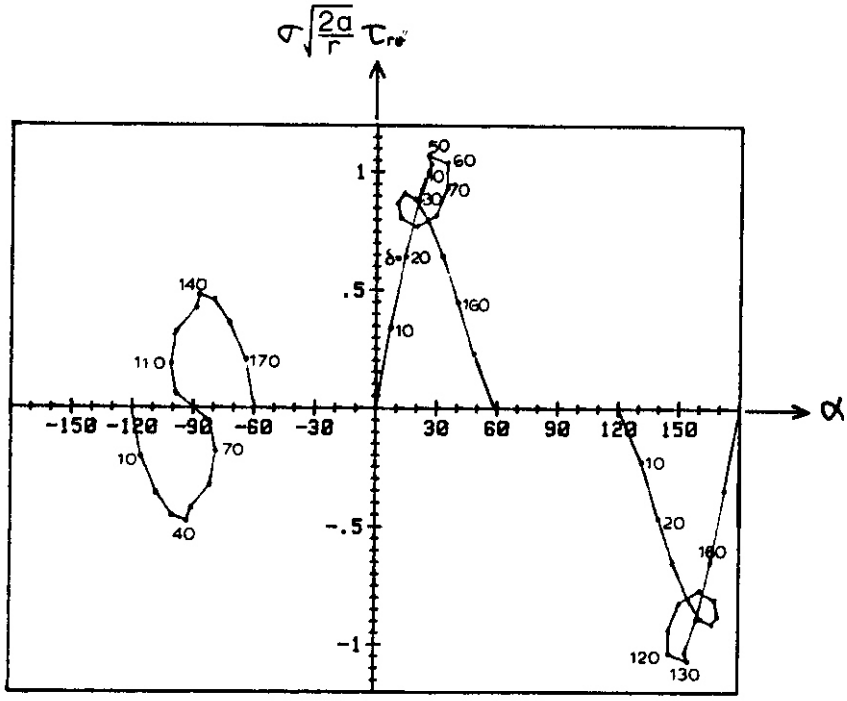

FIGURE 9: Relationship Between $(\tau_{r\theta"})_{max}$ and α for Various Values of 6.

5.5 Conclusions

All grain boundary sliding observed here was caused by a nearly Mode I crack reaching a grain boundary and initiating Mode II cracking at the grain boundary, i.e., initiating grain boundary sliding. Mode II cracking was only observed when the macroscopic tensile axis was nearly parallel to the grain boundary and also to the crack opening displacement vector.

Mode II failure is hindered and Mode I cracking is formed by neutron and helium irradiation. In the case of helium irradiation, Mode II cracking can be restored by post irradiation annealing.

Over the temperature range studied (25-600°C), Mode II intergranular failure in irradiated specimens was absent and Mode I intergranular failure was present in irradiated specimens.

In unirradiated specimens, the crack propagation mode was observed to undergo a transition from Mode II to Mode I when the crack direction angle *a* exceeded about 30°, and this result agrees with the theoretical result.

6.0 References

1. T. Hanamura and W. A. Jesser, "Effect of Helium Irradiation on Fracture Modes," DAFS Quarterly Report, DOE/ER-0046/11 (1982) 72.

2. J. I. Bennetch, R. D. Gerke and W. A. Jesser, "HVEM Observations *of* Crack Propagation in Helium Irradiated Type 316 Stainless Steel Containing Precipitates," DAFS Quarterly Report, DOE/ER-0046/2 (1930) 75.

3. D. S. Geller, L. E. Thomas and R. W. Powell, "HVEM In-situ Deformation of Neutron Irradiated Fe-0.3Cu," 109th AIME Meeting, Las Vegas, Nevada (1980).

4. R. D. Gerke. T. Hanamura and W. A. Jesser." Crack Propagation Characteristics in Helium Irradiated Type 316 Stainless Steel," DAFS Quarterly Report, DOE/ER-0046/6 (1981) 97.

5. J. A. Horton, "HVEM Studies of Helium Embrittlement," Ph.D. Dissertation, University of Virginia (January 1980).

6. J. I. Bennetch, "Microstructural Aspects of Helium Embrittlement in Stainless Steel," Ph.D. Dissertation, University of Virginia (May 1981).

7. R. 0. Gerke and W. A. Jesser, "Quantitative Load-Elongation Capabilities of an In-situ Hot Tensile Stage for HVEM Use," DAFS Quarterly Report, DOE/ER-0046/8 (1982) 71.

8. M. L. Williams, "On the Stress Distribution at the Base of a Stationary Crack," Journal of Applied Mechanics, Vol. 24, Trans. ASME, Vol. 79, 1957, pp. 109-114.

9. R. W. Hertzberg, Deformation and Fracture Mechanics of Engineering Materials, John Wiley and Sons, 1976, p. 263.

7.0 Future Work

Assessment of the amount of Mode III cracking will be made. The relation of microtensile specimen data and bulk specimen data is being addressed.

8.0 Publications

1. J. I. Bennetch and W. A. Jesser, "An Improved Reduced van der Waals Equation of State for Helium," J. Nucl. Mater., in press.

2. J. I. Bennetch and W. A. Jesser, "A TEM Method for Analysing Local Strain Fields in Irradiated Materials," J. Nucl. Mater., in press.

3. T. Hanamura and W. A. Jesser, "The Effect of Neutron and Helium Irradiation on the Crack Modes of Type 316 Stainless Steel," J. Nucl. Mater., in press.

4. R. D. Gerke and W. A. Jesser, "Crack Propagation Characteristics in Neutron Irradiated Type 316 Stainless Steel Microspecimens," J. Nucl. Mater., in press.

5. W. A. Jesser, "Dvnamic HVEM Observations of Metals and Alloys During In-situ Helium Ion "Irradiations," IEEE Transactions of Nucl. Sci., Vol. NS-30 No. 2, (1983) p. 1259.

CHARACTERIZATION OF LOCALIZED PLASTIC FLOW BY INDENTATION GEOMETRY ANALYSIS

M. Jayakumar and G. E. Lucas (Department of Chemical and Nuclear Engineering, University of California, Santa Barbara)

1.0 Objective

The purpose of this study was to investigate a means of characterizing localized plastic flow in irradiated metals with indentation hardness. Specifically, we have investigated techniques for characterizing the flow distribution around impressions produced by static indentation tests and to determine a relationship, if any, between this flow distribution and the degree of homogeneity in the plasticity of the test material.

2.0 Summary

Seven alloys, heat treatable to a range of strengths and ductilities, have been investigated. Specimens were fabricated and pulled in uniaxial tension as well as subjected to indentation hardness. Both tensile and hardness specimen surfaces were replicated and examined by transmission electron microscopy. In addition, hardness indentations were examined by multiple beam and differential interference techniques. It was observed that specimens exhibiting very coarse slip produced quite asymmetric pile-ups around the indentations, whereas specimens exhibiting fine slip produced indentations which were symmetric in their pile-up.

3.0 Program

Title: Damage Analysis and Fundamental Studies for Fusion Reactor Materials Development

Principal Investigators: G.R. Odette and G.E. Lucas

Affiliation: University of California, Santa Barbara

4.0 Relevant OAFS Program Plan Task/Subtask

Subtask B Fundamental Mechanical Properties

5.0 Accomplishments and Status

5.1 Introduction

For a variety of reasons, including volume limitations in high energy neutron sources, techniques are required for extracting mechanical properties from small volume specimens. To this end, a number of techniques have been under investigation at UCSB.[1-5]

One plastic flow phenomenon for which there is interest in characterizing in irradiated metals is the onset of inhomogeneous or localized plastic flow. This is generally attributed to dislocation channeling subsequent to or concurrent with an irradiation defect clearing or sweeping in widely spaced narrow channels coincident with slip planes.

A technique for characterizing localized plastic flow was identified as having potential by Lucas and Haggag.[3] In their investigation of the geometry of the pile-up around indentations in mild steel, they noted that the indentation lip exhibited peaks and valleys, i.e., it was "crown-like" in appearance. This had also been previously observed by Underwood,[6] who postulated that it was related to Liiders band formation in steels. Since Lüders deformation is one type of localized plastic flow, it was felt that localized or inhomogeneous plastic flow in general might lead to such a phenomenon; hence, indentation geometry analysis might be useful for monitoring and characterizing the onset of dislocation channeling in irradiated metals.

Consequently, a study was undertaken to investigate several techniques for indentation pile-up analysis and to determine a relationship, if any, be-

tween the pile-up geometry and the degree of homogeneity in the plastic flow of the test material.

5.2 Materials

Technique and correlation development was carried out on the six heat-treatable alloys listed in Table 1. These alloys were selected because of the range of strengths and ductilities to which they could be heat-treated and because of the low ductilities which could be achieved -- thereby simulating, to a certain extent, radiation effects. In addition, the alloys taken together exhibit a range of homogeneities in their plasticity. Final heat treatments and conditions are also given in Table 1.

Following development, techniques have been (and are being) tried on additional material. Reported here are results on nearly pure aluminum (1100 Al) in both the hot-rolled and the quenched and aged condition. This latter conditon was achieved by annealing specimens at 600°C for 1/2 h, quenching in liquid nitrogen and aging at room temperature for 15 h. This produces hardening by vacancy dislocation loop formation,[7] thereby simulating radiation-induced dislocation channeling during plastic deformation.

5.3 Experimental Procedure

Tensile specimens -- 3.2 mm in diameter, 50.8 mm long and with a 25.4 mm gage length -- were fabricated from the various conditions of the first six alloys given in Table 1. Three specimens of each material were pulled in uniaxial tension at room temperature; and stress-strain curves, strength, and ductility data were obtained. Selected tensile specimen gage section surfaces were electropolished and then replicated before and after tensile testing. Replicas were examined on a JEM-200 CX to determine the nature of deformation in uniaxial tension.

Following tensile testing, the specimen end tabs were sectioned off, mounted

TABLE 1

Description of Test Alloys

ALLOY	HEAT TREATMENT		
	Soft	Intermediate	Hard
Cu-2 *Be*	Anneal at 800°C, 1/2 h; water quench	As received	Anneal at 800°C, 1/2 h; age 1 h at 330°C
7075 Al	Anneal at 470°C, 2 h; water quench	Anneal at 470°C, 2 h; water quench; age 1 day at Rm. Temp.	Anneal at 470°C, 2 h; water quench; age 1 day at 120°C
4340 Steel	Anneal at 845°C, 1 h; oil quench; age 1 h at 5400C		Anneal at 845°C, 1 h; oil quench; age 1 h at 260°C
A6 Steel	Anneal at 730°C, 1/2 h; furnace cool to 630°C and water quench	Anneal at 870°C, 1 h; water quench; age 1 h at 595°C	Anneal at 870°C, 1 h; water quench; age 1 h at 1200c
17-4 PH	Anneal at 1040°C, 1 h; water quench; age 6 h at 6500C	Anneal at 1040°C, 1 h; water quench, age 2 h at 540°C	Anneal at 1040°C, 1 h; water quench; age 1 h at 480°C
Ti-Cr-Al	Anneal at 785°C, 20 min; air cool		Anneal at 785°C, 20 min: water quench; age 72 h at 480°C; water quench
1100 Al	As-received		Anneal at 600°C, 1/2 h; liquid nitro-gen quench; Age at rm. temp., 15 h.

in Bakelite, polished and subjected to 120° cone indentations. Loads were adjusted to provide indentations with diameters of ~ 0.11 to 0.15 mm, a size convenient for subsequent investigation by optical microscopy. Selected indentations were replicated, and the replicas examined by transmission electron microscopy. All indentations were examined by both multiple beam interferometry and differential interferometry. Multiple beam interferometry was conducted on a Unitron Series N Metallograph using a xenon source and cadmium filter to produce monochromatic light with a 644 nm wavelength. Differential interfeometry was conducted on a Leitz Laborlux microscope using a tungsten source and a polarizer. Micrographs of indentations and replicas were then used in conjunction with tensile data to determine a relationship between flow distribution and indentation geometry.

5.4 Results and Discussion

Results of the tensile tests are summarized in Table 2. As can be seen, materials exhibited total ductilities ranging from ~ 4 to 40% and yield stresses ranging from 143 to 1800 MPa. In addition it should be noted that the Cu-2Be, 7075 Al and Ti-Cr-Al all showed evidence of localized plastic flow phenomena in the tensile tests. The Cu-2Be and 7075 Al exhibited serrated yielding, characteristic of dynamic strain aging, and the Ti-Cr-Al alloy in the soft condition showed nearly elastic-perfectly plastic behavior.

Analysis of indentation geometries and surface replicas revealed the following. For materials which exhibited fine slip in uniaxial tensile deformation (i.e., the A6, 17-4 PH and 4340 steel specimens), fine slip was also exhibited in the indentation pile-up; and the pile-up itself showed a high degree of uniformity with little or no crowning (i.e., exhibition of a crown-like lip). A representative example is shown in Fig. 1. The differential interference micrograph shows that slip is relatively fine, and the multiple beam interferograph shows that the pile-up is quite uniform; i.e., the fringes are concentric with no nested circles, (which are indicative of crowning) at the lip of the indentation.

TABLE 2

Summary of Uniaxial Tensile Test Results

Alloy	Yield Stress (MPa)	Ultimate Tensile (MPa)	Uniform Elongation (%)	Total Ductility (%)	Reduction in area (%)	Strain Hardening Exponent
Cu-2 Be						
Hard	1014	1225	6.2	7.2	11.8	0.117
Medium	613	744	4.9	17.7	65.2	0.126
Soft	212	491	36.1	37.5	71.4	0.242
7075 Al						
Hard	515	580	9.7	17.4	31.2	0.066
Medium	258	459	17.4	20.6	34.3	0.017
Soft	143	356	16.3	20.7	40.0	0.244
4340 Steel						
Hard	1544	1898	3.7	12.7	49.8	0.138
Soft	697	834	9.2	20.4	66.1	0.068
A6 Steel						
Hard	1800	2331	4.4	4.4	6.9	0.133
Medium	1320	1471	4.8	7.9	22.7	- -
Soft	477	837	10.0	12.8	23.6	0.198
17-4 PH						
Hard	1245	1411	4.1	15.1	56.3	0.102
Medium	1060	1163	4.4	16.4	61.4	0.113
Soft	706	971	4.3	17.7	63.8	0.187
Ti-Cr-Al						
Hard	1309	1421	5.2	6.1	11.1	0.054
Soft	990	990	14.4	23.6	57.9	0.020

On the other hand, materials which exhibited localized flow in their tensile behavior exhibited coarse slip steps on the gage surface. An example for Cu-2 Be is shown in Fig. 2. In addition, coarse slip was also evident in the pile-up around the indentations in these alloys, and the pile-ups exhibited a pronounced crown-like appearance. An example for Cu-2 Be is shown in Fig. 3. The differential interference micrograph demonstrates the coarseness of slip around the indentation, and the multiple beam interferograph shows large groups of nested fringes around the indentation lip.

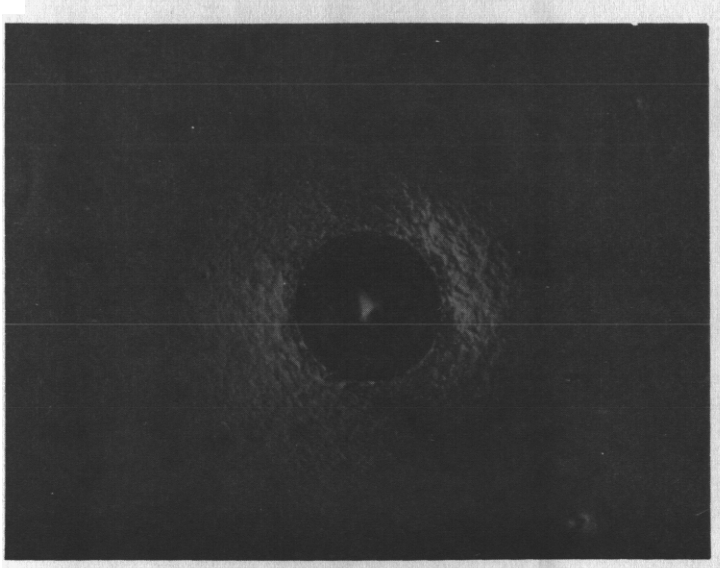

(a)

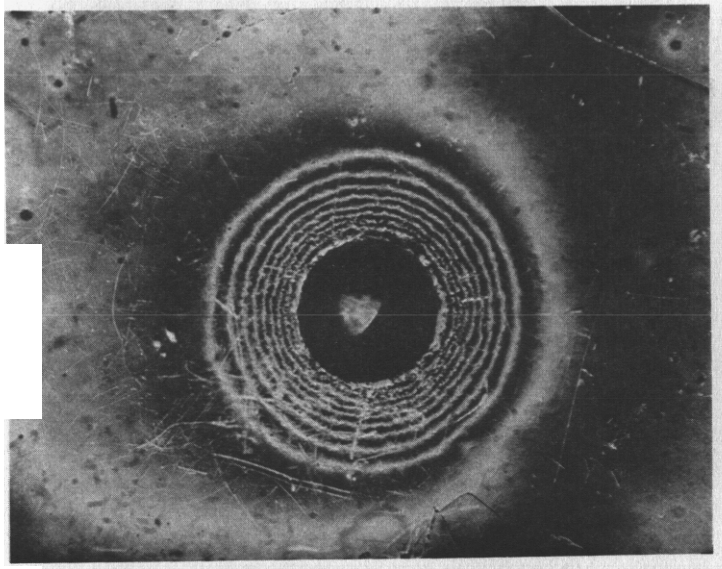

(b)

FIGURE 1. Differential Interference Micrograph (a) and Multiple Beam Interferograph (b) of D6 Tool Steel in the Soft Condition.

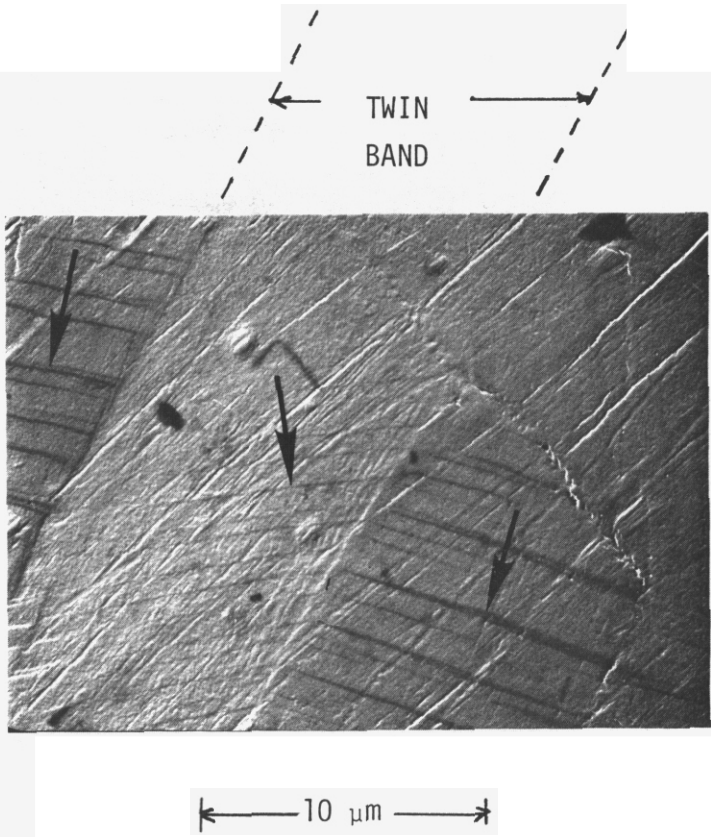

FIGURE 2. Transmission Electron Micrograph of a Surface Replica of the Soft Cu-2 Be Tensile Specimen at 8.1% Strain. Lines Correspond to Slip Steps.

In all the alloys investigated, this correspondence between coarse slip and crowning around the indentation lip was observed. Moreover, for a given alloy, the slip was observed to either be coarse for all heat treatments or fine; that is, there was no transition from fine slip to coarse slip as the alloy became harder as one might expect, for instance, in an irradiated metal.

Consequently, we attempted to simulate an irradiation response in 1100 aluminum by quenching and aging as described previously in Section 5.2. Both the hot-rolled and quenched/aged sample were investigated by interference microscopy of indentation geometries. Results of the interferometry

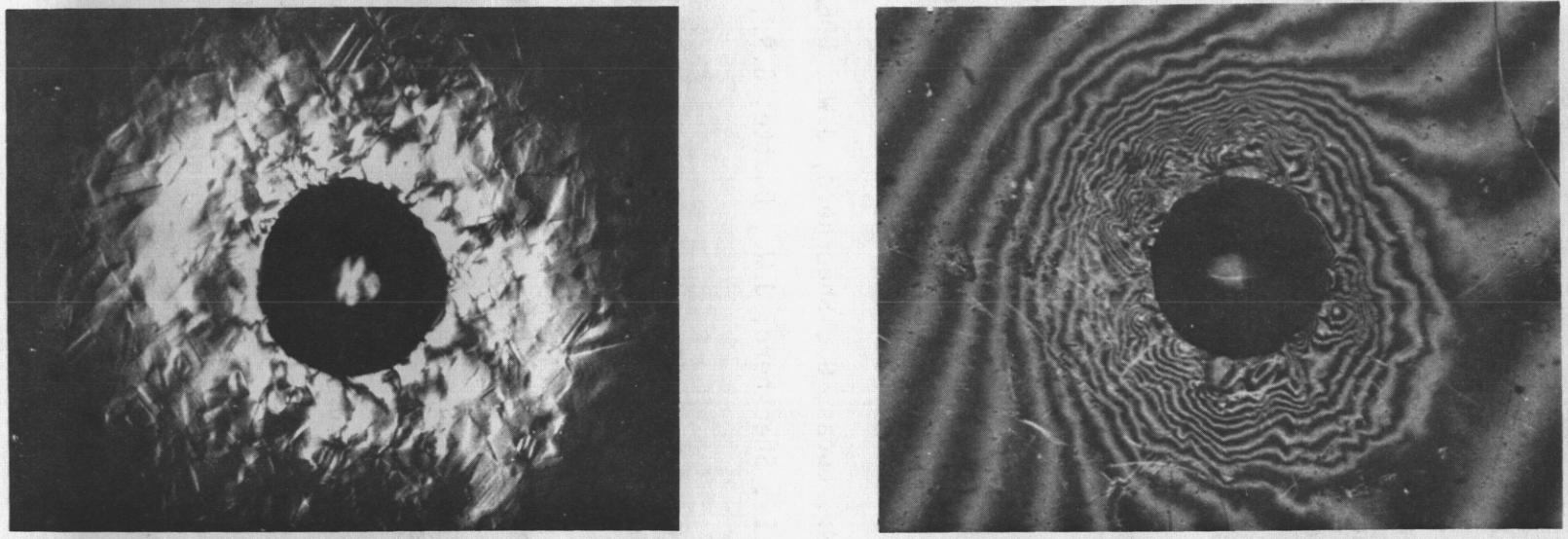

(a) (b)

FIGURE 3. Differential Interference Micrograph (a) and Multiple Beam Interferograph (b) of Cu-2 Be in the Soft Condition

analysis are shown in Fig. 4. The hot-rolled sample exhibited fine-to-intermediate slip, and as can be seen in Fig. 4, the pile up is largely devoid of crowning (the lip is somewhat obscured by deformation that took place when the reference plane of the interference objective contacted the surface). The quenched and aged sample showed coarse slip, and as can be seen in Fig. 4, pronounced crowning was exhibited in multiple beam interferography. Thus, the technique appears promising for application to irradiated materials.

6.0 References

1. Lucas, G.E., et al., DOE/ET-0065/5 (1979) 199.

2. Lucas, G.E., et al., DOE/ER-0046/4 (1981) 46.

3. Lucas, G.E., Haggag, F., DOE/ER-0046/6 (1981) 105.

4. Oooley, M., Lucas, G., Sheckherd, J.W., DOE/ER-0046/8 (1982) 104.

5. Lucas, G.E., Sheckherd, J.W., Odette, G.R., DOE/ER-0046/11 (1982) 43.

6. Underwood, J.H., "Residual Stress Measurement Using Surface Displacements Around an Indentation, "Proc. Soc. Exp. Stress Analysis, 30, 2 (1973) 1.

7. I. Crivelli-Visconti and I.G. Greenfield, J. Appl. Phys., 39, 6 (1969) 2845.

7.0 Future Work

Work is underway to quantify the results described above. In addition other materials, particularly copper, are being investigated in quench and age experiments similar to the one conducted on aluminum as described above. Following favorable evaluation, the technique may be applied to other alloy systems and to actual irradiated samples.

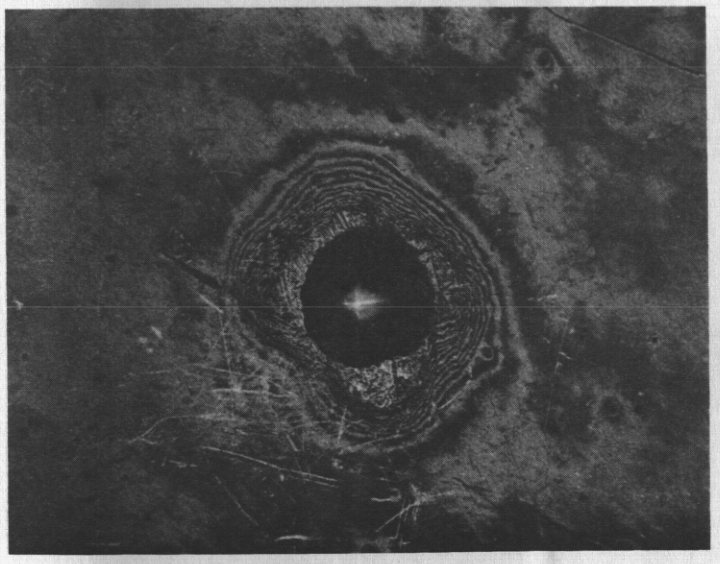

(a)

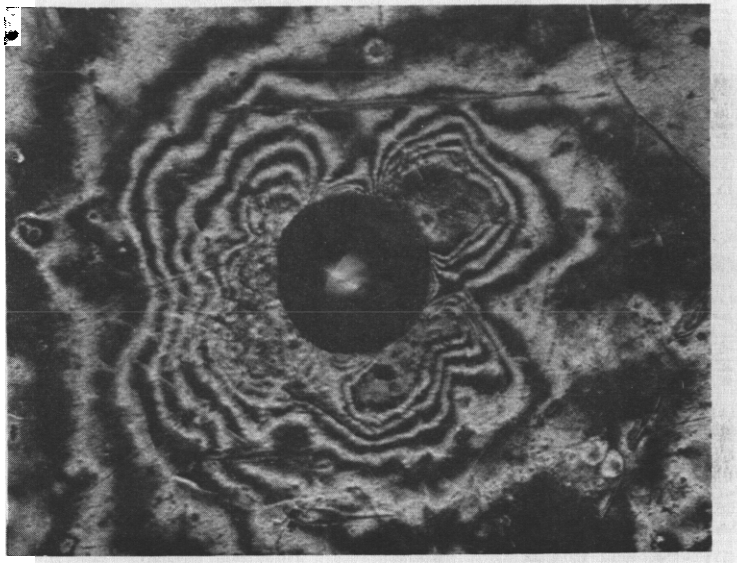

(b)

FIGURE 4. Comparison of Multiple Beam Interferographs on 7100 Aluminum in the (a) Hot-Rolled and (b) Quenced and Aged Condition.

FUNDAMENTAL FLOW AND FRACTURE ANALYSIS OF PRIME CANDIDATE ALLOY (PCA) FOR PATH A (AUSTENITICS)

G.E. Lucas, P. Brashear (Department of Chemical and Nuclear Engineering, University of California, Santa Barbara)
P. J. Maziasz (Metals and Ceramics Division, Oak Ridge National Laboratory)

1.0 Objective

The purpose of this aspect of the program is to use a set of well-characterized alloys under investigation in the Alloy Development for Irradiation Performance (ADIP) program to develop an understanding of the relationship between microstructure and fundamental flow and fracture behavior. Such an understanding is vital to the development of correlation methodologies for use in the fusion materials program. Moreover, the mechanical properties data obtained in such an analysis will be of immediate interest to the ADIP program.

2.0 Summary

Work has proceeded in two different areas. In the first, shear punch tests were performed on several microstructures of PCA and values of room temperature yield stess, ultimate tensile strength, and reduction in area were predicted. This was done as a blind test, with actual experimental values of the corresponding parameters determined separately at ORNL. Quite good agreement was obtained between predicted and actual values of the strength parameters. In the second area, techniques have been developed to test miniaturized tensile specimens under creep and creep rupture conditions; a creep test program has been initiated on the A3 and B2 microstructures of PCA, and preliminary results, compared to MFE 316 stainless steel, are reported here.

3.0 Program

Title: Damage Analysis and Fundamental Studies for Fusion Reactor Materials Development

Principal Investigator: G. R. Odette and G. E. Lucas

Affiliation: University of California, Santa Barbara

(This work was performed in collaboration with P. J. Maziasz, Alloy Development for Irradiation Performance (ADIP) Program for Magnetic fusion Energy, Metals and Ceramics Division, Oak Ridge National Laboratory.)

4.0 Relevant DAFS Program Plan Task/Subtask

Subtask B Fundamental Mechanical Properties

Subtask C Correlation Methodology

5.0 Accomplishments and Status

5.1 Introduction

As described previously,[**]) this program was initiated for several reasons. A number of microstructures of PCA have been fabricated and well characterized for purposes of studying the void swelling response of this system; hence, a materials bank exists which is ideally suited for fundamental flow and fracture investigations. Moreover, a need exists to evaluate the mechanical properties of this alloy system to complement the swelling resistance data which are currently being collected.

Initial microhardness studies[**]) showed that PCA precipitate-hardened with aging time at 750°C, whereas cold-worked, solution strengthened austenic stainless steels softened under the same conditions. This provided some demonstration that PCA in the precipitate hardened condition might exhibit a better elevated temperature strength than solution strengthened and/or cold-

work strengthened austenitic stainless steels. As a subsequent effort, shear punch tests were performed on PCA to corroborate the microhardness findings. (This was also done, to some extent, to test the shear punch approach, as part of the effort to develop small specimen test techniques.[2]) In addition creep and creep rupture investigations were initiated on several microstructures of PCA and on MFE 316 stainless steel in the 20% cold worked condition as a reference. The results of these efforts are reported below.

5.2 Shear Punch Tests

Shear punch tests were conducted on PCA microstructures A1, A2, A3, B2, C, and D at room temperature using both 3 mm and 1 mm punches. From the resulting load-displacement curves, the yield stress, ultimate tensile strength (UTS) and reduction in area were determined by procedures discussed elsewhere.[3] At this time, because of the limited data upon which these correlations are based, the uncertainty in strength predictions is ± 150 MPa; and the uncertainty in reduction in area (RA) predictions is ± 20% of the RA value. For comparison, shear punch tests were also conducted on the M1, M3, and M4 microstructures of MFE 316 stainless steel and the 01, 03, and 04 microstructures of the DO heat of 316 stainless steel.* These data were obtained without prior knowledge of the actual room temperature tensile data of the corresponding alloys. Hence, the experiment was performed as a blind test.

Following these tests, data were compared to tensile data obtained on alloys 01, 03,[4] A1, A3, B2[5] and M3.[6] Results of the comparison are shown in Table 1 and Fig. 1. Several points are worth noting. First, given the uncertainty in the shear punch-UT5 prediction and the uncertainty in the empirical correlation between diamond pyramid hardness and UTS,[7] there is

*The numbers in the designations M1-M4 and 01-04 have the following meanings:
1 = solution annealed
3 = 20% cold worked
4 = 20% cold worked plus aged 2 h @ 750°C

Table 1

Comparison of Strength and Ductilities Predicted from Shear Punch and Microhardness Tests with Uniaxial Tensile Test Data

Alloy Designation	Yield Stress, σ_y (MPa)		Ultimate Tensile Strength, σ_{UTS} (MPa)			Reduction in Area RA	
	Predicted 3mm (1mm)	Measured	Predicted 3mm (1mm)	[from DPH]	Measured	Predicted 3 mm (1mm)	Measured
M3	645	688	920	[958]	791	0.63	0.434
O1	300	240	710	[531]	650	0.60	
O3	550	813	790	[1006]	848	0.57	
A1	130	220	450	[460]	529	0.45	0.451
A3	500 (580)	603	730 (740)	[740]	737	0.56 (0.47)	0.283
B2C	530 (650) 510 (600)	442	790 (870) 725 (775)	[807] [772]	723	0.60 (0.42) 0.61 (0.52)	0.373

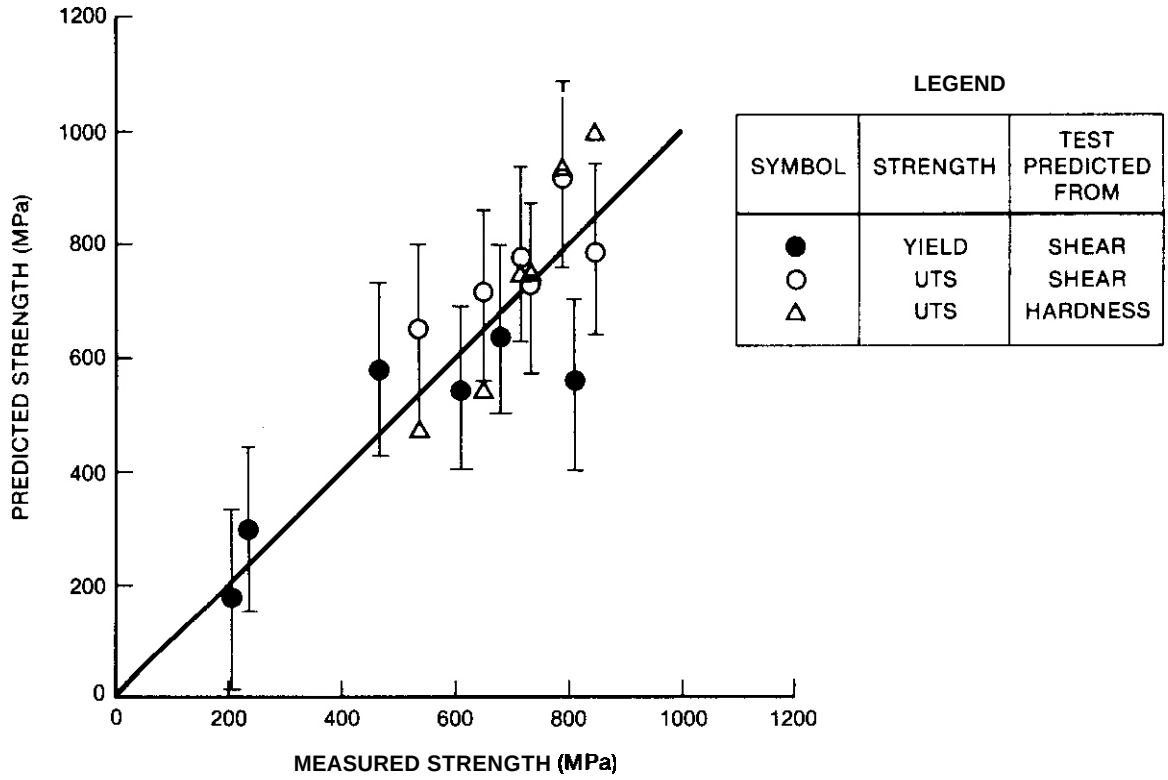

FIGURE 1. Comparison of Values of Yield Stress and Ultimate Tensile Strength Measured in Uniaxial Tension Tests with Values Predicted from Both Shear Punch and Diamond Pyramid Hardness Tests.

reasonable agreement among both predicted values and the actual measured values of UTS. Secondly, with the exception of one material (03), there is reasonable agreement between the predicted and measured values of yield stress. Finally, the values of UTS predicted from shear data are in better agreement than the values of yield stress; this is a reflection *of* the better experimental accuracy in determining maximum loads in the shear-punch load-displacement curves than in determing yield loads.[3]

It should also be noted that the material exhibiting the highest room temperature yield stress (813 MPa), and the highest room temperature UTS (848 MPa) is 03. The microstructure/alloy exhibiting the lowest room temperature yield stress (220 MPa) and the lowest ultimate tensile strength (529 MPa) is Al.

Finally, the predicted values of reduction in area are in rather poor agreement with measured values. This may in part be due to difference in tensile specimen geometries (i.e., the ones used to generate the punch correlation versus the ones used to obtain the data in Table 1). This is currently under investigation.

5.3 Creep and Creep Rupture Tests

Creep and creep rupture properties of alloys selected from those mentioned above are being conducted on sheet tensile specimens with the nominal geometry given in Fig. 2. These specimens are relatively small. This geometry was selected to maximize the number of specimens which could be tested from the available experimental alloy stock.

Prior to initiating tests on PCA microstructures and reference materials, an initial developmental effort was undertaken to devise a means of testing these small specimens to obtain both creep and creep rupture data, and to validate these data against larger specimens. ATS 2430 creep frames were modified to provide both lever arm and direct dead weight loading. Special wedge grips were fabricated to permit aligned gripping of the small specimens and to provide standard mechanical/electrical extensometers (ATS 412 type) to be attached for displacement measurement. The grip geometry is shown in Fig. 3. Because of the specimen size, it was decided to avoid attaching an extensometer directly to the specimen gage section. However, to minimize extraneous displacment measurements, the points of attachment were kept as close to the specimen gage section as possible. As shown in Fig. 3, the extensometer attaches to the rib just behind the specimen end tab.

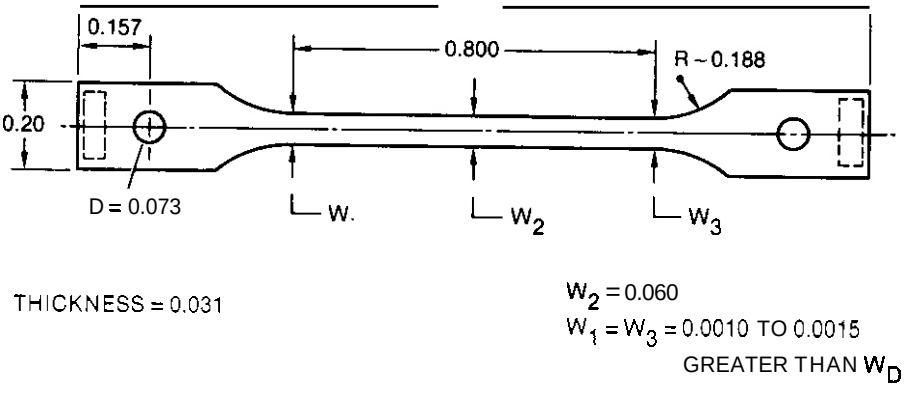

FIGURE 2. Geometry of Sheet Tensile Specimen. (Dimensions are in inches.)

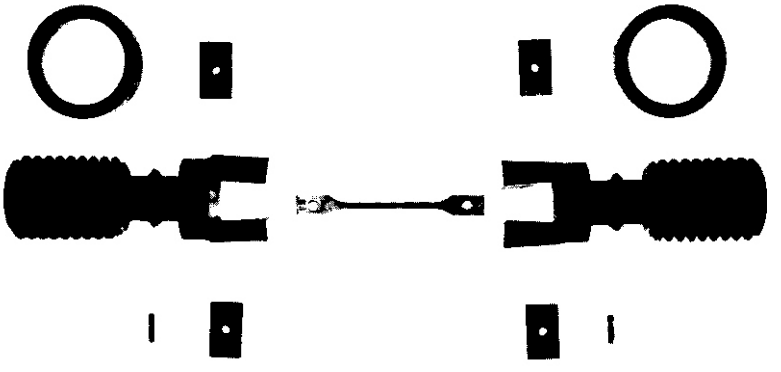

FIGURE 3. Small Creep Specimen Grips.

To validate the small specimen test technique, both small specimens (i.e., Fig. 2) and large (i.e., a gage section 5.08 cm long x .64cm x .084 cm) specimens -- to which the extensometer could be directly attached -- were cut from AISI 302 stainless steel. Both types of specimens were tested in uniaxial tension over a temperature range of 755-1030°K and a stress range of 124-558 MPa. Results are shown in Figs. 4 and 5.

Figure 4 illustrates the variation of the Larson-Miller parameter (LMP) with applied stress σ for both large and small specimens, here

$$LMP = T(^{o}K)(\log t_r(h) + 20) \qquad (1)$$

where t_r is the rupture time and T is the test temperature.

As can be seen, the data obtained from both large and small specimens fall on the same master curve, indicating the validity of the small specimen technique for obtaining creep rupture data. Note the two separate regimes of σ vs. LMP. These both correspond to regimes of transgranular fracture as can be verified by the corresponding factographs shown in Fig. 4. Preliminary analyses indicate that the behavior at high stresses probably corresponds to a dislocation glide controlled regime, and the behavior at low stresses to a dislocation climb-glide regime.

Figure 5 illustrates the variation of the rupture time with the minimum creep rate, i.e., the Monkman-Grant relationship,[8] for both large and small specimens. Again both data sets fall on the same master curve, indicating the validity of the small specimen test technique for measuring both creep strain and creep rates.

Once the techniques had been developed and verified, tests were begun on PCA microstructures A3 and B2 and on M3 as a reference material (i.e,, MFE 316 stainless steel, 20% cold-worked). To date, tests have only been conducted at 650°C in the stress range 262-379 MPa. Comparisons of the data for the three alloys/microstructures are shown in Figs. 6 and 7.

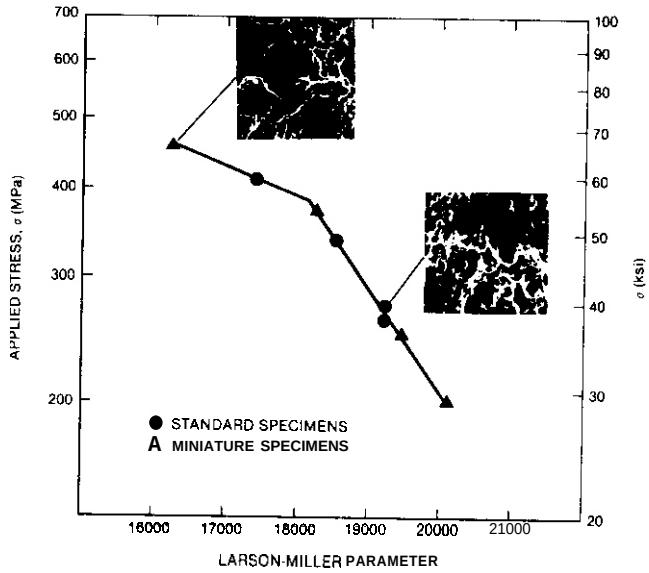

FIGURE 4. Variation of the Larson-Miller Parameter with Applied Stress for Both Large and Small Tensile Specimens.

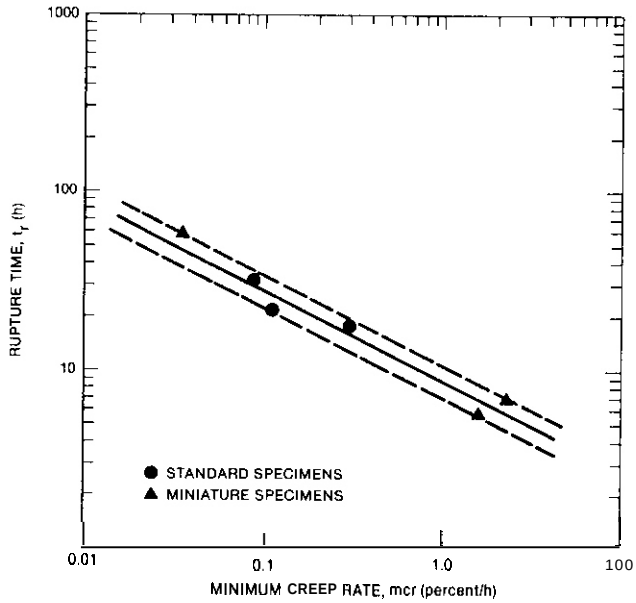

FIGURE 5. Variation of the Minimum Creep Rate with Rupture Time for Both Large and Small Tensile Specimens.

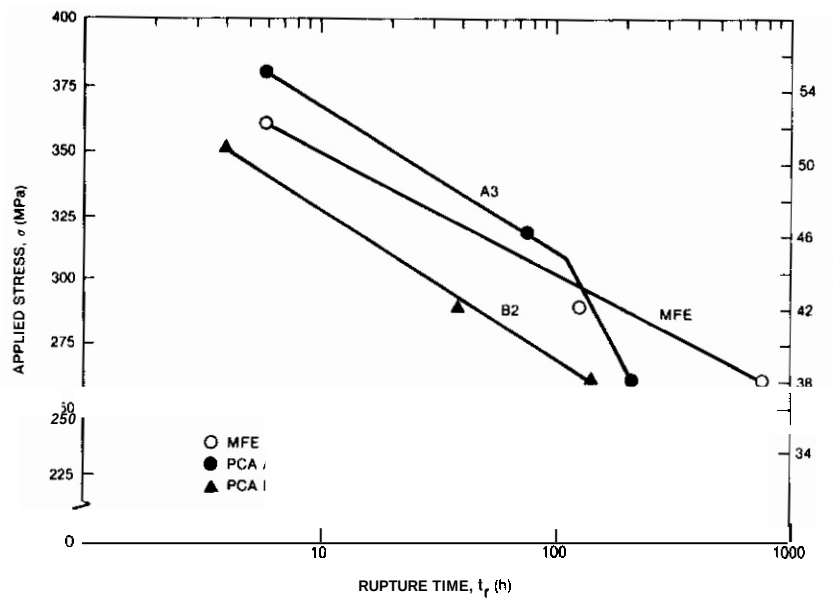

FIGURE 6. Variation of the Rupture Time with Applied Stress for M3, A3, and 82 at 650°C.

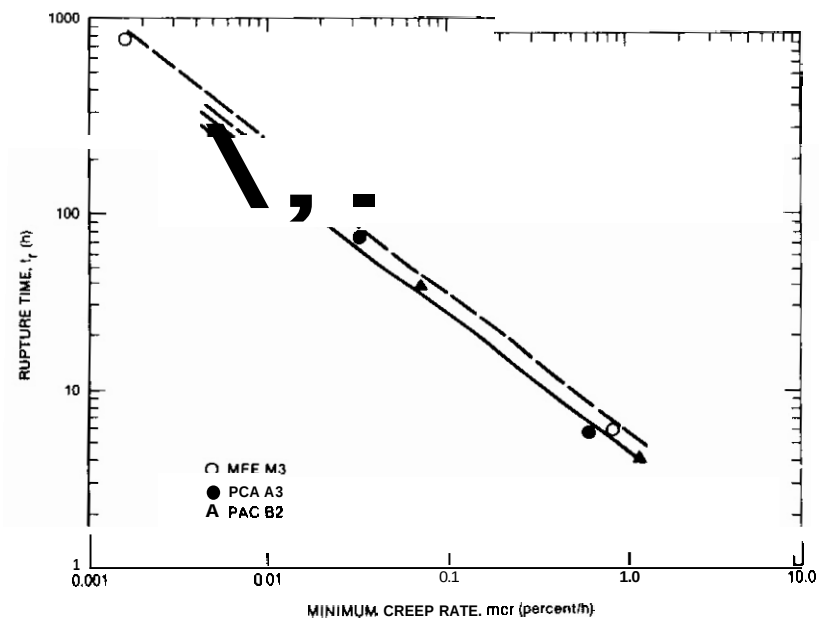

FIGURE 7. Variation of the Minimum Creep Rate with Rupture Time for M3, A3, and 82 at 650°C.

Figure 6 illustrates the variation of rupture time with applied stress. For these conditions, all failures were transgranular with the exception of the test at 262 MPa for A3. This failure was intergranular (as verified by fractography) and corresponds to a slope change in σ vs. t_r. In the transgranular failure regime, for a given rupture time, the applied stress is greatest for A3 and smallest for 82. This is consistent with the elevated temperature yield stress data for these alloys/microstructures.(5)

Figure 7 illustrates the variation of the minimum creep rate with rupture time for the three materials. For a given rupture time, the creep rate is somewhat higher for M3. The creep rates for 82 and A3 are nearly identical.

It is important to note that at these test temperatures and times, the microstructures of these materials are not constant. For instance, time-temperature-precipitation (TTP) curves for PCA show that the percent formation of MC achieved by aging at 750°C for 2 h (i.e., the matrix precipitation step in microstructure B2) is also achieved at 650°C in ~ 42 h.(9) This is born out in the tests to date. For instance, Fig. 8 shows both bright field and dark field TEM micrographs of alloy A3 after exposure to 650°C for 217 h (i.e., the TEM disc was cut from the gage section of the corresponding creep rupture specimen after the test). The decoration with MC of the dislocations is quite similar to but slightly coarser than that for microstructure B2.(1) (Note that both the matrix and grain boundary MC distirbutions are similar to, but again slightly coarser than, microstructure C(9)). Consequently, it is not entirely surprising that the creep results are similar for A3 and 82 at long test times. However, since the 82 has significantly coarser MC at the grain boundary (see ref. 1) than the tested A3, the response to intergranular failure may be considerably different. This will be investigated in future tests. Similarly, TEM investigations of the other microstructures and test conditions are ongoing. However, there is insufficient data at this point in time to draw any conclusions.

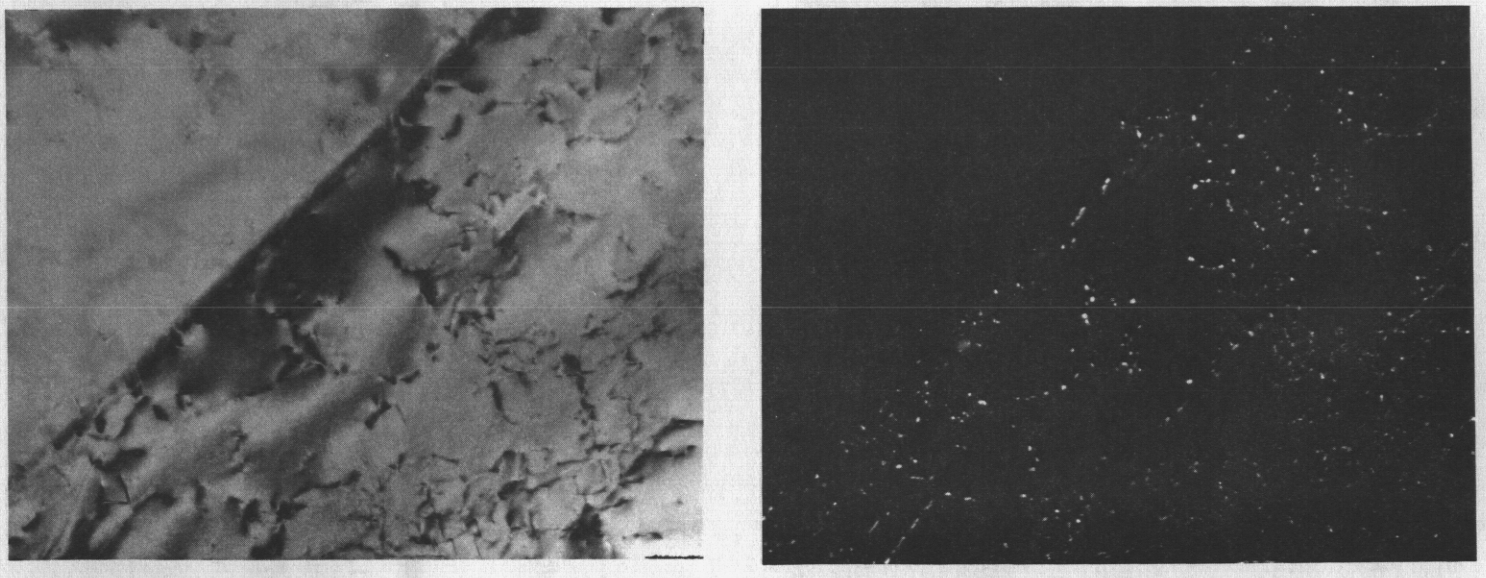

FIGURE 8. Comparison of the a) Bright Field (BF) and b) Dark Field (DF) TEM Micrographs of A3 after testing at 650°C for 217 h. The dark precipitates in BF (bright spots in DF) correspond to MC.

6.0 References

1. G. E. Lucas, M. Jayakumar, and P. J. Maziasz, DAFS Quart. Prog. Rep., DOE/ER-0046/11 (1982) 54.

2. G. E. Lucas, J. W. Sheckherd, and G. R. Odette, DAFS Quart. Prog. Rep., DOE/ER-0046/11 (1982) 43.

3. G. E. Lucas, "The Development of Small Specimen Mechanical Test Techniques", presented at the TMS-AIME Meeting, St. Louis, 1982, to be published in J. Nucl. Mater.

4. F. W. Wiffen and P. J. Maziasz, J. Nucl. Mater., 103 and 104 (1981) 821.

5. D. N. Braski and P. J. Maziasz, DOE/ER-0045/9 (1982) 69.

6. D. N. Braski and P. J. Maxiasz (to be published in DOE/ER-0045/10).

7. Metals Handbook, 8th Ed., Volume I, ASM, Metals Park, Ohio (1961) 1234.

8. F.C. Monkman and N.J. Grant, "An Empirical Relation Between Rupture Life and Minimum Creep Rupture Tests", ASTM Proceedings, Vol. 56, Phil. PA (1956).

9. P. J. Maziasz and T. K. Roche, ADIP Quart. Prog. Rep., DOE/ET-0058/7 (1979) 83.

7.0 Future Work

Work will continue on obtaining creep and creep rupture data on materials M3, A3, and 82, particularly at lower temperatures. Additional microstructures may be investigated. Furthermore, microstructural analysis of specimens will continue. Microstructures of the as-fabricated material will be compared to material exposed to time at temperature (specimen end tabs) and creep deformation (gage length). Work will begin on microstructure-property relationship and deformation/fracture mapping.

C H A P T E R 5

CORRELATION METHODOLOGY

SUPPRESSION OF VOID NUCLEATION BY INJECTED INTERSTITIALS FOR MEDIUM ENERGY IONS

D.L. Plumton, H.M. Attaya and W.G. Wolfer (University of Wisconsin)

1.0 Objective

Injected interstitials were recently shown to suppress void nucleation in 14 MeV ion bombardment. For 5 MeV ion bombardment, which is employed by many laboratories, the spread of the injected interstitials represents a larger fraction of the entire range. The effect of this increased overlap of the two profiles, displacement damage and injected interstitial, on the suppression of void nucleation is investigated.

2.0 Summary

The effect of injected interstitials on void nucleation depends on the precise distribution of both the displacement damage and the deposited ions. The lower the ion energy, the larger the overlap of these two distributions. These distributions have been obtained for 5 MeV Ni ion bombardment of nickel using two different computer codes. The BRICE and HERAD codes were used to evaluate the depth distribution of the void nucleation rate. Significant differences were found for the degree and range of void nucleation suppression.

3.0 Programs

Title: Effects of Radiation and High Heat Flux on the Performance of First Wall Components
Principal Investigator: W.G. Wolfer
Affiliation: University of Wisconsin-Madison
Title: Radiation Damage Studies
Principal Investigator: G.L. Kulcinski and R.A. Dodd
Affiliation: University of Wisconsin-Madison

4.0 Relevant DAFS Program Task/Subtask

II.B.2.3
Subtask C. Correlation Methodology

5.0 Accomplishment and Status

5.1 Introduction

In a recent investigation, Plumton and Wolfer[1] have shown that the injected self-ions in ion-bombardment studies can suppress void nucleation in the peak damage region. This suppression was particularly pronounced at low temperatures when recombination becomes the dominant point defect loss mechanism. Since the predominance of recombination also depends on the displacement rate, which in turn is a function of depth, the depth distribution of the void nucleation rate exhibits a complicated profile. The void nucleation profile is determined by the mutual overlap of the two depth distribution profiles, the displacement rate profile and the ion deposition rate profile. For example, it was found that voids nucleate in two separate bands, one found in front and one behind the peak damage region. Although a large fraction of the self-ions come to rest behind the peak damage region, void nucleation is still possible inspite of the high concentration of excess interstitials because the displacement rate is low. The low displacement rate gives a low point defect supersaturation so that point defect loss occurs mainly at sinks and recombination is insignificant as a loss mechanism; therefore the injected interstitials have little effect on void nucleation.

The previous investigation was specifically carried out for 14 MeV Ni ion bombardment of nickel and utilized the BRICE code to determine profiles for the displacement damage and ion deposition. Because of the large ion range, the region of mutual overlap of these profiles is relatively small and not very sensitive to the precise determination of these profiles. However, for lower energy bombardment the overlap region becomes an increasing fraction of

the total ion range. Consequently, any inaccuracies in the damage and ion deposition profiles for low energy ions will likely have a larger effect on the accuracy of the nucleation profile. For example, it is assumed in the BRICE code that the ion deposition profile is Gaussian. While this is probably a reasonable assumption for high energies, it is expected to be less reliable at lower ion energies.

The calculations were carried out for 5 MeV Ni ion bombardment of nickel using the results of both the BRICE[2] and the HERAD[3] code. The latter code solves the ion transport problem without resorting to any compromising assumptions by the implementation of a Monte Carlo simulation. With a sufficiently large number of case histories, accurate damage and ion deposition profiles can be obtained.

5.2 Displacement Damage and Ion Deposition Profiles

The displacement damage profiles calculated with the BRICE and HERAD codes are illustrated in Figs. 1 and 2, respectively, where the minimum displacement energy is taken as 40 eV. The damage peak for the BRICE case is at ~ 0.85 μ while for the HERAD case the peak is at ~ 1.05 μ. This shift of the HERAD peak, relative to the BRICE peak, towards the end of range is reflected in the ion deposition profiles. The BRICE peak deposition is at ~ 1 μ while the HERAD peak deposition is at ~ 1.2 μ.

The displacement rate and the excess interstitial fraction are plotted as a function of depth for both codes in Fig. 3. The excess interstitial fraction in both 5 MeV cases rises to about three times the magnitude of that in the 14 MeV case. Therefore the excess interstitials should be more important for 5 MeV irradiations than the 14 MeV irradiations.

5.3 Void Nucleation Profiles

For the evaluation of the void nucleation rates as a function of depth in nickel the same materials parameters were used as in the previous study.[1]

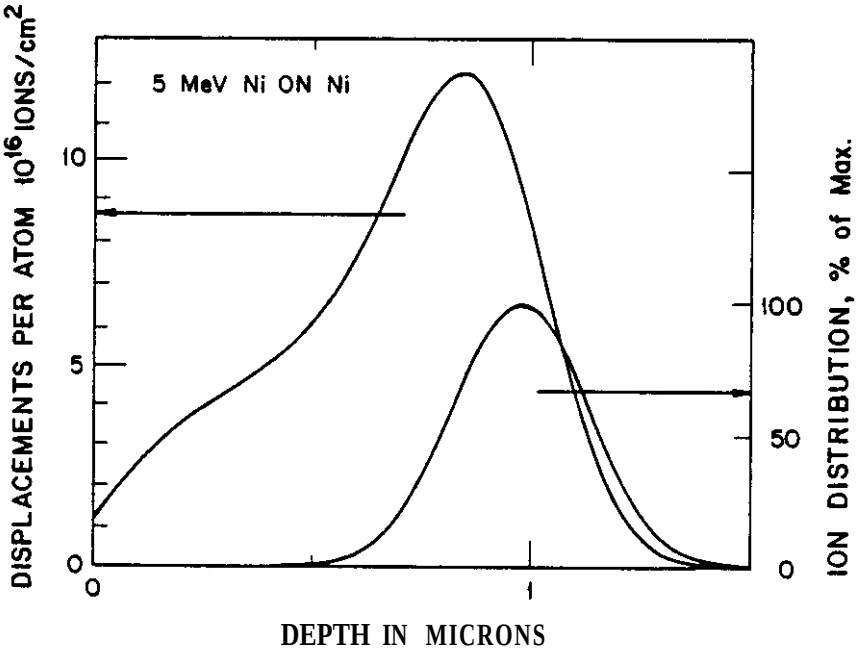

FIGURE 1. Displacement Damage and Ion Deposition Distribution for 5-MeV Nickel on Nickel Using the BRICE Code.(2)

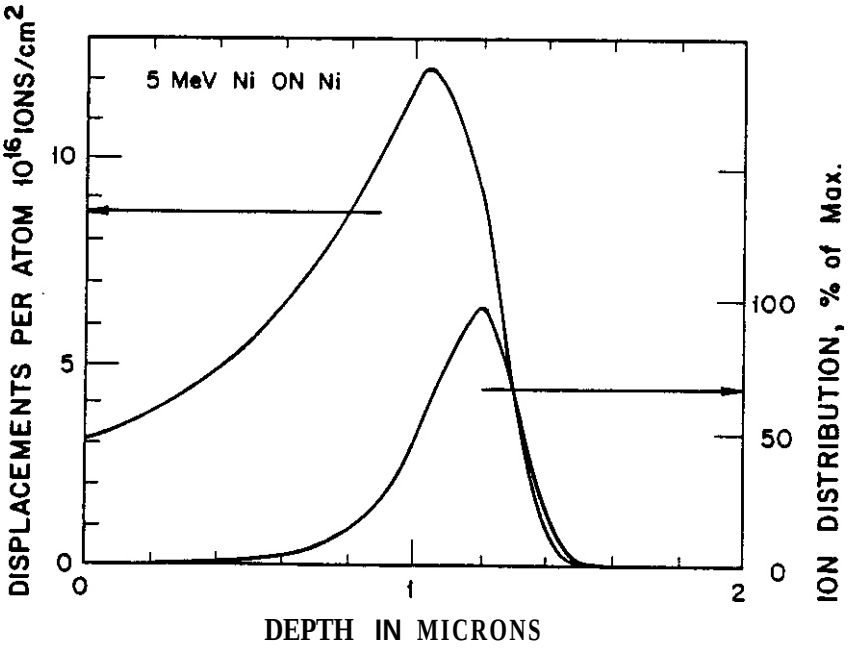

FIGURE 2. Displacement Damage and Ion Deposition Distribution for 5-MeV Nickel on Nickel Using the HERAD Code.(3)

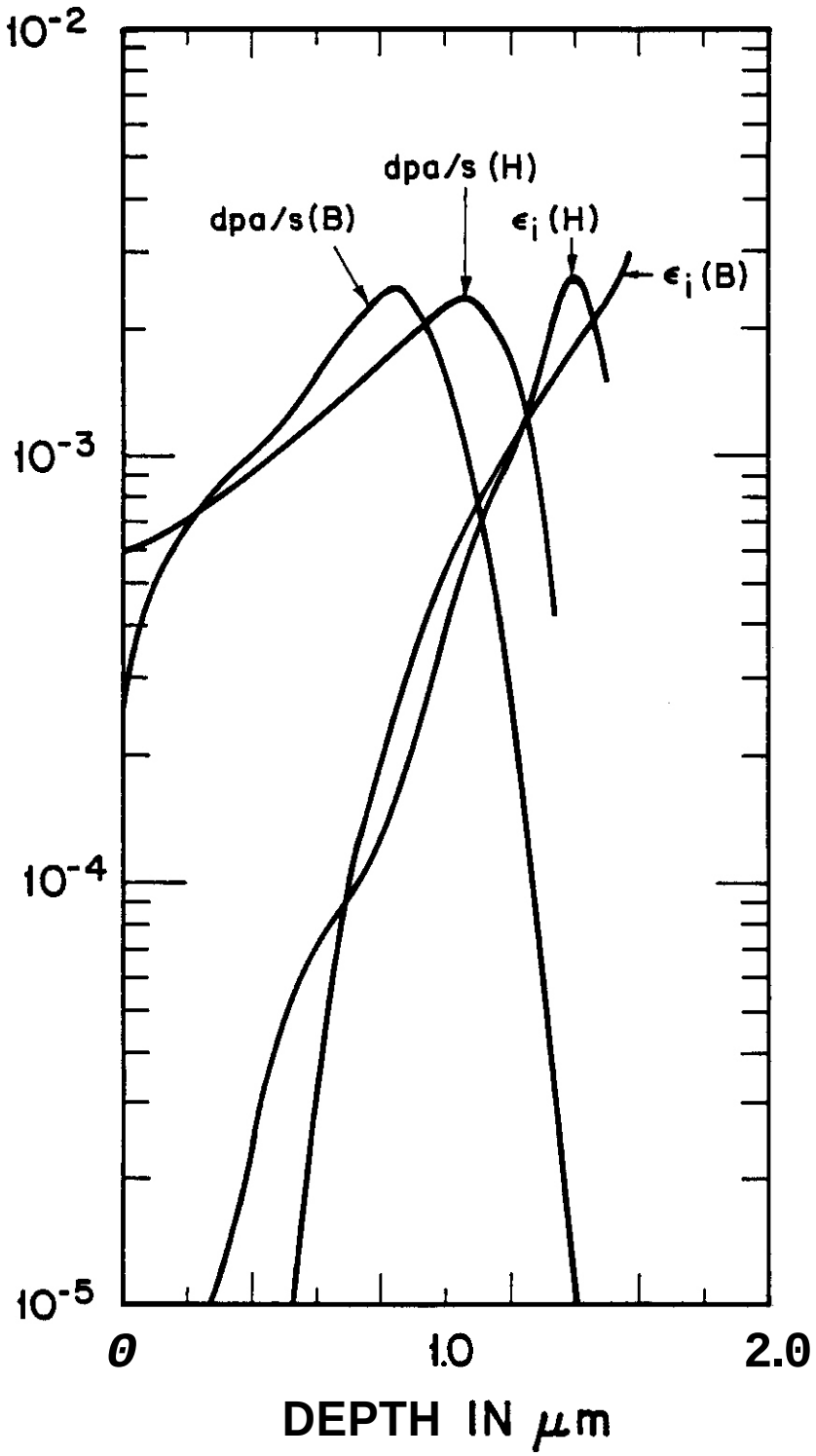

FIGURE 3. Comparison of the Displacement Rates and Excess Interstitial Fraction, ϵ_i, Between the BRICE (B) Code and the HERAD (H) Code.

Specifically, a dislocation density (sink strength) of 5E13 m^{-2} is assumed and the cascade survival fraction is taken as 0.25. Although the same vacancy formation and migration energies were used, 1.7 eV and 1.2 eV respectively, the self-diffusion pre-exponential factor is slightly different at 1.34E-6 m^2/sec. The old value was an experimentally determined value that was good for a particular vacancy migration energy only. To make the self-atom diffusivity internally consistent, a change in the vacancy migration energy must not only effect the exponential but also the pre-exponential. The formalism used is that developed by Seeger and Mehrer[4] where the pre-exponential is treated as a function of the vacancy migration energy. The change in the pre-exponential is most important at high temperatures (600°C) where previously[1] the calculated void nucleation rate dropped precipitously.

The depth and temperature dependence of the void nucleation rates for 5 MeV Ni on nickel is shown in Fig. 4 for the BRICE code, and in Fig. 5 for the HERAD code. The dashed lines in both figures represent the void nucleation rates with the injected interstitials neglected. The suppression of void nucleation is seen to be very significant except for the high temperature, 600°C, cases. In addition, large discrepancies in the void suppression between the BRICE and HERAD code are observed. Whereas the damage and ion deposition profiles from the BRICE code result in little suppression at 500°C, the profiles obtained with the HERAD code give a large suppression at 500°C. Even at 600°C the HERAD results give a significant reduction of void nucleation at the peak damage location.

The shift in the peak of swelling due to excess interstitial suppression can be larger for the HERAD code than for the BRICE code depending on the temperature.

The BRICE code results give a peak nucleation shift of $-$ 0.4 μ at 300°C (0.9 μ to 0.5 μ) while at 500°C the shift is ~ 0.2 μ (0.9 μ to 0.7 μ). The HERAD code results give a peak nucleation shift of $-$ 1 μ at 300°C (1.1 μ to 0.1 μ) while at 500°C the shift is $-$ 0.3 μ (1.1 μ to 0.8 μ).

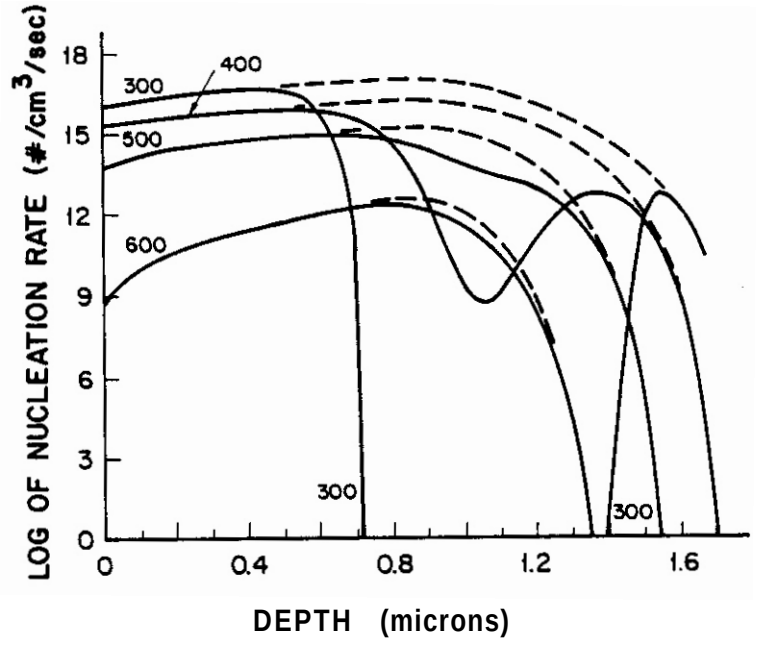

FIGURE 4. Void Nucleation Profile from BRICE Data.

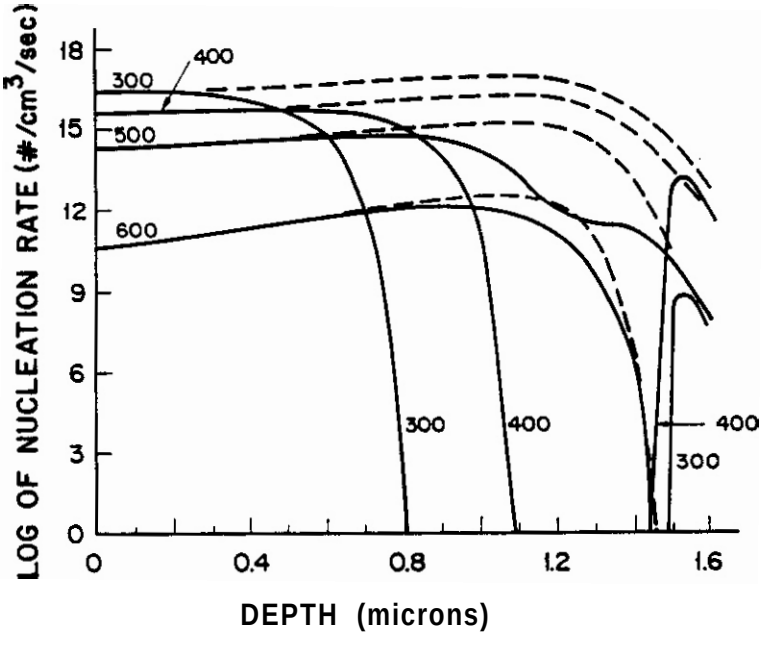

FIGURE 5. Void Nucleation Profile from HERAD Data.

5.4 Discussion

The void nucleation differences, obtained between the BRICE code and the HERAD code, occur because of the difference in the shape of the displacement rate and ion deposition profiles between the two codes. The BRICE code gives a Gaussian shape while the HERAD code gives a non-Gaussian shape exhibiting a more pronounced tail towards the surface. Because of the more detailed physical modeling of the collision process in HERAD and the absence of any compromising assumptions regarding the solution of the transport equation, the results of the HERAD code are expected to be more reliable.

The larger effect of the excess interstitials at (or near) the peak damage region in the HERAD case occurs because the ion-deposition profile does not exhibit as large a straggling at the end of range as the BRICE case. The larger shift in the peak nucleation as a function of temperature in the HERAD case occurs because of more straggling towards the surface than in the BRICE case. The long tail towards the surface gives a low excess interstitial fraction which is only significant at low temperatures when recombination dominates the point defect loss.

Regardless of which code is used, the effects of excess interstitials at this medium energy, 5 MeV, are more pronounced than in the 14 MeV results because the excess interstitials cover a larger fraction of the total range. When a more accurate displacement damage code such as HERAD is used the effect of injected interstitials is larger in the low and middle temperature range than might be expected strictly from analysis with the BRICE code.

6.0 References

1. D.L. Plumton and W.G. Wolfer, DOE/ER-0046/2, pp. 216-231.

2. D.K. Brice, SAND 75-0622 (1977).

3. H.M. Attaya, Doctoral Thesis, University of Wisconsin-Madison (1981).

4. A. Seeger and H. Mehrer, Vacancies and Interstitials in Metals, ed. by A. Seeger, D. Schumacher, W. Schilling and J. Diehl, North-Holland, Amsterdam, 1970, p. 1.

7.0 Future Work

Further evaluations will be performed on low-energy ion bombardment in the range from 10 keV to 1 MeV.

MICROSEGREGATION INDUCED IN Fe-35.5Ni-7.5Cr BY IRRADIATION IN EBR-II

H. R. Brager and F. A. Garner (Hanford Engineering Development Laboratory)

1.0 Objective

The object of this effort is to identify the microstructural and microchemical origins of the compositional dependence of radiation-induced swelling, creep and changes in mechanical properties in Fe-Ni-Cr alloys.

2.0 Summary

The examination was continued of composition oscillations in an annealed Fe-35.5Ni-7.5Cr alloy which is resistant to void formation. Energy dispersive x-ray measurements were made of the matrix composition along straight lines at smaller intervals (50 vs 200 nm) than previously reported. These data better delineate the oscillations in composition measured in this single phase material irradiated in the EBR-II at 593°C to ~40 dpa and verify previous EDX results. The matrix composition of unirradiated specimens were also examined by EDX and showed only minimal spatial variations.

The compositional variations of the irradiated material do not correlate with any currently existing microstructural feature and may arise from irradiation-assisted long-range ordering processes. The compositional oscillations occur on a scale of ~200 nm.

3.0 Program

Title: Irradiation Effects Analysis (AKJ)
Principal Investigator: D. G. Doran
Affiliation: Hanford Engineering Development Laboratory

4.0 Relevant DAFS Program Plan Task/Subtask

Subtask II.C.1. Effects of Material Parameters on Microstructure

5.0 Accomplishments and Status

5.1 Introduction

In several recent reports it has been shown that the swelling of relatively pure and annealed Fe-Ni-Cr alloys is sensitive to their chromium and nickel levels,[1-3] with the greatest resistance to swelling at ~35 wt% nickel and low chromium levels (<10 wt%). It was also shown that the matrix of the E37 alloy (Fe-35.5Ni-7.5Cr) actually densified during irradiation at 593°C, with the density increasing 0.9% at 7.6 x 10^{22} n/cm^2 (E > 0.1 MeV).

Since the E37 alloy is known to be near a composition at which the density of the alloy is a minimum, it was proposed that segregation of the alloy into regions that were enriched in nickel at the expense of other regions would lead to a net densification of the alloy.[4] Examination of this alloy by microscopy and EDX microanalysis did not reveal the presence of any precipitate phases, however. Additional EDX examination[4] showed that there were substantial reproducible variations in composition along any linear traverse across the specimen. Not only did the local nickel content vary substantially (25-53%) but those areas enriched in nickel were depleted in chromium and iron, with the reverse being true in regions of low nickel content.[4]

The conclusions reached in the previous report[4] are subject to several reservations. First the variation in matrix composition was measured along lines with spacings equal to ~200 nm. The possibility of the observed perturbations occurring over shorter intervals needed to be investigated. Second, it is assumed that the compositional variation, which appears to be irradiation-induced and spinodal in nature, extends in all three dimensions. Only a limited number of sets (four) of reproducible compositional traces were originally obtained and these were limited by the small concentration of identifiable features. It is possible that the variations observed were distorted by the averaging effect of the beam over the foil thickness. Third, the compositional variation in unirradiated material was not studied. These deficiencies were addressed in the current study.

5.2 Results

A problem in analyzing this irradiated alloy was the relative absence of identifiable microstructural features from which one could start measuring alloy compositions. This lack of features was also true in the unirradiated material.

5.2.1 Unirradiated Specimen

An unirradiated specimen of alloy E37 was examined in order to determine the magnitude of the variations of the solute concentrations in the as-processed material. The identification marker used in this example was a small chromium rich inclusion, Figures 1 and 2. The compositional variations of the matrix are rather minimal, with the nickel content varying only from 34.2 to 36.6% along a traverse of ~600 nm. In those measurements the electron beam diameter of the JEOLCO 100 CX STEM was approximately the same nominal size (~30 nm) used for the irradiated specimens. The foil thickness examined was ~50 nm.

5.2.2 Irradiated Specimen

The compositional variations observed in alloy E37 after irradiation are much larger. Using a dislocation as a marker (Figure 3), variations in nickel content ranged from 32 to 42%. In all cases the chromium and iron concentration behaved opposite to that of nickel as observed previously. Note that the characteristic distance over which the compositional oscillation occurs is still on the order of 2.200 nm. Similar behavior was observed in some respects in thin-foil traverses using other markers such as precipitates (Figure 4), voids (Figure 5) and grain boundaries (Figure 6). Note that the largest variations often occur with the microstructural features known to segregate nickel, such as voids and grain boundaries.[5-6] Figure 6 also shows how the use of thicker foils tends to average out the compositional variations. In an area where a grain boundary is the dominant sink, the

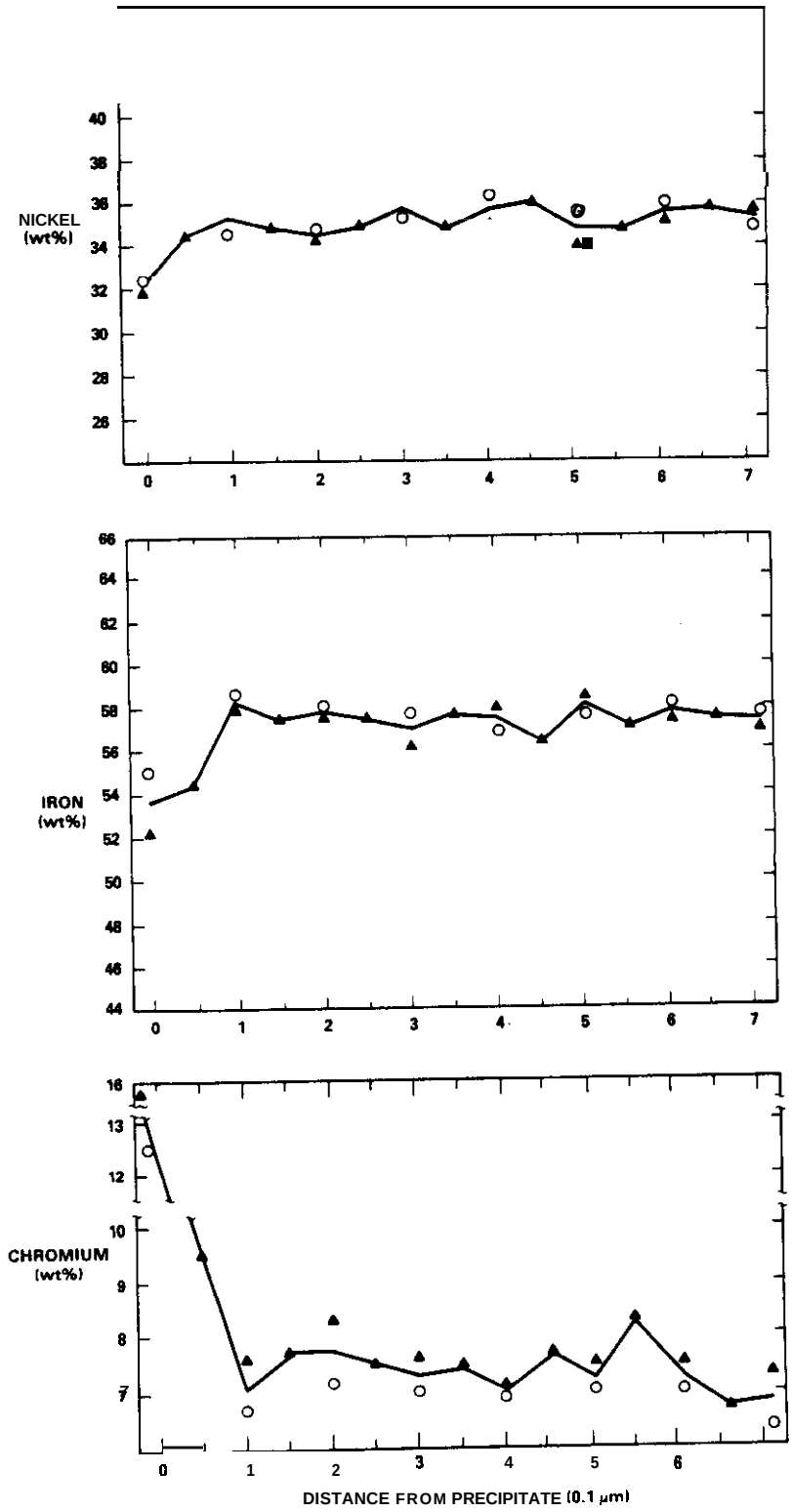

FIGURE 1. Compositional Variations Observed in a Thin-Foil Traverse on One Side of a Precipitate-Inclusion in Unirradiated Alloy E37. Figures with open circle and closed triangle symbols represent alloy concentrations measured on two independent scans to illustrate the reproducibility in the spatial variation of the alloy composition.

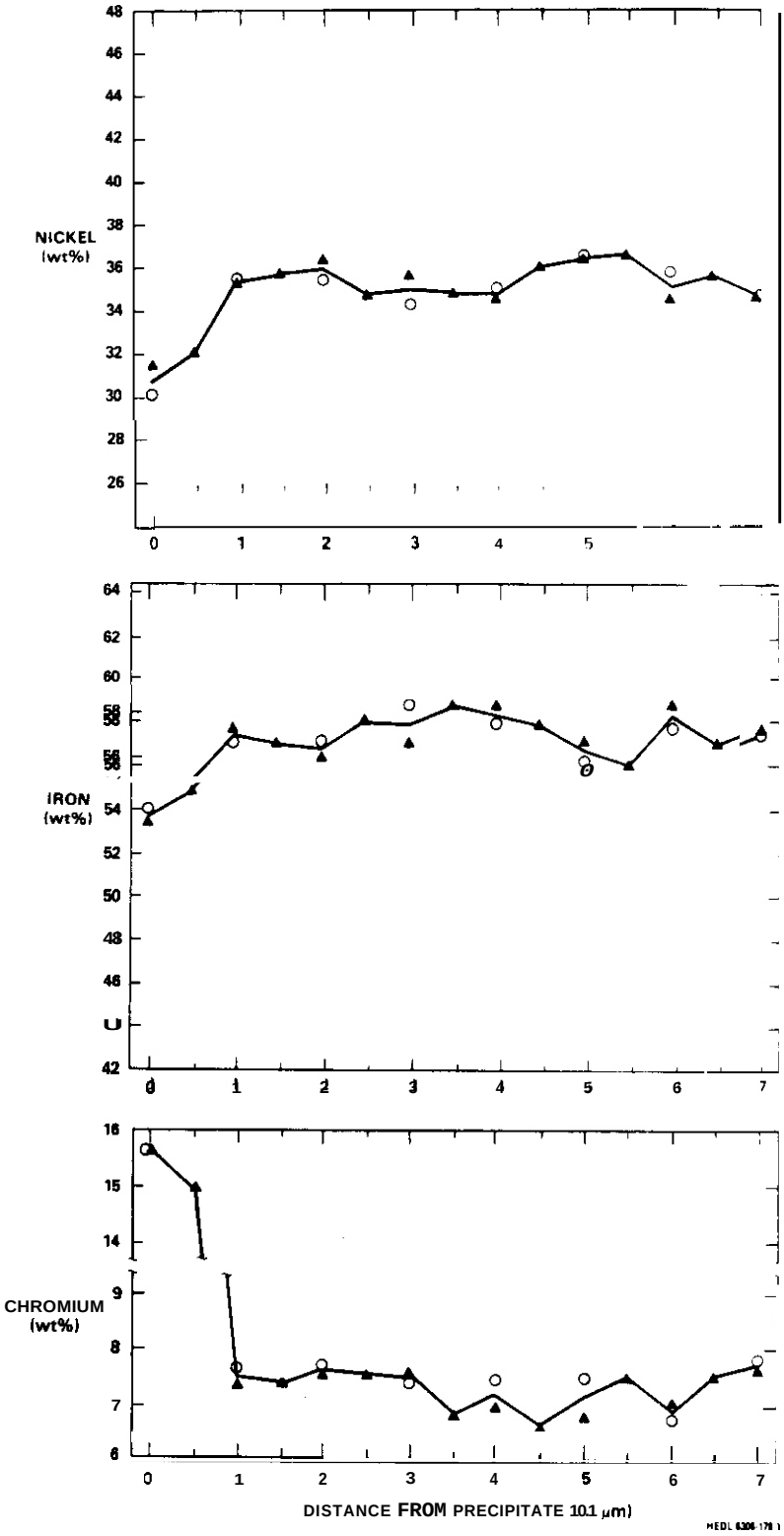

FIGURE 2. **Compositional Traverse of Unirradiated** Alloy E37 **on the Other Side** of **Precipitate Identified in Figure** 1.

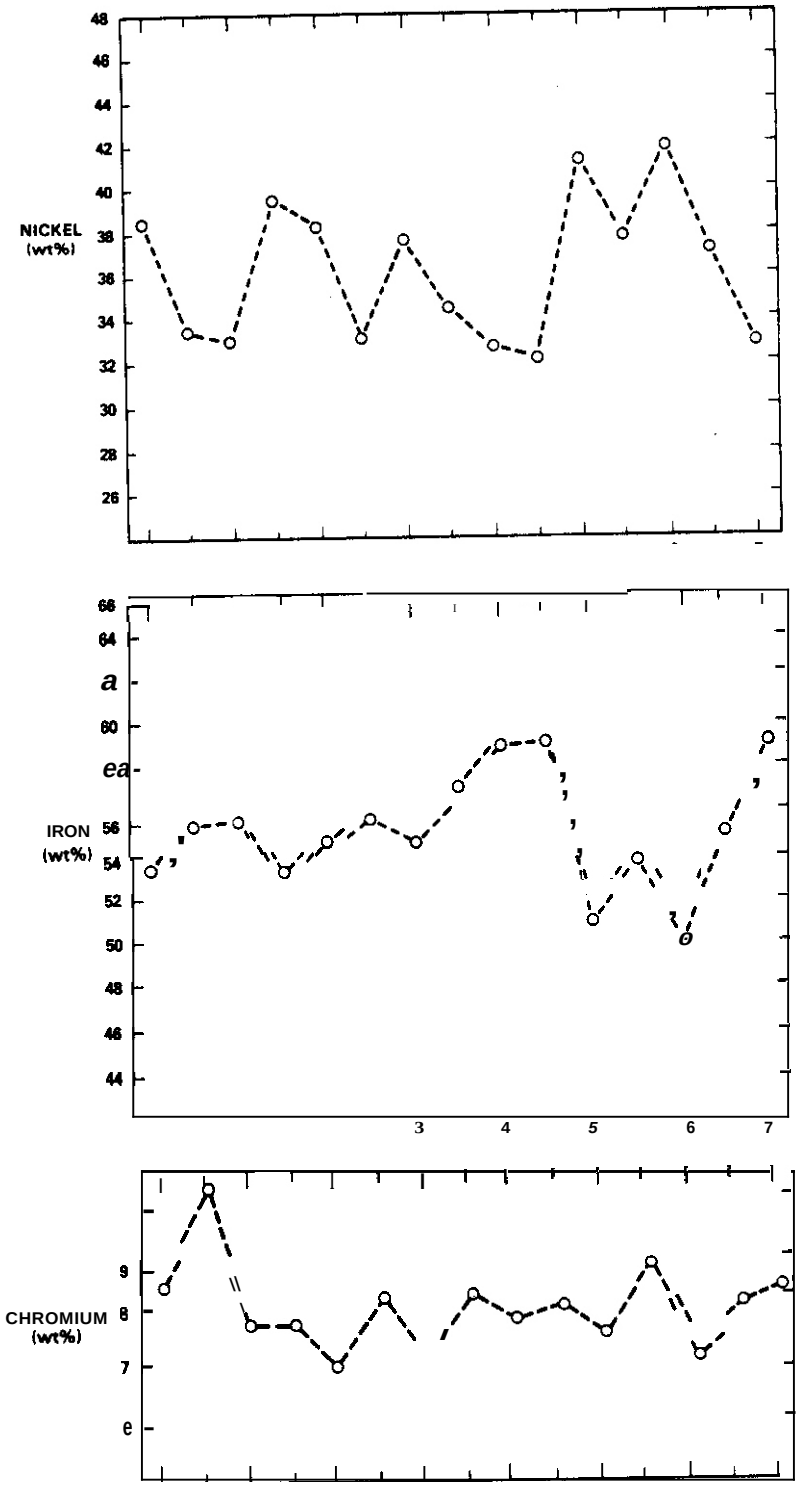
NICKEL
(wt%)
48
46
44
42
40
38
36
34
32
30
28
26
IRON
(wt%)
66
64
60
56
54
52
50
48
46
44
3
4
5
6
7
CHROMIUM
(wt%)
9
8
7

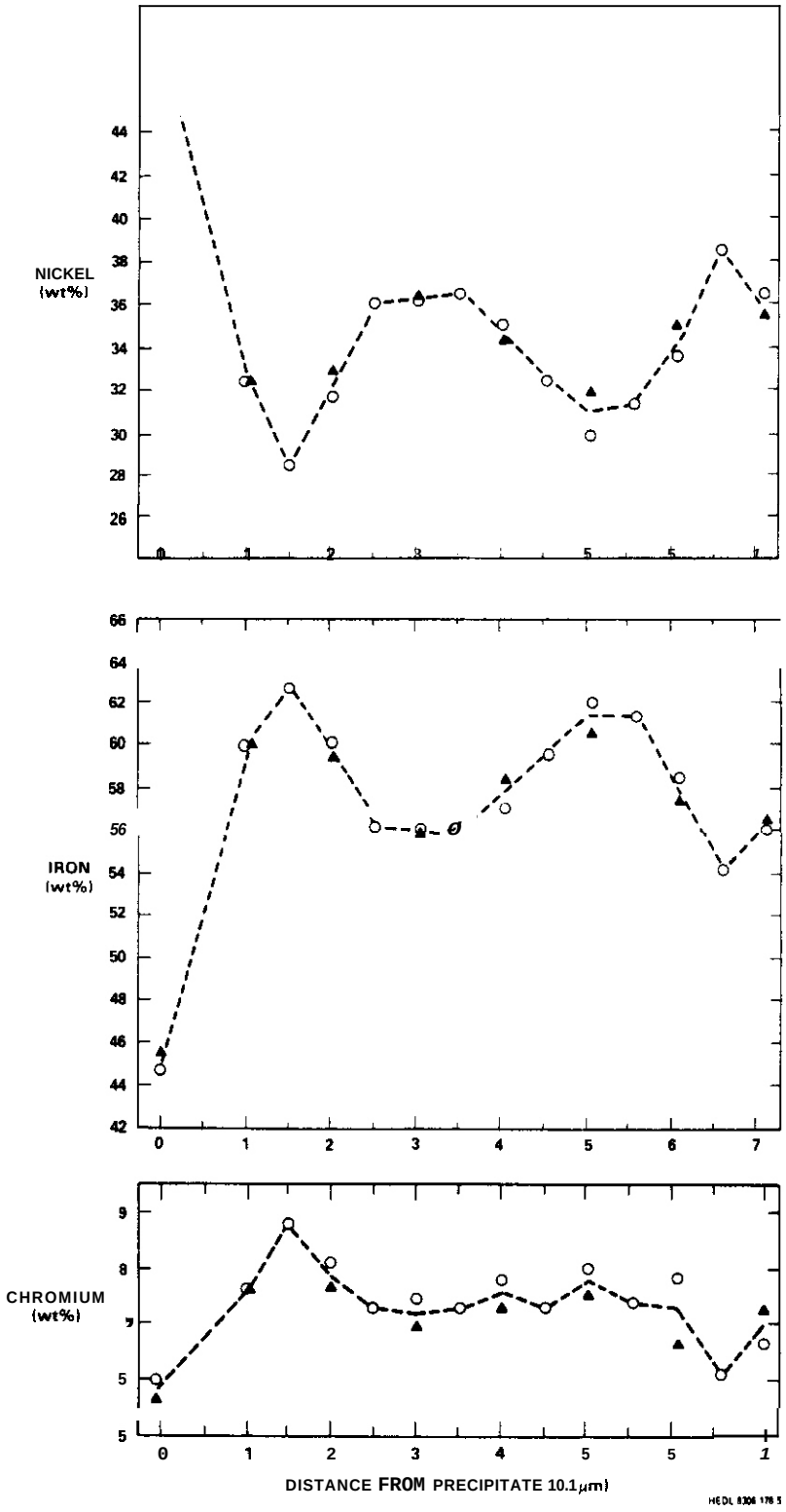

FIGURE 4. Thin-Foil Compositional Traverse in Irradiated Alloy E37 Using a Precipitate as a Location Marker.

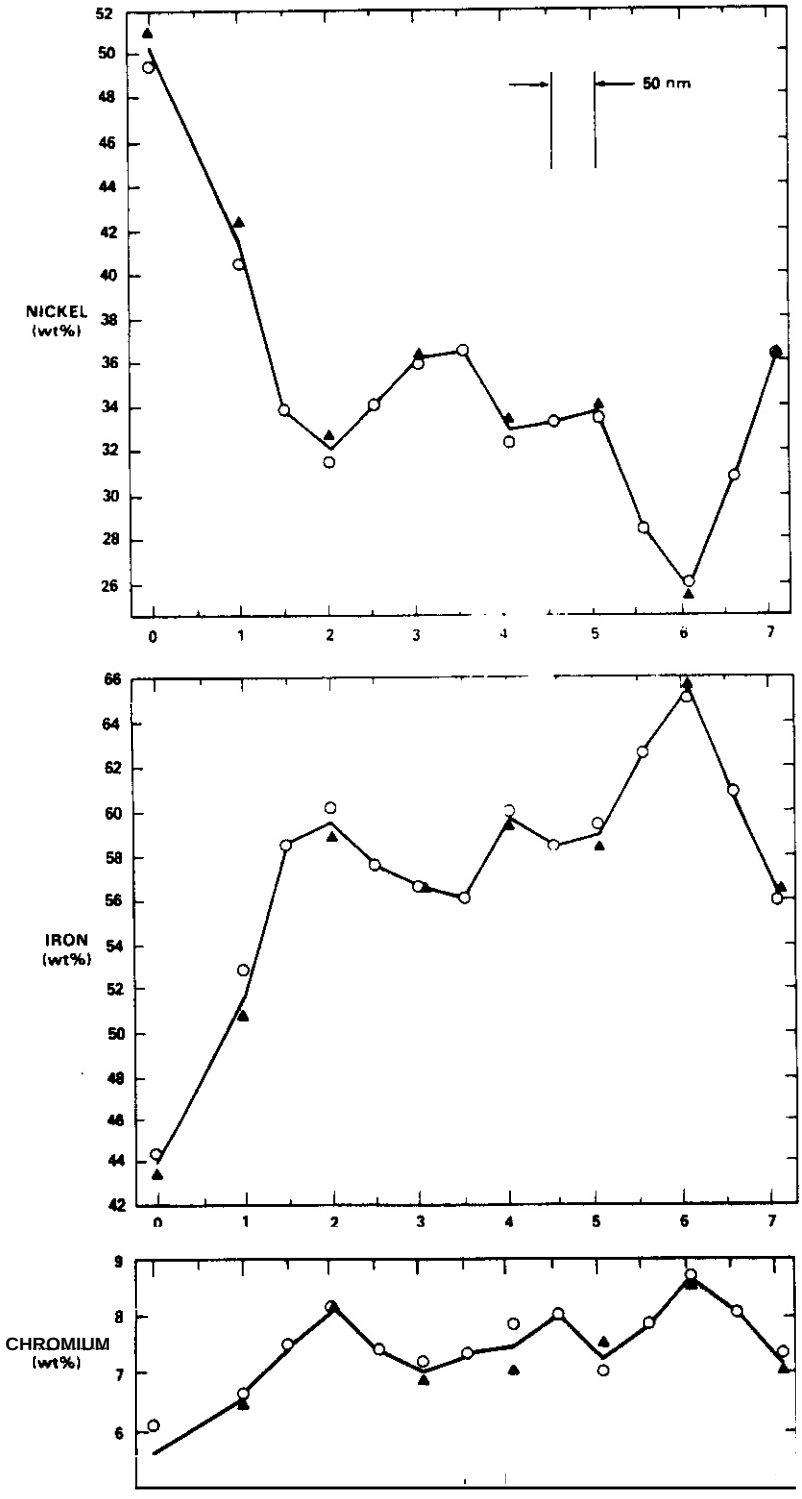
50 nm
NICKEL (wt%)
IRON (wt%)
CHROMIUM (wt%)

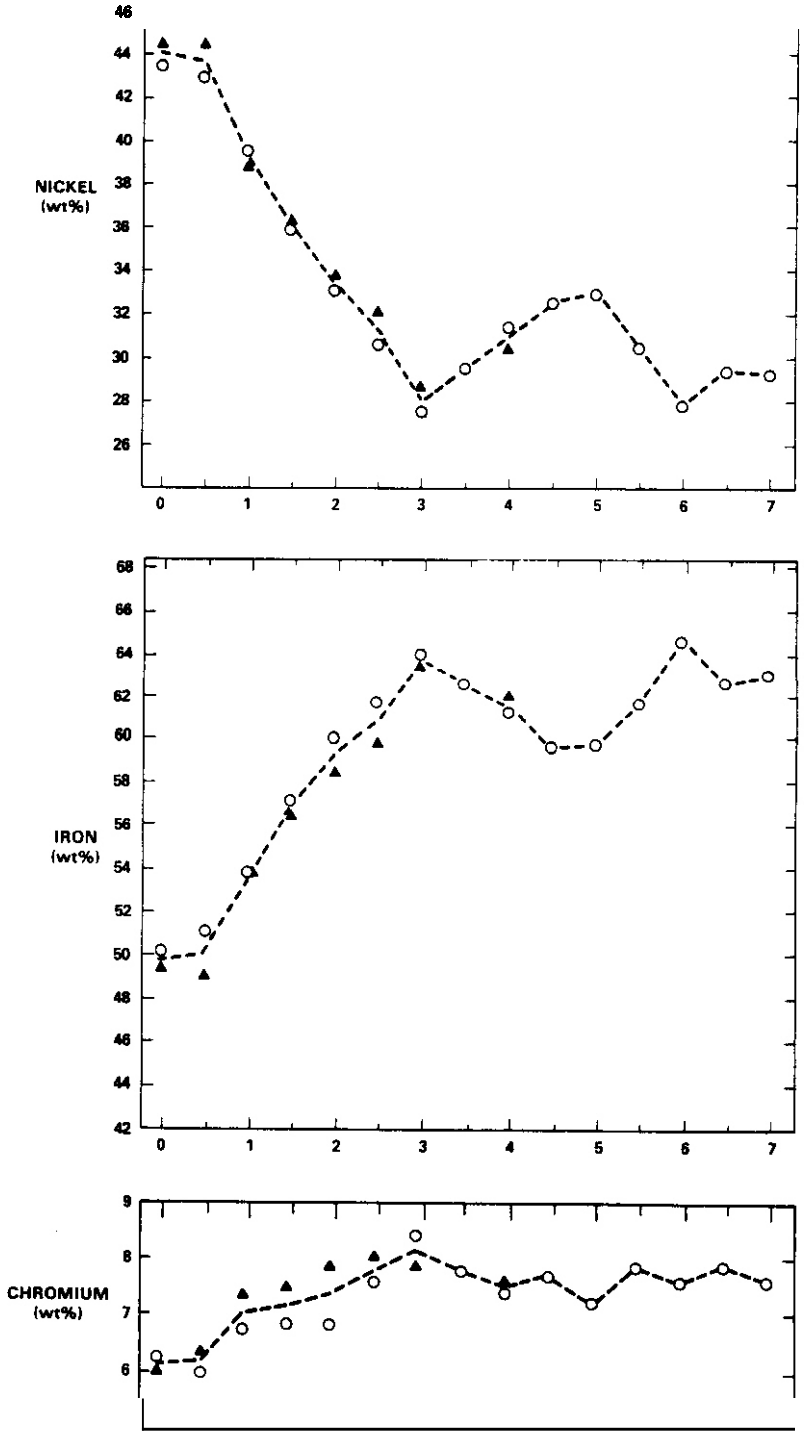

FIGURE 6a. **Thin-Foil Traverse in Irradiated Alloy** E37 **Using a Grain Boundary as Marker.**

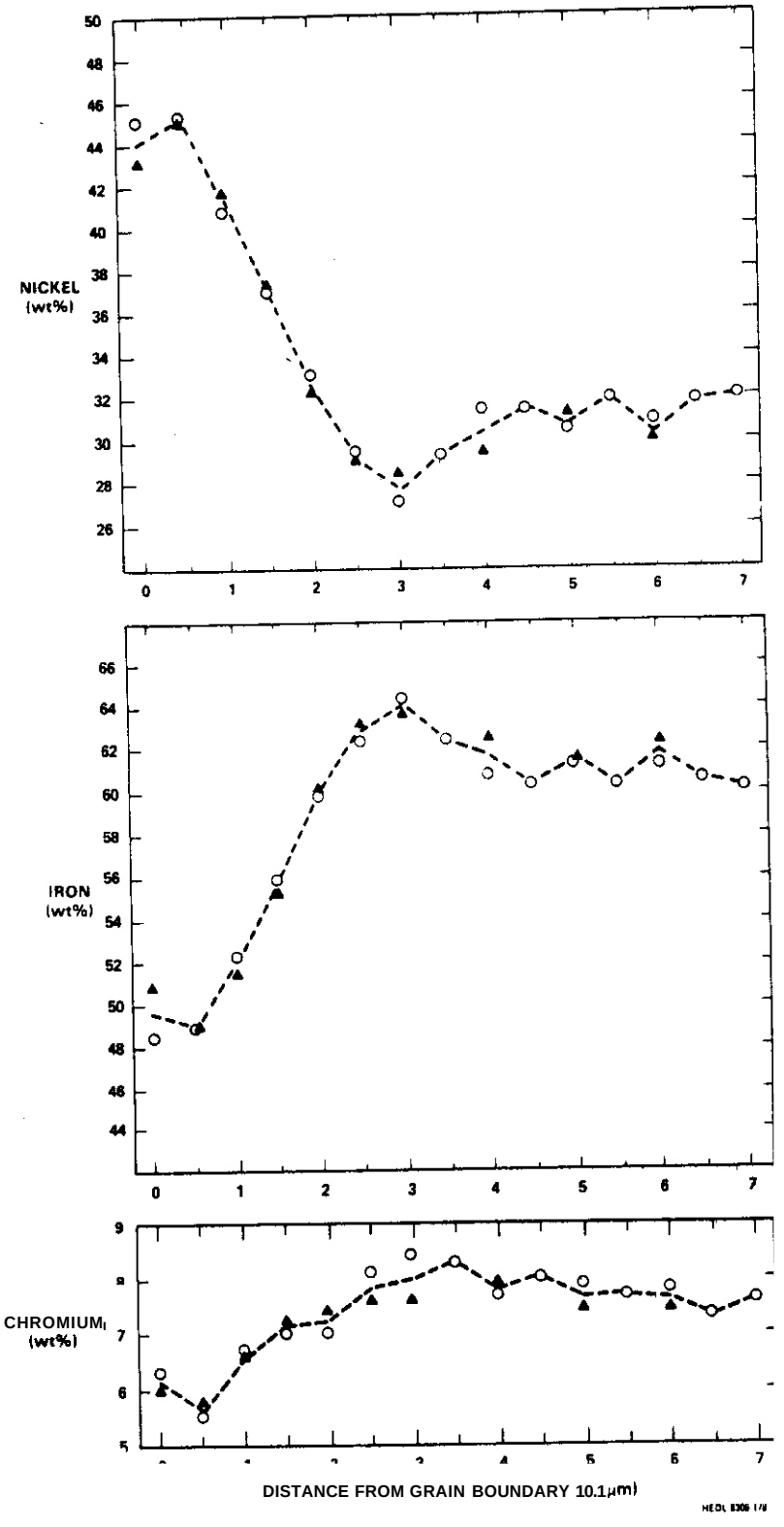

FIGURE 6b. Thick-Foil Traverse in Irradiated Alloy E37 Using a Grain Boundary as Marker.

thicker foil measurement shows a much lower degree of variation in the depleted region far from the grain boundary.

5.3 Discussion

It appears that the variation of composition arises from at least two possibly separate sources. The largest variations in the matrix composition at locations which were not adjacent to observable features, might be associated with large microstructural features shown in this study to segregate nickel. These features, such as grain boundaries and voids, would need to be located in regions adjacent to the thin foil but were removed during sample preparation. However, with the very low density of these features found within the foil volume, it appears that the numerous and relatively substantial variations in alloy composition cannot be correlated solely with such visible microstructural features.

One might also postulate that small radiation-induced dislocation loops may have once occupied the regions of higher nickel content and initiated compositional variations which persist after the growth, unfaulting and movement of the resulting dislocation. It is considered more likely however, that the observed oscillations in matrix composition occur spontaneously during irradiation. This possibility will be discussed in more detail in the next report.

The range of the measurements reported here are limited by the size of the electron probe employed and the thickness of the foil examined. Under consideration are the possibilities of using either the smaller probe available on the HB501 STEM or a field ion microscope.

5.4 Conclusions

The examination was continued of composition oscillations in an annealed Fe-35.5Ni-7.5Cr alloy which is resistant to void formation. Energy dispersive x-ray measurements were made of the matrix composition along

straight lines at smaller intervals (50 vs 200 nm) than previously reported. These data better delineate the oscillations in composition measured in this single phase material irradiated in the EBR-II at 593°C to ~40 dpa and verify previous EDX results. The matrix composition of unirradiated specimens were also examined by EDX and showed only minimal spatial variations.

The compositional variations of the irradiated material do not correlate with any currently existing microstructural feature and may arise from irradiation-assisted long-range ordering processes. The compositional oscillations occur on a scale of ~200 nm.

6.0 References

1. F. A. Garner, "Dependence of Swelling on Nickel and Chromium Content in Fe-Cr-Ni Ternary Alloys," this report.

2. H. R. Brager and F. A. Garner, "Dependence of Swelling of Fe-Ni-Cr Alloys on Chromium and Nickel Content," DAFS Quarterly Progress Report, DOE/ER-0046/11, p. 221.

3. H. R. Brager and F. A. Garner, "Swelling of High-Nickel Ternary Alloys in EBR-II," this report.

4. H. R. Brager and F. A. Garner, "Radiation-Induced Evolution of Fe-Ni-Cr Alloys," DAFS Quarterly Progress Report, DOE/ER-0046/12, p. 170.

5. H. R. Braoer and F. A. Garner. "Analysis of Radiation-Induced Microchemical Evolution in 300 Series Stainless Steel," Advanced Techniques for Characterizing Microstructures, F. W. Wiffen and J. A. Spitznagel, Eds., The Metallurgical Society of AIME, p. 97, 1982.

6. W. G. Johnston, W. G. Morris and A. M. Turkalo, "Excess Subsurface Swelling Produced by Nickel Ion Bombardment," Radiation Effects in Breeder Reactor Structural Materials, M. L. Bleiberg and J. W. Bennett, Eds., The Metallurgical Society of AIME, p. 421, 1977.

7.0 Future Work

This study will continue, concentrating primarily on the origins of the compositional oscillations that are not associated with currently visible microstructural components and also on the consequences of segregation on void nucleation and growth. Additional experimental work will proceed on other ternary alloys at different irradiation conditions.

8.0 Pubiications

None.

DEPENDENCE OF SWELLING ON NICKEL AND CHROMIUM CONTENT IN Fe-Ni-Cr TERNARY ALLOYS

F. A. Garner (Hanford Engineering Development Laboratory)

1.0 Objective

The objective of this effort is to determine the role played by each major element in the radiation-induced microchemical evolution of irradiated alloys.

2.0 Summary

The steady-state swelling rate of EBR-II irradiated ternary alloys with $\leq$35% nickel appears to be approximately 5% per 10^{22} n cm^{-2} (E > 0.1 MeV) or 1%/dpa, independent of chromium and/or nickel content and also independent of the irradiation temperature in the range 400-600°C. The duration of the transient regime of swelling is sensitive to these three variables, however, tending to increase with increasing nickel or temperature or decreasing chromium content. A similar relative independence of the steady-state swelling rate on temperature has been also observed in commercial stainless steels, which also appear to be approaching a swelling rate of 1%/dpa at high fluence. There is some evidence that elemental segregation plays a role in the compositional dependence of swelling.

3.0 Program

Title: Radiation Effects Analysis (AKJ)
Principal Investigator: D. G. Doran
Affiliation: Hanford Engineering Development Laboratory

4.0 Relevent Program Plan Task/Subtask

Subtask II.C.1 Effect of Material Parameters on Microstructure

5.0 Accomplishments and Status

5.1 Introduction

It has been shown that the swelling of both ternary and commercial alloys during ion bombardment can be correlated to the nickel content of each alloy.[1,2] As shown in Figure 1, swelling of ternary alloys is sensitive to the iron, nickel and chromium levels, but most strongly linked to the nickel content at levels below 35-40% nickel. This behavior has been confirmed in some aspects by irradiations conducted in the fast reactor designated EBR-II.[3,4] Neither the previously published reactor or ion-generated data provide a definitive clue as to whether the nickel or chromium content affects the incubation period, steady-state swelling rate or both.

Recently additional swelling data have become available for ternary alloys irradiated in EBR-II to fluences as large as 12.1 x 10^{22} n/cm^2 (E > 0.1 MeV) or 60 dpa. These data are shown in Table 1. In this report it is shown that a significant amount of insight can be extracted from these data and applied to the modeling of the compositional dependence of swelling.

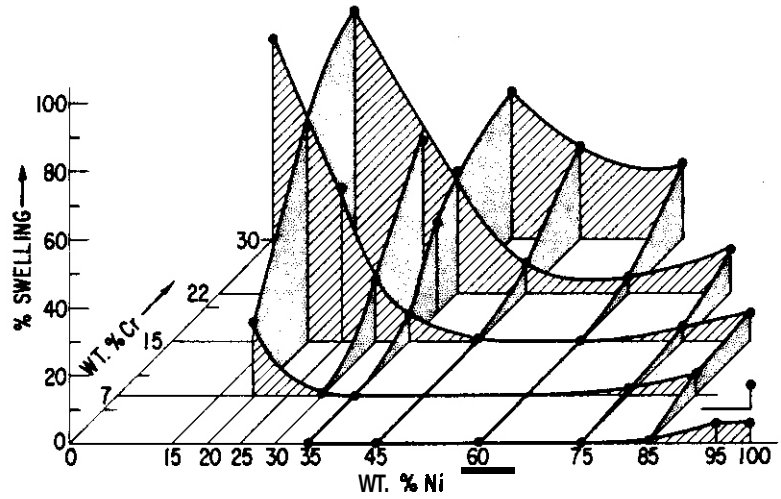

FIGURE 1. Composition Dependence of Swelling in 5 MeV Ni^+ Ion-Irradiated Fe-Ni-Cr Alloys at 675°C and 140 dpa.[1,2]

TABLE 1 (5)

Temperature (°C)			400	427	454	482	510	538	593	650
Fluence (10^{21} n/cm², E >0.1 MeV)			1.6 3.7 -	2.2 4.7 6.6	1.9 3.0 - 7.1	2.4 4.1 6.3 9.1	2.6 5.3 7.3 11.2	2.7 5.0 7.2 11.0	2.9 5.5 7.6 12.1	2.9 5.4 7.5 12.0
Alloy	Ni (wt. %)	Cr (Wt. %)								
E18	12.1	15.1	- 8.19 -	- 14.4 -	- - -	- 14.5 26.1 -	- 22.5 - -	- 21.2 - -	- 1.82 5.07 -	- 0.81 - 4.31
E9C	15.7	15.6	1.53 8.52 -	2.74 17.0 21.6	2.91 - - -	3.08 - - -	3.77 22.0 - -	0.14 10.3 18.9 -	0.05 0.41 1.32 11.23	0.03 0.11 0.70 1.56
E39	20.3	7.5	1.23 8.50 -	1.92 - -	0.26 - - -	0.19 7.79 - -	0.34 - 18.8 -	0.11 - 0.85 1.07	0.09 -0.16 -0.16 -	0.09 - - .32
E28	20.3	11.8	0.44 7.62 -	1.40 13.6 19.2	1.10 8.98 - -	1.33 11.3 22.8 -	1.49 4.95 24.6 -	0.24 0.75 1.84 4.86	0.19 0.08 0.54 2.37	0.06 0.0 0.26 1.33
E19	19.4	14.9	0.77 8.41 -	1.55 13.8 20.2	1.33 10.7 -	1.46 10.5 25.2	1.77 12.7 26.4	0.17 2.66 10.5 -	0.13 0.18 0.47 -	0.06 0.09 0.40 .36
E27	24.7	10.2	0.91 9.75	0.85 10.9	0.28 5.26	0.25 3.17	0.27 0.80 4.23	0.28 0.46 0.71	0.08 0.02 -.68	0.23 0.82
E20	24.4	14.9	0.95 8.20 -	1.47 13.3 -	0.79 7.90 -	0.68 9.93 20.2	1.05 6.96 24.5	0.24 0.61 1.95	0.11 -0.18 0.32 -	-0.03 -.26 0.04 .35
E21	29.6	15.3	0.71 9.22 -	0.86 13.6 20.0	0.26 8.52 - 12.11	0.24 4.49 9.32 21.82	0.30 2.18 10.4 21.82	0.16 0.55 1.55 -	0.07 -0.15 0.23 -	0.00 -0.07 0.17 0.20
E37	35.5	7.5	0.07 0.25 -	0.0 0.58 1.32	0.03 -0.11 -	.02 -.24 -.10	.03 -.29 -.19	.02 -.17 -.23	-.02 -.22 -.86 -	.05 -.19 -.23 -.49
E22	34.5	15.1	.47 2.76 -	.24 2.12 4.60	.16 1.05 - 4.19	.17 .82 1.78 3.65	.20 .29 1.76 2.59	0.15 .17 .85 .61	.07 -.31 -1.16 -	.02 -.25 .02 -.12
E38	35.2	20.0	.54 2.89 -	.53 3.31 8.51	.20 1.79 - 7.69	.22 2.51 4.72 12.79	.29 2.50 9.58 -	.13 .55 2.46 13.84	.02 -.44 -.39 -	.03 -.17 .38 1.88
E25	35.1	21.7	.53 3.63 -	.47 3.49 9.91	.23 2.33 - 8.70	.29 3.56 8.55 19.92	.32 4.76 13.1 -	.80 2.07 7.71 23.87	.14 -.45 .70 -	.07 -.25 .48 4.65
E23	45.3	15.0	.16 .30 -	.13 .97 3.18	.21 .54 -	.32 .66 1.02	.36 .20 1.41	.15 -.14 .16	.10 -.42 -.27	.13 -.36 .02 .15
E24	75.1	14.6	.28 .38 -	.36 - 1.84	.32 .80 -	.54 1.07 2.89	.69 1.57 3.99 -	.93 1.07 2.47 4.77	.65 -.12 -.52 0.33	.03 -.30 .76 12.06
E36	84.9	15.1	.23 .22 -	.30 .62 1.11	.22 .11 -	.34 .34 1.27	.33 .69 1.62	.40 .80 1.13	.19 -.17 .13 -	-.03 -.15 .11

5.2 Data Analysis

It should be noted in Table 1 that for a given alloy composition and temperature there are occasionally four data points at different fluences. Most often there are only three data points, however, and occasionally only two, one or no data. Therefore, attempts to extract steady-state swelling rates or *to* define an incubation-plus-linear swelling curve for a single alloy and temperature lead to substantial uncertainty, particularly when one attempts to determine the separate effects of temperature, composition, natural data scatter and possibly displacement rate. The last variable is not usually considered in analyses of neutron-induced swelling data.

An alternate approach to the analysis of this data is to group the data in composition-related subsets which are defined by temperature and composition limits that confine a minimum variation of swelling within the data set. If such limits can be defined then trends within and between subsets can be sought to provide the needed insight. The compositions of the ternary alloys examined in this study are shown in Table 2.

5.3 Dependence of Swelling on Nickel Content

Figure 2 shows the swelling observed in a data subset containing only those alloys designated E18, E90 and E19 at temperatures of 400, 427, 454, 482 and 510°C. These alloys have 14.9 - 15.6% chromium and have nickel contents of 12.1, 15.7 and 19.4% nickel respectively. When plotted in this manner it becomes very clear that swelling is relatively insensitive to both temperature and nickel content in this range. No consistent internal trends with temperature, nickel content, neutron flux or irradiation position can be discerned within the subset. This implies that the scatter about the trend line shown in Figure 2 arises primarily from measurement error and the natural variation of the swelling process. The trend line shown in Figure 2 has a slope of 5% per 10^{22} n cm^{-2} ($E > 0.1$ MeV) or 1% per dpa and is reproduced for comparison purposes in Figures 4 through 8.

TABLE 2

COMPOSITIONS OF THE SIMPLE FE-NI-CR ALLOYS

Designation	Fe	Ni	Cr	C	O	N
E18	Bal	12.1	15.1	.005	.016	.0024
E90	Bal	15.7	15.6	.013	---	---
E39	Bal	20.3	7.5	.004	.016	.0014
E26	Bal	20.1	11.8	.002	.016	.0019
E19	Bal	19.4	14.9	.003	.018	.0015
E27	Bal	24.7	10.2	<.001	.012	.0017
E20	Bal	24.4	14.9	.003	.017	.0017
E21	Bal	29.6	15.3	.004	.017	.0020
E37	Bal	35.5	7.5	.002	.016	.0013
E22	Bal	34.5	15.1	.003	.017	,0021
E38	Bal	35.2	20.0	.004	.017	.0010
E25	Bal	35.1	21.7	.004	.015	.0020
E23	Bal	45.3	15.0	.002	.014	.0017
E24	Bal	75.1	14.6	.001	.0077	.0011
E36	---	84.9	15.1	.002	.0064	.0010

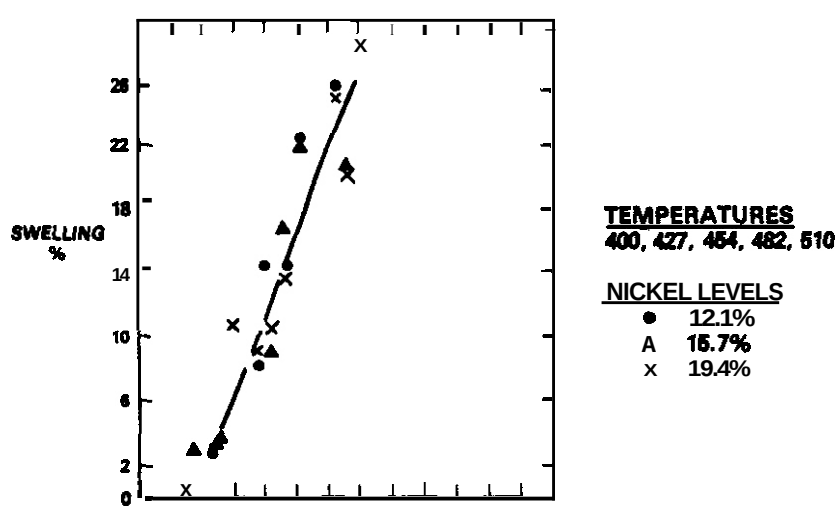

FIGURE 2. Swelling in Neutron-Irradiated Ternary Alloys at Temperatures Below 510°C for Nickel Levels of 12.1, 15.7 and 19.4%.

figures 3a - 3c show the trend band of the data contained in Figure 2 as well as the data for the same three alloys at 538, 593°C and 650°C. It appears that the primary effect of increasing temperature is to extend the transient portion of the swelling curve. Most importantly however, there now appears to be a clear separation of the swelling curves with increasing nickel content at each temperature, a trend that was not discernible at 400-510°C. Note that the swelling rate at 538°C for the 15.7 and 19.4% nickel levels is clearly comparable to that of the 400-510°C trend band. At 593°C the data are incomplete at 12.1 x 10^{22} n cm^{-2} but the E90 alloy (15.7% Ni) has clearly reached a swelling rate comparable to that of the 400-510°C and 538°C data subsets. The data at 650°C have not reached a sufficient fluence to determine if the same steady-state swelling rate will also be reached at this temperature.

Figure 4a shows the data subset comprising the alloys E20 and E27 at 24.4 and 24.7% Ni, and 14.9 and 10.2% Cr respectively. Note that with one exception, these data also fall into a tight grouping, falling in qeneral just a little to the right of the trend line shown in Figure 2 for the 12.1 to 19.4% Ni subset. Note in Figure 4b that at higher temperatures the transient regime of swelling is again progressively extended, but that at 538°C the steady-state swelling rate is comparable to that of the two low temperature subsets presented in Figures 2, 3a and 4a.

Figure 5 shows that in the range 400 to 454°C all but one of the data points at 29.6% Ni - 15.3% Cr (E-21) agree with the trend line of the 12.1 to 19.4% Ni subset. Note that where the steady-state slopes can be determined at higher temperatures they are again comparable to that of the trend line, but the duration of the transient regime increases with temperature.

Figure 6a shows that at 34.5% Ni and 15.1% Cr the incubation periods have been extended to fluences large enough such that the steady-state swelling rates cannot be determined at even the lowest irradiation temperature. The trends with temperature are consistent with those of previous data subsets however.

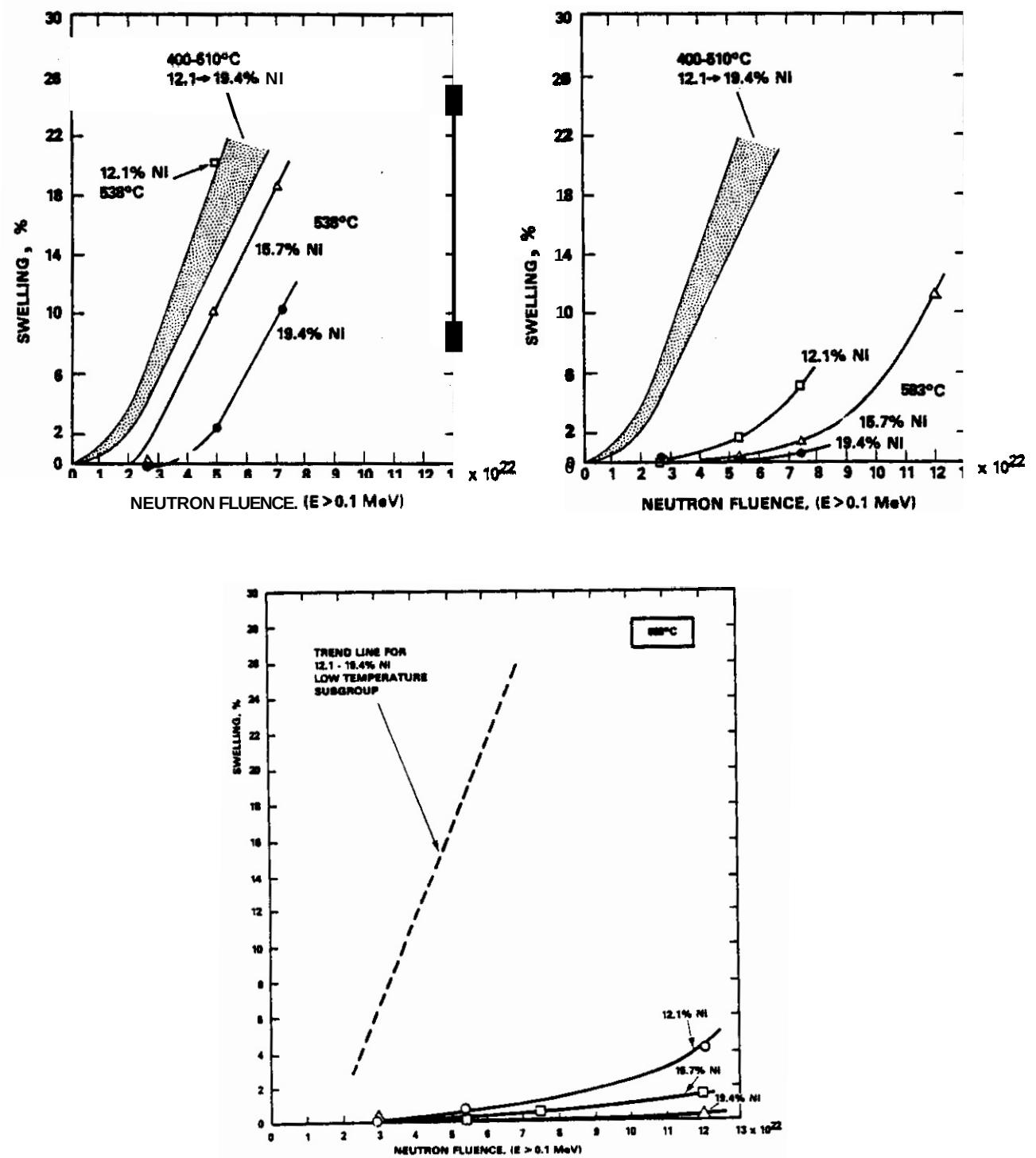

FIGURE 3. Swelling in Neutron-Irradiated Ternary Alloys at Temperatures of 538, 593, 650°C for Nickel Levels of 12.1, 15.7 and 19.4%. Note the extension of the transient regime of swelling with increasing temperature and nickel content.

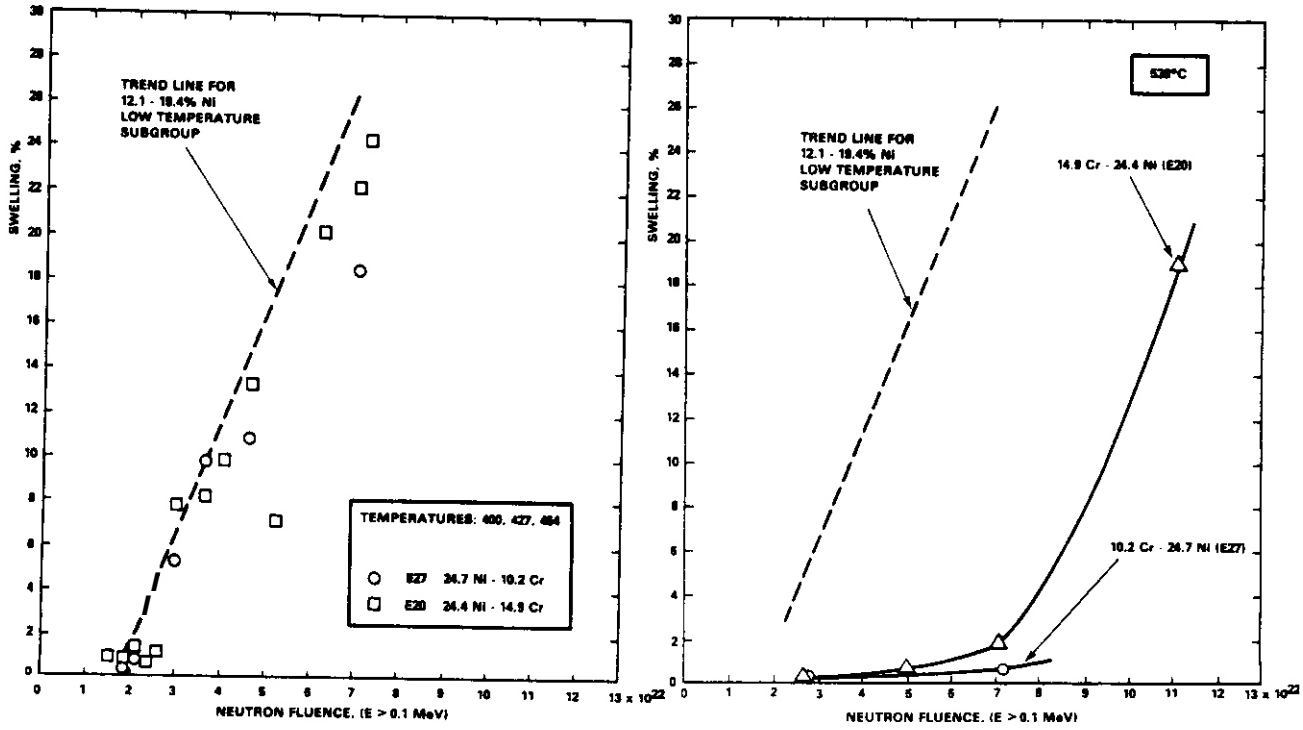

FIGURE 4. **Swelling** of **Two Alloys with** 24.4–24.7% **Nickel Content.**

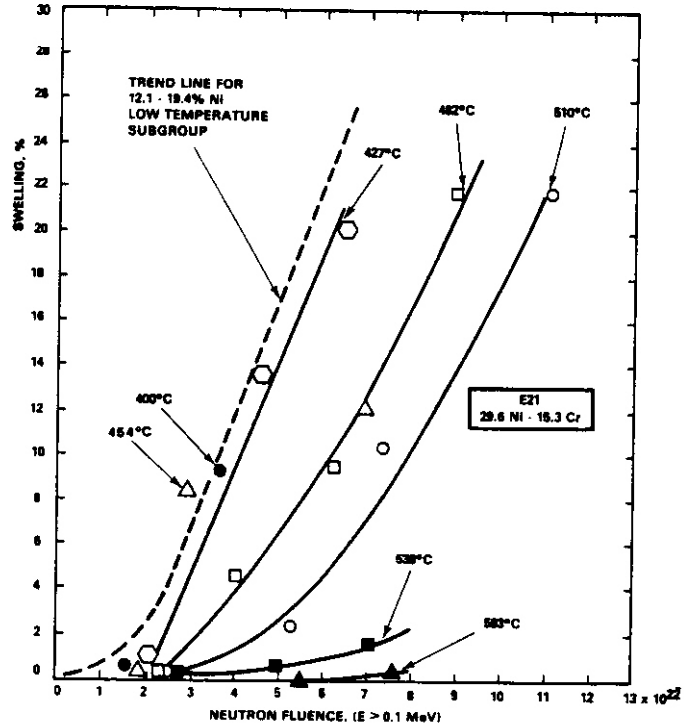

FIGURE **5.** **Swelling** *of* **One Alloy with 29.6% Nickel Content.**

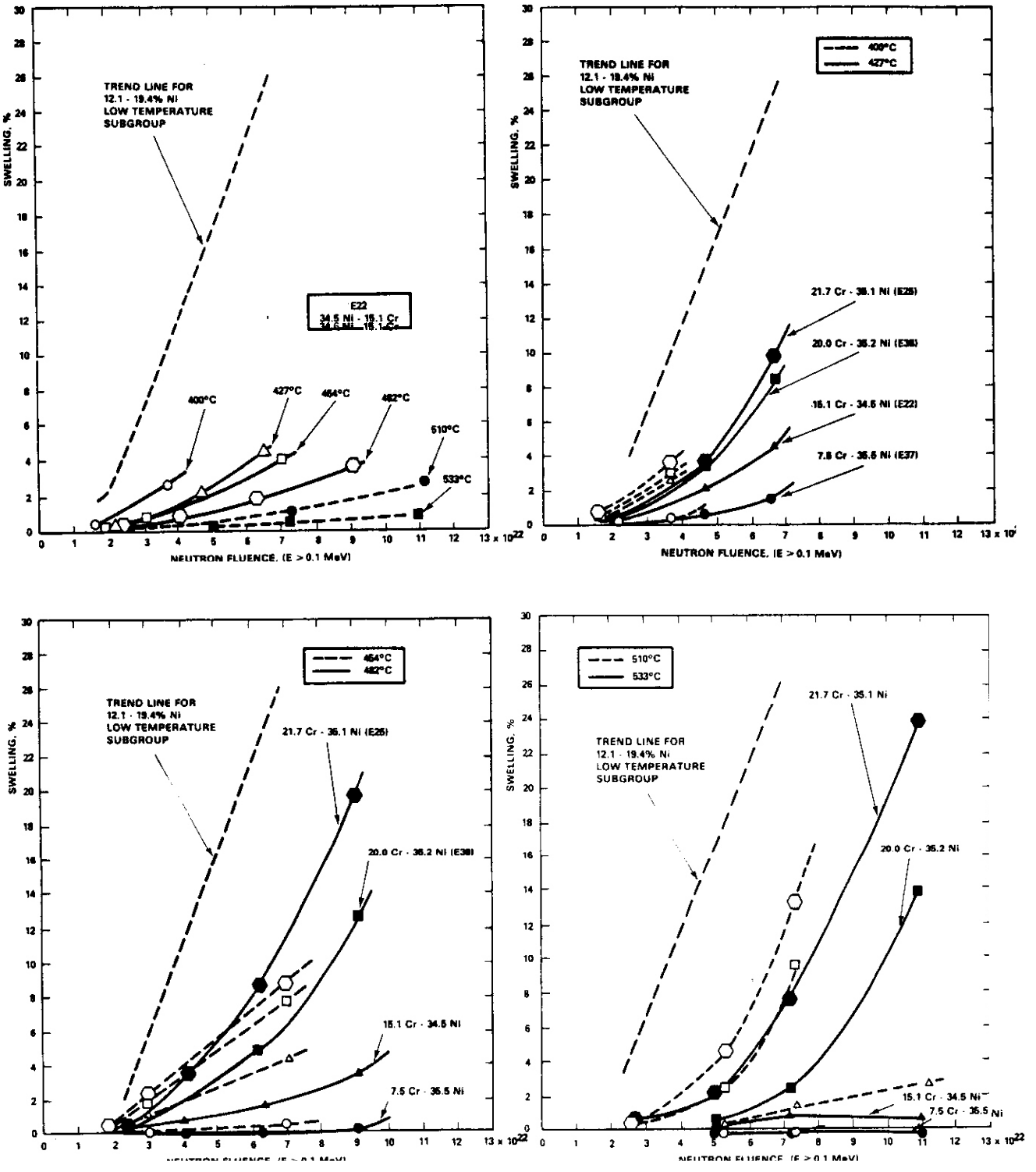

FIGURE 6. Swelling of Four Alloys with 34.5-35.5% Nickel and Varying Chromium Content.

It should be noted, however, that the curves in Figure 6a are probably approaching the slope of the trend line. The reasons for this assertion are shown in Figures 6b-d, discussed in the next section.

5.4 Dependence of Swelling on Chromium Content

Figures 6b-d contain a subset of alloys comprising E37, E22, E38 and E25, containing 34.5 - 35.5% Ni and 15.1, 20.0 and 21.7% respectively. Note that at all temperatures the effect of adding chromium is to shorten the transient regime of swelling and to yield steady-state swelling rates approaching that of the trend line. A similar trend can be seen at temperatures >482°C in Figures 7a-c. This data subset comprises the alloys E20 and E27 at 24.4 - 24.7% Ni and 14.9 and 10.2% Cr, respectively.

Figure 8a shows a subset of data comprising the alloys E39, E26 and E19 at temperatures of 510°C and below. These alloys have a narrow range of nickel concentration (19.4 - 20.3%) and chromium levels of 7.5, 11.8 and 14.9% respectively. Note once again the relatively narrow band of swelling, which closely embraces the trend line of the first data set. As shown in Figures 8b and c the trends observed with chromium level and temperature in previous figures are still maintained.

5.5 Discussion

There are several surprises arising from this analysis. First of all, there appears to be an intrinsic steady-state swelling rate of ~5% per 10^{22} n cm^{-2} (or 1%/dpa) for all Fe-Ni-Cr ternary alloys studied at <35% nickel. (The data presented in this report are judged insufficient at this time to determine the steady-state swelling rate at higher nickel contents.) Second, the steady-state swelling regime is preceded by a transient swelling regime which is shortest for low nickel, high chromium and low temperature. The transient is never shorter than ~2 X 10^{22} n cm^{-2} (E > 0.1 MeV) however. For a given nickel and chromium level there appears to be some temperature below which the transient regime is also insensitive to temperature. Third and finally,

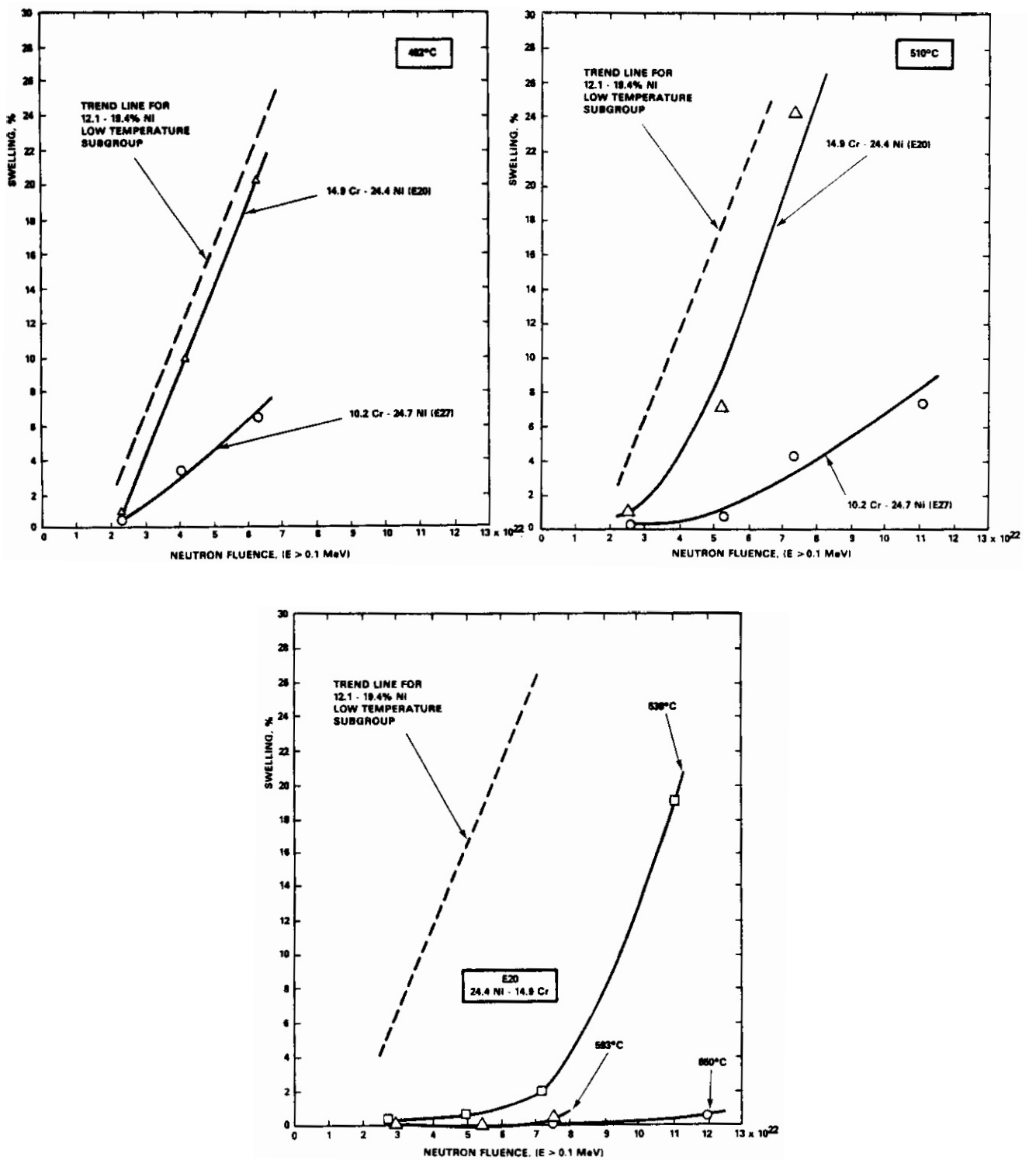

FIGURE 7. Dependence of Swelling on Chromium Content in Alloys with 24.4-24.7% Nickel Content.

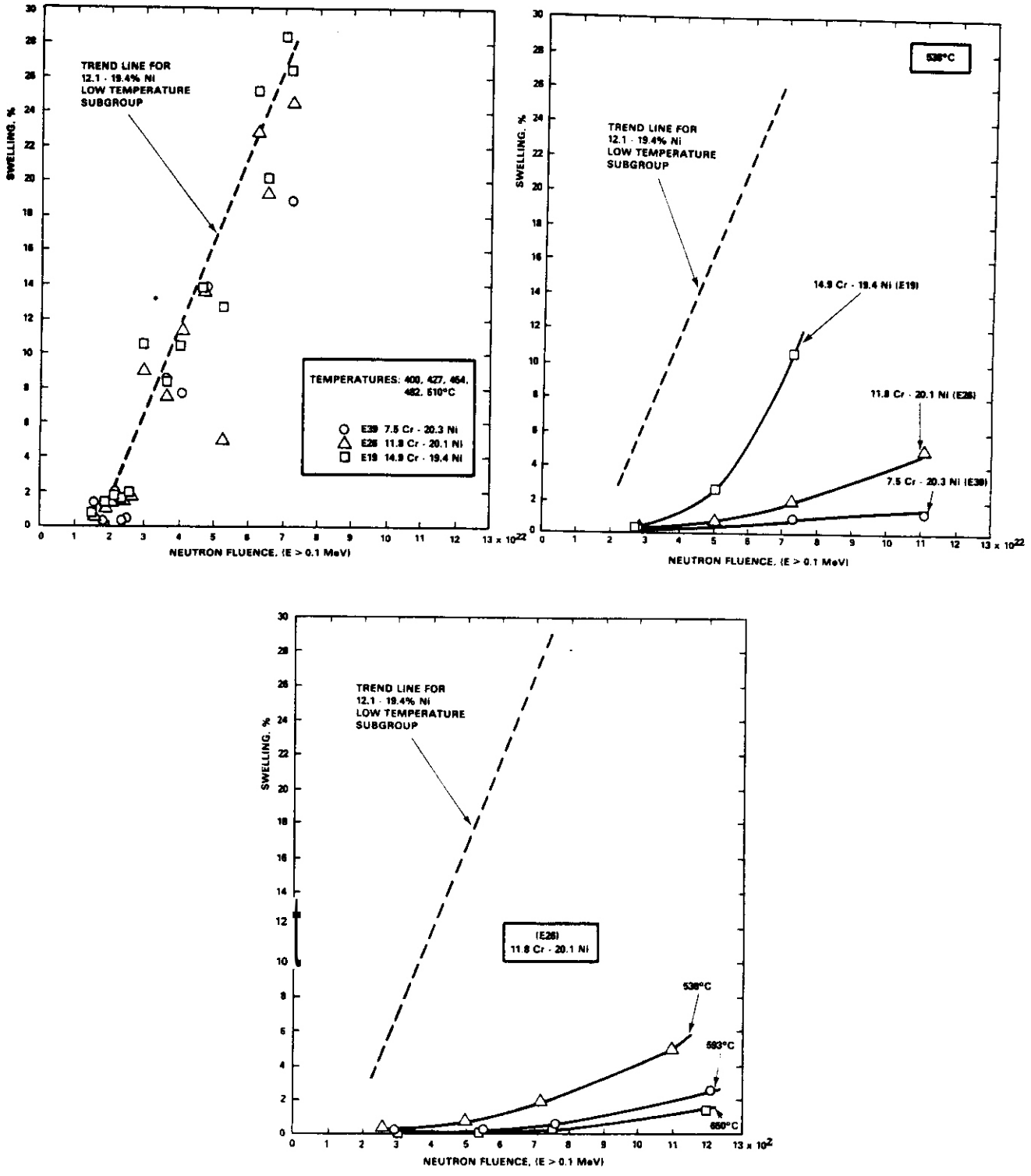

FIGURE 8. Dependence of Swelling on Chromium Content in Alloys with Nickel Contents of 19.4–20.3%.

the steady-state swelling rate itself is independent of temperature in the Fe-Ni-Cr system over a remarkably large range of temperatures (400-650°C).

The strong dependence of ion-induced swelling on nickel and chromium content in Figure 1 can now be seen to occur as a result of the influence of these elements on determining the duration of the transient swelling regime, a phenomenon which occurs only at relatively high temperatures. The extension of the transient regime with increasing nickel in Figures 3-8 always occurs by 538°C and frequently happens at lower temperatures. The ion-generated data of Figure 1 were developed at a much higher displacement rate and 675°C, a temperature comparable to 550°C in fast breeder irradiation.*

Since nickel and chromium influence the incubation period but not the steady-state swelling rate, this implies that any modeling effort must concentrate either on transient components of the microstructure or transient phenomena occurring either in the matrix or at static microstructural components. Matrix changes are expected to be minimal in pure ternaries. Frank loops are transient but eventually unfault and glide away, and network dislocations can also climb away from any segregated elements. It has been suggested that the required transient may arise from the composition-dependent consequences of radiation-induced nickel segregation and chromium depletion at the surface of void embryos.(5) This has been shown to change the void's capture efficiency for point defects. This proposal has been explored in another report and appears to be a plausible explanation for at least part of the dependence of swelling on nickel content.(6)

Note that Figure 9 shows that one subset of the ion irradiation data confirms that the primary effect of nickel is to extend the transient regime. This is once again a relatively high irradiation temperature (675°C) and the extension is shown to occur to nickel levels of at least 45%.

*A temperature shift of 125°C was assumed to compensate for the difference in displacement rates.

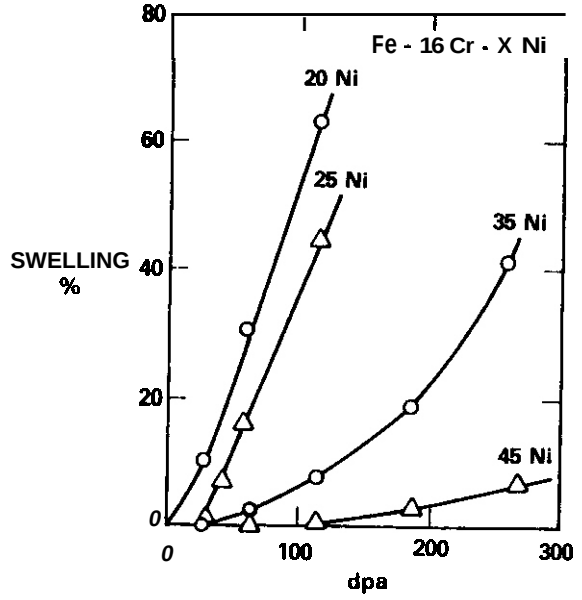

FIGURE 9. Influence of Nickel Content on Swelling Behavior on Fe-15Cr-XNi Alloys at 675°C When Bombarded with 5 MeV Ni^+ Ions.(3)

It is important to note that the strong dependence of high temperature swelling on nickel content has also been observed in ion irradiation of more complex Fe-Ni-Cr alloys containing solutes such as Mo, Si, C, Mn, etc., as shown in Figure 10. It has also been shown that the primary effect of adding such solutes is to extend the incubation period but not to change the swelling rate as shown in Figure 11. It is therefore reasonable to assume that the swelling of the more complex alloys should exhibit not only a dependence on nickel content but should also show a similar relative independence of the steady-state swelling rate on nickel content and temperature. This trend has been observed in various heats of AISI 316 and 304 steel.(7-10)

The finding that both ternary and commercial alloys exhibit an independence of steady-state swelling rate on temperature is at odds with the widely accepted perception that a strong temperature dependence exists. This perception is most strongly reinforced by most ion bombardment data. Figure 12 shows that Johnston and coworkers would have predicted a strong temperature dependence of swelling (and probably swelling rate) even for the ternary

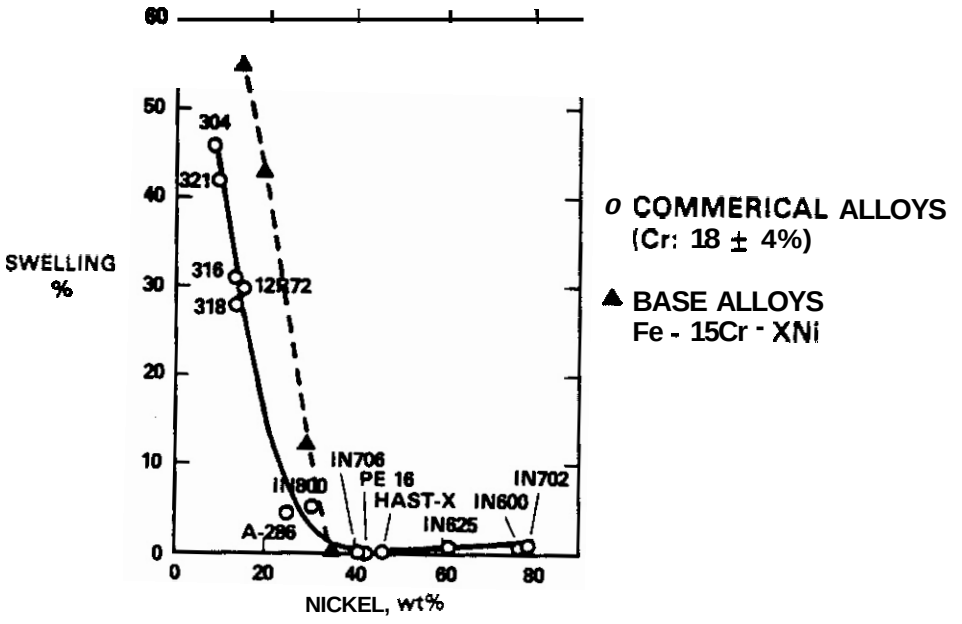

FIGURE 10. Dependence of Swelling in Both Commercial and Ternary Alloys on Nickel Content During 5 MeV Ni^+ Ion Irradiation to 140 dpa at 625°C.(3)

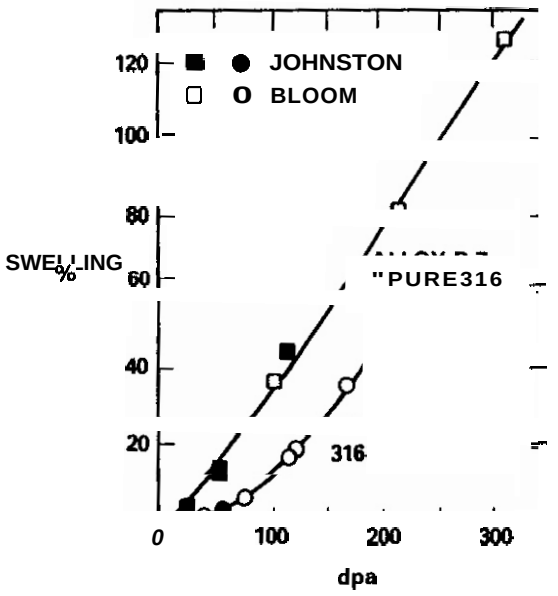

FIGURE 11. Comparison of Ion Bombardment Data on Swelling of Annealed AISI 316 Stainless Steel at 630 ± 5°C.(2,11,12) Note that solutes extend the transient regime of swelling but do not affect the steady-state swelling rate very strongly.

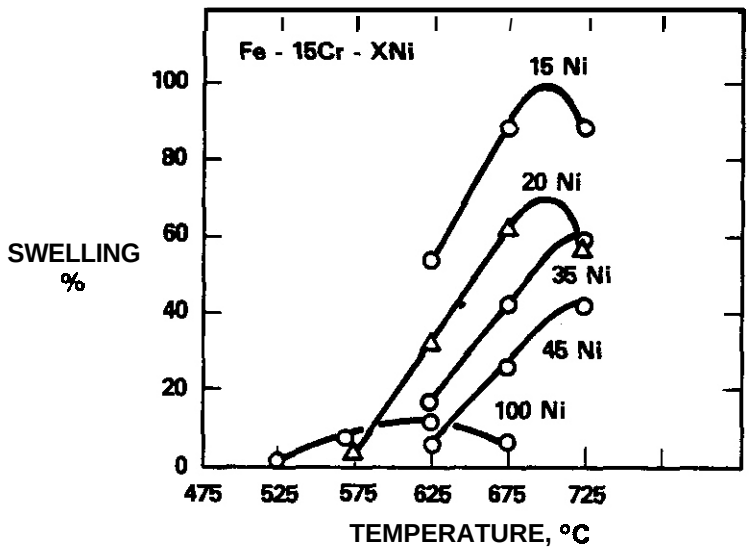

FIGURE 12. Temperature Dependence of Swelling of Ternary Alloys Irradiated With 5 MeV Ni^+ Ions to 140 dpa, as Reported by Johnston and Coworkers.(2)

alloy series. It has recently been shown(11) however, that the magnitude and temperature dependence of the ion-induced swelling rate is severely distorted by the effect of injected interstitials, as shown in Figure 13.

There is one potentially important variable which has not yet been incorporated in this analysis. This is the dependence of swelling on displacement rate, which varies roughly a factor of two between the various subcapsules in which the ternary alloys were irradiated. In any alloy where the incubation period was sensitive to temperature it is expected that there will also exist a corresponding sensitivity to displacement rate, particularly at temperatures where the transient regime begins to get longer. In addition, the data are currently correlated to neutron fluence above 0.1 MeV, which implies an assumption that the number of displacements per $E > 0.1$ MeV neutron are equal at all positions in the reactor core. As shown in Figure 14 this assumption is not completely correct. The variability or scatter of the Fe-Ni-Cr swelling data may partially arise from considerations such as these.

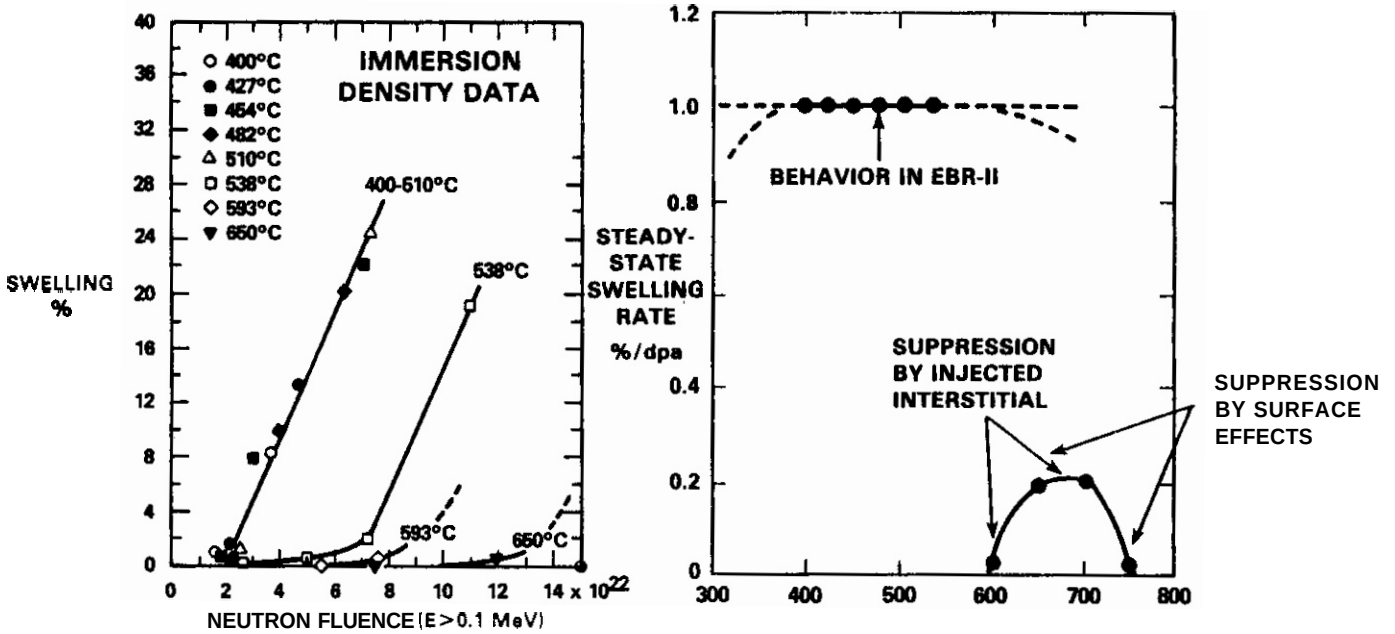

FIGURE 13. (a) Swelling of Fe-15Cr-25Ni in E8R-II as Reported by Garner.[11] (b) Comparison of the Temperature Dependence of Neutron and Ion-Induced Swelling Rates for this Alloy. The ion curve was derived from microscopy observations at the peak damage region, where the injected interstitial effect is largest. Step-height measurements yield intermediate swelling rates that are also distorted with respect to the temperature dependence observed with neutrons.[11]

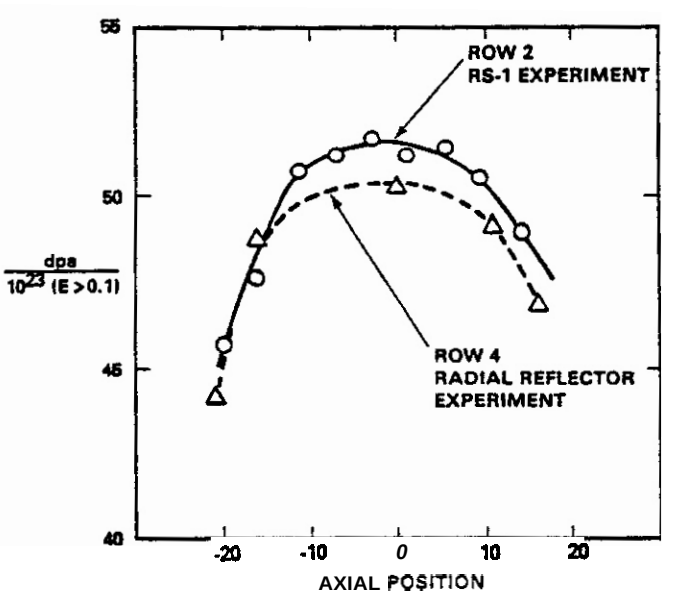

FIGURE 14. Displacement Characteristics of E8R-II Neutrons.

There are several other features of the data tabulated in Table 1, which should be explored in more depth. Note in Table 1 that many alloys, particularly those with relatively high nickel, exhibit a relatively continuous densification at temperatures of 593 and 650°C. This densification can be quite large (1.16% for E22 at 593°C) and was at first thought to be related to formation of a separate phase. More recent microscopy studies have shown that no precipitate phase forms but that densification occurs because there exists a minimum in density that occurs at 435% nickel. Substantial radiation-induced microsegregation causes the density increases.[13-15] Note also that the alloy E37 (35.5 Ni, 7.5 Cr) exhibits densification as low as 454°C. The elemental separation appears to coincide with and possibly control the duration of the transient regime. Note that E24 (75.1% nickel and 14.6% Cr) also undergoes densification and then abruptly starts swelling (12.06% at 12.1 x 10^{22} n/cm^2). There is no known density minimum in this composition regime, however, and the densification may result from precipitate formation.

5.6 Conclusions

The steady-state swelling rate of EBR-II irradiated ternary alloys with nickel content ≤35% nickel is roughly 5% per 10^{22} n cm^{-2} (E > 0.1 MeV) or 1% dpa, independent of chromium and/or nickel content and the irradiation temperature. The duration of the transient regime of swelling is sensitive to these three variables, however, tending to increase with increasing nickel and temperature, or decreasing chromium content. A similar relative independence of the steady-state swelling rate on temperature is also observed in the various commercial stainless steels, which also approach 1%/dpa at high fluence. There is some evidence that elemental segregation plays a role in the compositional dependence of swelling.

6.0 References

1. W. G. Johnson, J. H. Rosolowski, A. M. Turkalo and T. Lauritzen, J. Nucl. Mater. 54, pp. 24-40, 1974.

2. W. G. Johnson, T. Lauritzen, J. H. Rosolowski and A. M. Turkalo, Effect of Metallurgical Variables on Void Swelling, General Electric Report 6CRD019, January 1976.

3. J. F. Bates and W. G. Johnson, "Effects of Allov Composition on Void Swelling," Radiation Effects in Breeder Reactor-Structural Materials, M. L. Bleiberg and J. W. Bennett, Eds., The Metallurgical Society of AIME, p. 625, 1979.

4. J. F. Bates and R. W. Powell, "Irradiation-Induced Swelling in Commercial Alloys," J. Nucl. Mater. 102, 1981, pp. 200-213.

5. H. R. Brager and F. A. Garner, "Analysis of Radiation-Induced Microchemical Evolution in 300 Series Stainless Steel," Proceedings of AIME Symposium on Advanced Techniques for the Characterization of Irradiated Materials, Las Vegas, NV, February 1980 p. 97.

6. W. G. Wolfer and F. A. Garner, "Compositional Dependence of Radiation-Induced Changes in Dimensional and Physical Properties of Fe-Ni-Cr Austenitic Alloys," DAFS Quarterly Progress Report, DOE/ER-0046/7.

7. F. A. Garner and D. L. Porter. "A Reassessment of the Swelling Behavior of AISI 304 Stainless Steel,"'Proceedings BNES Symposium on Dimensional Stability and Mechanical Behavior of Irradiated Metals and Alloys, Brighton, England, April 11-14, 1983, paper P-8.

8. F. A. Garner and W. G. Wolfer, "Recent Theoretical and Experimental Insights on the Swelling of Austenitic Alloys," Ibid, paper 13.

9. W. J. S. Yang and F. A. Garner, "Relationship Between Phase Development and Swelling of AISI 316 During Temperature Changes," Effects of Radiation on Materials: Eleventh Conference, ASTM STP 782, pp. 186-206, 1982.

10. H. R. Brager and F. A. Garner, "Microstructural and Microchemical Comparisons of AISI 316 Irradiated in HFIR and E8R-II," J. Nucl. Mater. 117, 1983, (in press).

11. F. A. Garner, "Impact of the Injected Interstitial on the Correlation of Charged Particle and Neutron-Induced Radiation Damage," Ibid, (in press).

12. J. M. Leitnaker, E. E. Bloom and J. O. Stiegler, J. Nucl. Mater. 49, pp. 57-66, 1973.

13. H. R. Brager and F. A. Garner, "Dependence of Swellings of Fe-Ni-Cr Alloys on Chromium and Nickel Content," DAFS Quarterly Progress Report, DOE/ER-0046/11, p. 211.

14. H. R. Brager and F. A. Garner, "Radiation-Induced Evolution of Fe-Ni-Cr Alloys," DAFS Quarterly Progress Report, DOE/ER-0046/12, p. 170.

15. H. R. Brager and F. A. Garner, "Microsegregation Induced in Fe-35.5 NI-7.5Cr Irradiation in E8R-II," this report.

SWELLING OF HIGH NICKEL Fe-Ni-Cr ALLOYS IN EBR-II

H. R. Brager and F. A. Garner (Hanford Engineering Development Laboratory)

1.0 Objective

The objective of this effort is to identify the origins of the compositional dependence of swelling in simple ternary alloys.

2.0 Summary

Swelling data on Fe-Ni-Cr alloys with nickel in the 35-75 wt% range has been obtained to fluences as large as 2.2 x 10^{23} n/cm^2 (E > 0.1 MeV) (~110 dpa). At 15% chromium the swelling rate at 35, 45 and 75% nickel continues to increase with accumulating exposure, most clearly approaching 1%/dpa at ~35% nickel. The minimum often observed in swelling at ~45% nickel appears to be due to a maximum in the duration of the transient regime at this composition. Decreasing the chromium level from 15 to 7.5% extends the transient regime even further.

3.0 Program

Title: Irradiation Effect Analysis (AKJ)
Principal Investigator: D. G. Doran
Affiliation: Hanford Engineering Development Laboratory

4.0 Relevant Program Plan Task/Subtask

Subtask II.C.1 Effect of Material Parameters on Microstructure

5.0 Accomplishments and Status

5.1 Introduction

In another report the compositional sensitivity of neutron-induced swelling in annealed Fe-Ni-Cr alloys was reported for nickel levels of ≤35 wt% and exposures of <60 dpa.(1)

With the exception of Fe-35.5Ni-7.5Cr and Fe-34.5Ni-15.1Cr, the swelling data for these alloys clearly demonstrate that the primary influence of composition lay only in the duration of the transient regime that preceeded steady-state swelling (at a rate of ~1%/dpa, essentially independent of both temperature and composition).

The data for the two alloys mentioned above (as well as two other alloys at 45 and 75% nickel content) were judged to be insufficient at those exposure levels to determine whether the lower swelling observed in them was a consequence only of an extended transient regime or also a reduction in the post-transient swelling rate relative to that of other Fe-Ni-Cr alloys.

Limited additional data are now available for these four alloys at exposures ranging from 75 to 110 dpa. The new swelling data tabulated in Table 1 were obtained by immersion density measurements on small microscopy disks irradiated in sodium-filled subcapsules in EBR-II.

5.2 Results

As shown in Figure 1 the swelling rate of Fe-34.5Ni-15.1Cr at 427 and 482°C is clearly approaching 1%/dpa similar to that observed at lower nickel levels. The determination of the eventual swelling rates at 400° and 454°C requires the acquisition of higher fluence data but the swelling rate at 510°C appears to be decelerating. Figure 2a provides a clue to the cause of this behavior, however, in that there clearly is a densification of 1% or more in progress. Since these are bulk density measurements it is most

TABLE 1

HIGH FLUENCE SWELLING DATA FOR FOUR TERNARY ALLOYS

	Temperature ("C)	$\phi t/10^{22}$ (E > 0.1 MeV)	dpa**	$\frac{\Delta V}{Vo}$ -%
Alloy E37 Fe-35.5Ni-7.5Cr	400	15.2	75	1.71
	454	15.8	79	1.93
	650	21.8	109	0.31
Alloy E22 Fe-34.5Ni-15.1Cr	400	15.2	76	16.2
	427	14.5	73	21.9
	482	17.4	87	20.8
	593	22.0	110	2.90
	650	21.8	109	4.42
Alloy E23 Fe-45.3Ni-15.0Cr	400	15.2	76	2.38
	427	14.5	73	8.19
	482	17.4	87	9.42
	538	20.3	102	5.26
	593	22.0	110	1.09
Alloy E24 Fe-75.1 Ni-14.6Cr	427	14.5	73	9.03
	510	21.0	105	21.1
	593	22.0	110	4.13*
	593	22.0	110	2.37*
	650	21.8	109	31.0

*Two separate and nominally identical specimens irradiated in the same packet, indicating the sensitivity of swelling at high temperature to ambient conditions.

**The displacements per atom listed in this column are approximate values only and assume that 5 dpa = 10^{22} n cm^{-2} (E > 0.1 MeV).

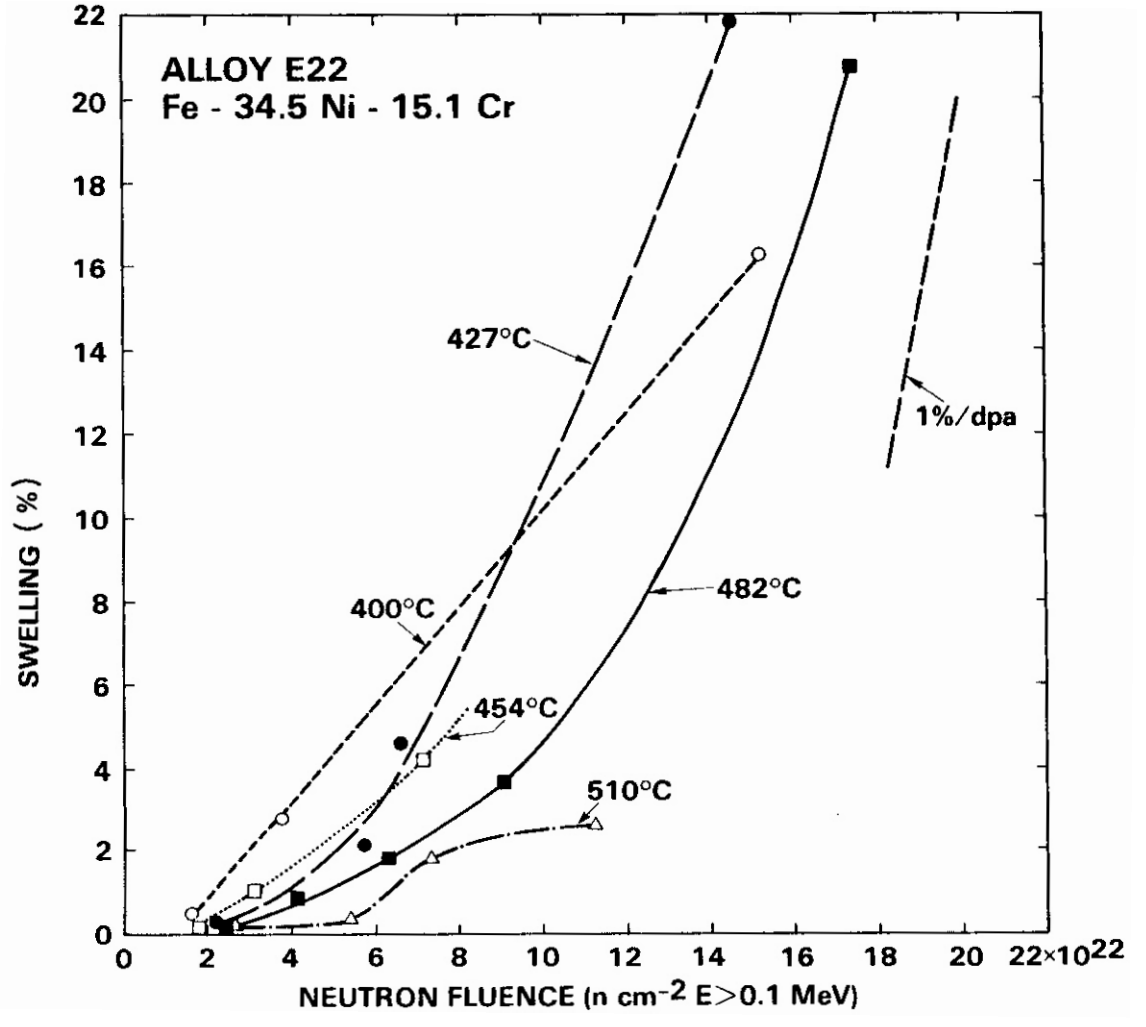

FIGURE 1. Swelling of Fe-34.5Ni-15.1Cr (Alloy E22) in EBR-II in the Range 400-510°C.

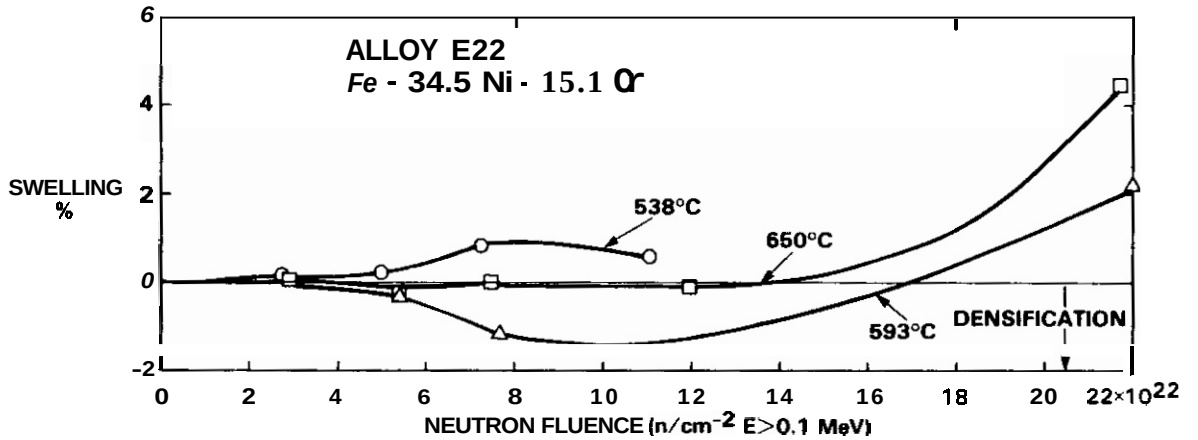

FIGURE 2a. Swelling and Densification of Fe-34.5Ni-15.1Cr (Alloy E22) in EBR-II in the Range 538 - 650°C.

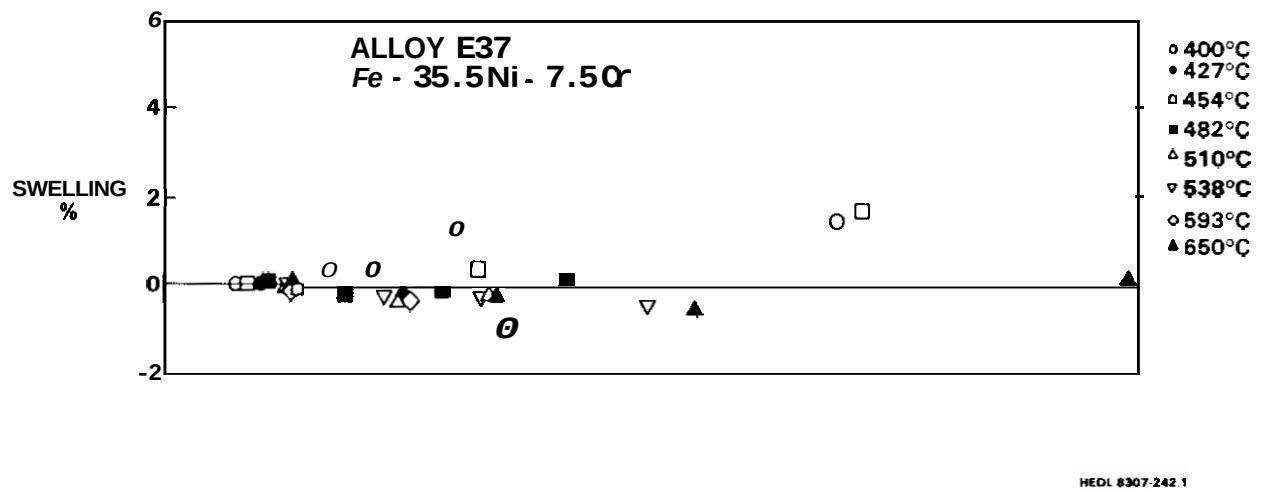

FIGURE 2b. Swelling and Densification of Fe-35.5Ni-7.5Cr (Alloy E37) in the Range 400 - 650°C.

likely that the apparent saturation of swelling at 510°C and apparent reduction at 538°C represents the competitive action of two separate processes: swelling and densification. The cause of the densification has been shown elsewhere to be microsegregation to both higher and lower nickel levels about a minimum in density that exists at ~40% nickel.[2-4]

Figure 2b shows that the transient and densification regimes of Fe-35.5 Ni-7.5Cr persist to higher fluence levels than obtained to date. The swelling in general is lower than that of the Fe-35.5Ni-15.1Cr alloy, a result consistent with both neutron[1,2] and ion[5] experiments reported earlier.

Figures 3 and 4 shows that at ~15% chromium and high nickel levels the swelling rate slowly increases with increasing exposure. At 75% nickel one observes that there is a regime of temperature (400 - 538°C) in which the swelling is relatively insensitive to temperature but at higher temperatures the transient regimes of swelling tend to become longer. At 35% nickel the same general trend is also observed. A noteable exception to this trend is seen at 650°C at 75% nickel.

In general it appears that the incubation periods of Fe-15Cr-XNi alloys at temperatures above 510°C exhibit a broad maximum at 45% nickel. This is consistent with a shallow minimum in swelling at that composition observed in ion irradiations.[5]

5.3 Conclusions

For Fe-15Cr-XNi alloys the swelling rate continues to accelerate with accumulating neutron exposure, even at nickel levels of 35-75 wt%, with about 1%/dpa as the upper limit. The minimum at ~45% in ion-induced swelling previously reported by Johnston[5] appears to arise from a maximum in duration of the transient regime of swelling. Decreasing the chromium level from 15.1 to 7.5% chromium extends the transient regime to even higher fluences.

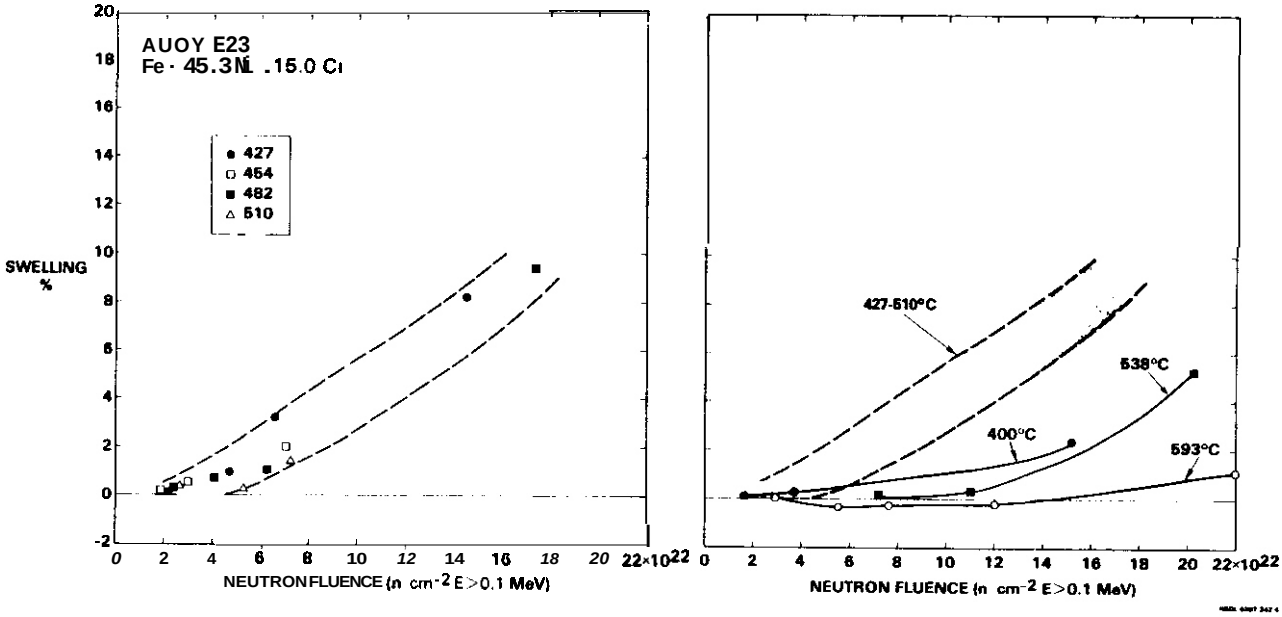

FIGURE 3. Swelling of Fe-45.3Ni-15.0Cr (Alloy E23) in E8R-II

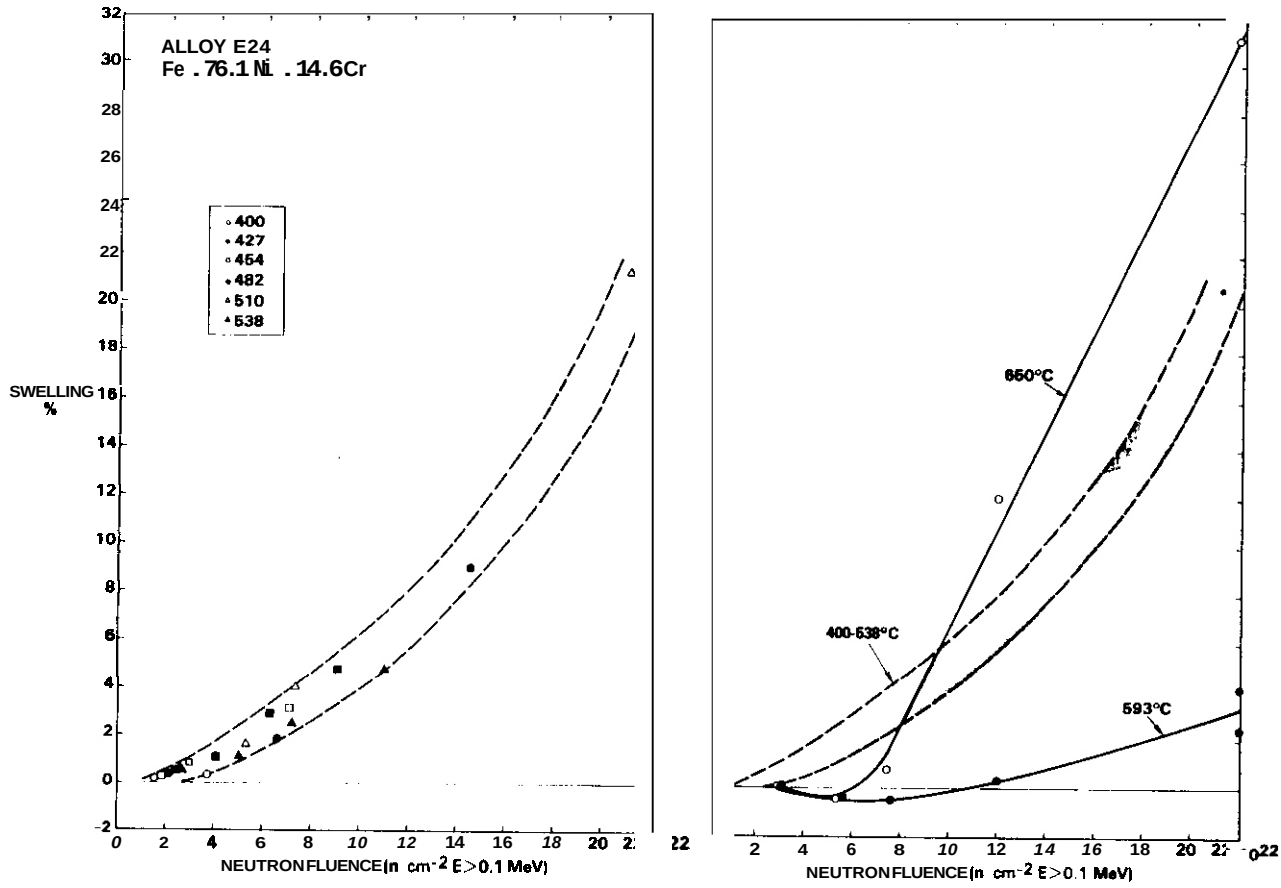

FIGURE 4. Swelling of Fe-75.1Ni-14.6Cr (Alloy E24) in E8R-II.

6.0 References

1. F. A. Garner, "Dependence of Swelling on Nickel and Chromium Content in Fe-Ni-Cr Ternary Alloys," this report.

2. H. R. Brager and F. A. Garner, 'Dependence of Swellings of Fe-Ni-Cr Alloys on Chromium and Nickel Content," DAFS Quarterly Progress Report, DOE/ER-0046/11, p. 221.

3. H. R. Brager and F. A. Garner, "Radiation-Induced Evolution of Fe-Ni-Cr Alloys," OAFS Quarterly Progress Report, DOE/ER-0046/12, p. 170.

4. H. R. Brager and F. A. Garner, "Microsegregation Induced in Fe-35.5 Ni-7.5Cr Irradiation in EBR-II," this report.

5. W. G. Johnston, T. Lauritzen, J. H. Rosolowski and A. M. Turkalo, Effect of Metallurgical Variables on Void Swelling, General Electric Co. Report 76CRD019, January 1976.

7.0 Future Work

The origins of the composition dependence of swelling in the Fe-Ni-Cr system will be described in terms of the compositional dependence of both vacancy diffusivity and elemental segregation to voids.

8.0 Publications

None.

DISTRIBUTION

UC-20 (108)

UC-20c (75)

DOE-HQ/Office of Breeder
Technology Projects
NE-53
Washington, DC 20545

PB Hemmig, Asst Director,
Reactor Physics Tech

DOE-HQ/Office of Fusion Energy (2)
Washington, DC 20545

JF Clark, ER-70
JF Decker, ER-54, G-256

DOE-RL/Office of Asst Manager for
Projects & Facilities Management (2)
FMIT Project Office

GM Chenevert, Project Manager

DOE-RL/Office of Asst Manager
for Advanced Reactor Programs
Breeder Technology Division

KR Absher, Chief,
Technology Development Branch

Argonne National Laboratory (5)
9700 South Cass Avenue
Argonne, IL 60439

LR Greenwood BA Loomis
A. Taylor H. Wiedersich
RE Nygren

Battelle Memorial Institute (3)
Pacific Northwest Laboratory
P.O. Box 999
Richland, WA 99352

JL Brimhall
DA Oingee
TD Chikalla

Brookhaven National Laboratory
Associated Universities
Upton, Long Island, NY 11973

Chairman, Nuclear Energy Dept

Columbia University
Plasma Physics Laboratory
New York, NY 10027

RA Gross

General Atomic Company (2)
P.O. Box 81608
San Diego, CA 92138

GR Hopkins
JR Gilleland

INESCO
11011 Torreyana Rd
San Diego, CA 92121

RD Stevenson

Lawrence
Livermore National Laboratory (3)
P.O. Box 808
Livermore, CA 94550

WL Barmore
MW Guinan, L-396
CM Logan

Los Alamos National Laboratory (4)
P.O. Box 1663
Los Alamos, NM 87544

DJ Dudziak J. Fowler, E-546
CR Emigh G. Hurley, E-546

Massachusetts Institute of Technology (5)
77 Massachusetts Avenue
Cambridge, MA 02139

L. Lidsky I- W Chen, 13-5118
NJ Grant, 8-305 DB Montgomery, NW21
JB van der Sande, 13-5025

DISTRIBUTION (Cont'd)

Massachusetts Institute of Technology
Nuclear Reactor Laboratory
138 Albany St
Cambridge, MA 02139

OK Harling, NW12-204

McDonnell-Douglas Astronautics Co.
P.O. Box 516
St. Louis, MO 63166

D. Kummer

Mound Laboratory
P.O. Box 32
Miamisburg, OH 45342

Manager, Tech Appl & Dev

National Bureau of Standards
Gaithersburg, MD 20760

JA Grundl

Naval Research Laboratory (3)
Washington, DC 20375

I. Manning, Code 6672
JA Sprague, Code 6395
LE Steele, Code 6390

North Carolina State University
Department of Nuclear Engineering
Raleigh, NC 26707

JR Beeler, Jr.

Oak Ridge National Laboratory (12)
P.O. Box X
Oak Ridge, TN 37830

K. Farrell
ML Grossbeck
PJ Maziasz
LK Mansur
NH Packan
M. Roberts, Director,
FG Perey
J. Sheffield
JO Stiegler
C. Weisbin
RW Wiffen
Bldg 9204-1
Bldg 9201-2

Princeton University (2)
Plasma Physics Laboratory
Forrestal Campus
P.O. Box 451
Princeton, NJ 08544

H. Furth
K. Wakefield

Risø National Laboratory
Postfach 49
DK-4000 Roskilde, Denmark

B.N. Singh

Rockwell International
8900 DeSoto Ave
Canoga Park, CA 91304

O. Kramer

Sandia National Laboratories (2)
P.O. Box 5800
Albuquerque, NM 87185

FL Vook, Org 5100

Sandia National Laboratories
Livermore, CA 94550

WD Wilson

Science Applications, Inc.
1200 Prospect
LaJolla, CA 92037

Dr. H. Gurol

University of California (2)
Los Angeles, CA 90024

RW Conn
NM Ghoniem

University of Michigan
Nuclear Engineering
Ann Arbor, MI 48109

T. Kammash

DISTRIBUTION (Cont'd)

University of Missouri
Mechanical & Aerospace Eng
1006 Engineering Bldg
Columbia, MO 65211

M. Jolles

University of Missouri
Dept of Nuclear Engineering
Rolla, MO 65401

A. Kumar

University of Virginia
Dept of Materials Science
Charlottesville, VA 22901

WA Jesser

University of Wisconsin
1500 W. Johnson Drive
Madison, WI 53706

WG Wolfer

Westinghouse
Advanced Energy Systems Division
Fuels Materials Technology
P.O. Box 158
Madison, PA 15663

A. Boltax, Manager

Westinghouse
Research and Development Center (2)
310 Beulah Road
Pittsburgh, PA 15235

JA Spitznagel
S. Wood

Commission for the European Communities
200, rue de la Loi
B-1049 Brussels, Belgium

J. Darvas

Energieonderzoek Centrum Nederland
Westerdionweg 3
NL-1755 ZG Petten, The Netherlands

B. van der Schaaf

EURATOM
Joint Research Center Ispra
Materials Science Division
1-21020 Ispra, Varese, Italy

P. Schiller

Hahn-Meitner Institute fur Kernforschung
Glienickerstrasse 100
0-1000 Berlin,
Federal Republic of Germany

H. Wollenberger

Hokkaido University (2)
Metals Research Institute
Kita-hu, Sapporo, Japan 060

Michio Kiritani, Precision Eng
Taro Takeyama

Japan Atomic Energy Research Institute (2)
Physical Metallurgy Laboratory
Tokai Research Establishment
Tokai-mura, Naka-gun, Ibaraki-ken, Japan

Shuichi Iwata, Physics
Kensuke Shiraishi, Nucl Fuel Research

Kernforschungsanlage Julich GmbH
Postfach 1913
D-517 Julich,
Federal Republic of Germany

H. Ullmaier

OISTRIBUTION (Cont'd)

Kernforschungsanlage Karlsruhe
Institüt für Reaktorbauelemente
Postfach 3640
0-7500 Karlsruhe 1,
Federal Republic of Germany

K. Ehrlich

Kyushu University
Research Institute for Appl Mechanics
6-10-1 Hakozaki, Higashi-ku,
Fukuoka, 812, Japan

Kazunori Kitajima

National Research Council
Montreal Road
Ottawa, Canada

EV Kornelson

National Research Institute for Metals
Nuclear Materials Division
1-2-1 Sengen, Sakura-mura,
Niihari-gun, Ibaraki, Japan 305

Naoki Kishimoto

Netherlands Energy Research Foundation
Materials Department
P.O. Box 1
NL-1755 ZG Petten, The Netherlands

W. Van Witzenburg

Osaka University
2-1. Yamada-oka., Suita.
Osaka, Japan 565

Kenji Sumita, Dept of Nuclear Eng
Toichi Okada,
Institute of Scientific &
Industrial Research

Science University of Tokyo
Engineering Dept
Kagurazaka, Shinjuku-ku,
Tokyo, Japan 162

RR Hasiguti

Studiecentrum voor Kernenergie
Centre d'Etude de l'Energie Nucleaire
Boeretang 200
B-2400 Mol, Belgium

J. Nihoul

Swiss Federal Institute
for Reactor Research
CH-5303 Wuerenlingen, Switzerland

WV Green

Tokyo Institute of Technology
12-1, 2-Chome, O-Okayama
Meguro-ku, Tokyo, Japan

Kensutaka Kawamura

United Kingdom Atomic Energy Authority
Atomic Energy Research Establishment
Metallurgy Division
Building 388
Oxfordshire, OX11 ORA, UK

DR Harries

University of Tokyo (3)
- -1 Hongo
Bunkyo-ku, Tokyo 113, Japan

Naohira Igata, Met & Mater Science
Shiori Ishino, Nuclear Eng
Taijiro Uchida

DISTRIBUTION (Cont'd)

HEDL (43)

SD Adkin	W/A-58	EK Opperman	W/A-58
TK Bierlein	W/A-1	NF Panayotou	W/A-65
HR Brager	W/A-64	RW Powell	W/A-64
LL Carter	W/B-47	RJ Puigh	W/A-58
DG Doran	W/A-57	FH Ruddy	W/C-39
EA Evans	W/C-23	FA Schmittroth	W/A-4
FA Garner	W/A-57	WF Sheely	W/C-62
DS Gelles	W/A-64	RL Simons	W/A-57
R. Gold	W/C-39	JL Straalsund	W/A-61
JW Hagan	W/B-41	HH Yoshikawa	W/C-44
HL Heinisch (2)	W/A-57	DAFS Files (10)	W/A-57
DL Johnson	W/A-4	Central Files (3)	W/C-110
GD Johnson	W/A-65	Publ Services (2)	W/C-115
FM Mann	W/A-4	Document Services	W/C-123
WN McElroy	W/C-39	Microfilm Services	W/C-123